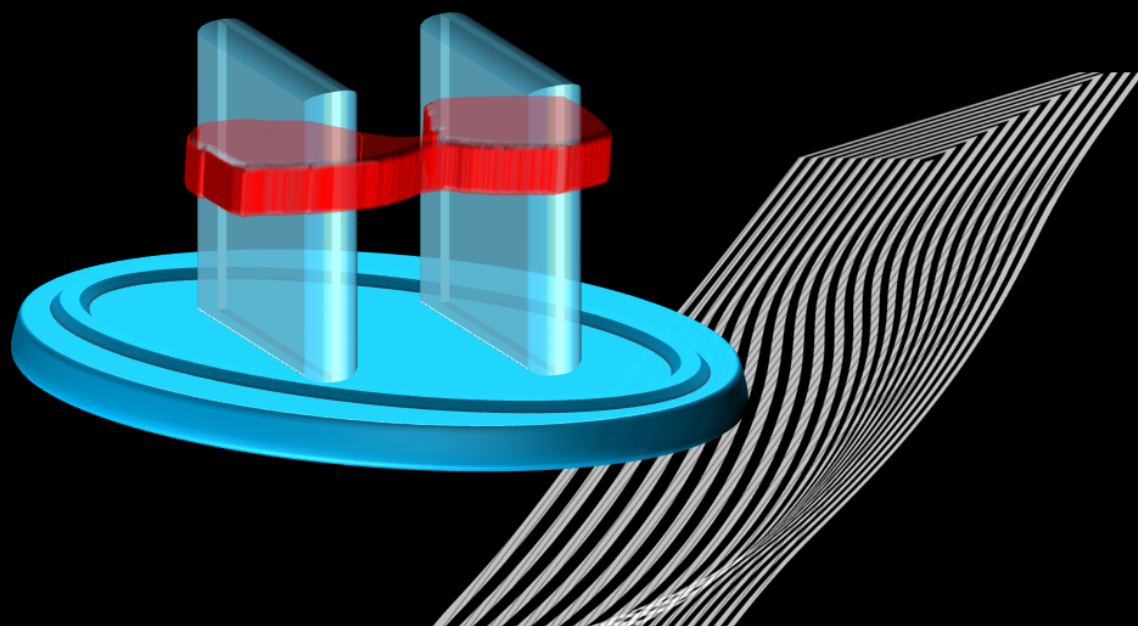# Design and Development of Integrated Displacement Sensors for Engineered Heart Tissue Platforms

Mahdieh Shojaei Baghini

TUDelft

EKL

Design and Development of Integrated Displacement Sensors for Engineered Heart Tissue Platforms

By

Mahdieh Shojaei Baghini

in partial fulfilment of the requirements for the degree of

Master of Science
in Biomedical Engineering

at the Delft University of Technology,
to be defended publicly on Thursday August 27, 2020 at 10:30 AM.

Thesis committee:	prof. dr. ir. Pasqualina M. Sarro (Chair),	TU Delft
	dr. M. Mastrangeli (Supervisor),	TU Delft
	prof. dr. ir. Jenny Dankelman (Co-supervisor),	TU Delft
	dr. M. k. Ghatkesar (External member),	TU Delft

TUDelft

CONTENTS

ABSTRACT

Cardiac cells derived from stem cells exhibit cellular contractions when cultured in vitro. They can be integrated with polymeric platforms consisting of micropillars, which act as anchors and pre-load for engineered heart tissue (EHT). The biomechanical response is often characterized using optical microscopy to track the displacement of pillar tops and assess the contractile properties of the EHT. This requires bulky instruments with sophisticated imaging algorithms, which are often prone to optical misalignment. The efficiency of the imaging algorithms is highly dependent on the structure of the top surface of the pillar.

In this thesis, an alternate approach to microscopy is presented. A novel sensor is designed, fabricated and characterized which converts the pillar response such as strain or displacement to a measurable output which can be further conditioned and read-out by an instrumentation module. As the first step, in-depth multiphysics simulations have been carried out analysing the response of the micropillar system integrated with sensors utilising piezoelectric, piezoresistive and capacitive sensing techniques. A quantitative and qualitative comparison based on the derived simulations was performed and the most optimal sensing platform was chosen.

Spiral sensors inspired from co-planar waveguides are designed and developed in such a manner so as to provide seamless integration with the process flow for the micropillars developed at ECTM and fabricated at EKL in TU Delft. The integrated sensors exhibit a change in capacitance due to warping of fringe electric field lines with the application of force to pillar boundaries. The simulated sensitivity of the sensors are 1.51-4.86 pF/N depending on the metallization ratio and average path length.

The sensors are fabricated via clean room processing and encapsulated within two layers of PDMS. On account of their low line widths ($5-40\mu m$), they have been successfully patterned with inductively coupled plasma. Simultaneously, the steps required for the fabrication of the EHT platform have been carried out.

The characterization of the sensors has been performed using on-wafer probing and equivalent lumped element circuitry also derived. The resulting capacitances are in excellent agreement with the optimised simulations in COMSOL. The sensors exhibit a stable base-line response to AC signals with frequencies up to 1 MHz and voltages up to 20 V_{rms}, the highest limits to the test signals of the instrumentation setup. Preliminary characterization of the sensor's response to mechanical loading exhibits promising outcomes. The read-out circuitry of the time varying capacitors is simulated in SPICE leading to a successful first level assessment of the designed novel sensors for biomechanical characterization of tissues grown on EHT platforms.

ACKNOWLEDGEMENTS

Completing a thesis during a global pandemic is not an easy task and I would not have been able to do it without the continuous support and guidance of my supervisors. Milica, thank you for being patient with me and for all your guidance, I couldn't have asked for a better daily advisor. To my supervisors, Massimo, Lina, and Jenny, I appreciate all the technical and personal values I assimilated during our meetings and discussions. Together we created something new and exciting, and I enjoyed it every step of the way. A thank you to Sten as well, I quite enjoyed our discussions.

A big virtual hug to my new found family at EKL. Thank you for answering my continuous in-flow of questions in the clean-room. Mario, Tom, Silvana, Hitham, Johannes, Bruno, Paolo, I am grateful for learning what I did from you. I will forever be in awe of the expansive knowledge one can gain whilst working on an interdisciplinary project. I will miss our waving to each from one end of the clean-room to the other. Brahim, Mojtaba, Hande, Paul, I am very grateful for your support. PS@Hande: Cue a puppy-eyed baby Yoda meme. A big thank you to Paul and Frank from COMSOL for your constant guidance on multiphysics modelling.

Ronald and Berend, thank you for introducing me to the wide world of heart on chips. Who would have thought that I'd get a chance to work on them more than a year later. I am glad a meeting was scheduled in Eindhoven on one fine Monday morning since I got to see the sunrise for the first time in a while.

My friends without whom many days would have been very difficult. Swaathi, Pradeep and Jon, thank you for always being there on the bad days and on the good ones. Yaqian and Anita, it was amazing sharing an office with you two. I will surpass the word limit of this thesis if I named everybody in my life who have, in their own ways, helped me where I am today. To my amazing classmates that became friends and now family. Maybe we should have the zoom call we've been talking about for months.

Lastly, the people without whom I would not have been here, literally. To my parents and grandmother back home. I miss you all and can't wait to see you again after more than a year which seems like eternity. Your support, love and encouragement are the reason I am here.

Here's to the future and everything it might hold.

1

INTRODUCTION

This chapter is a summary of the Literature Review and Thesis Introductory report [1].

1.1. ORGAN-ON-CHIPS (OOC)

The driving force behind the development of Organ-on-Chip devices is the invention of drug testing platforms which closely mimic tissue microenvironment along with providing reliable results [2]. This is further amplified during pandemics such as COVID-19 when timely, cost-effective and efficient testing systems are of the essence. The steps leading to commercialization of medicines are multiple stages of trials beginning from cellular studies (phase 0) to commercial availability (phase 4) [3]. Since cellular studies are often carried out on two-dimensional systems such as Petri dishes, the obtained tissue cultures exhibit properties different from physiological tissue in terms of cellular constituency, stiffness, interactivity with other cellular components, action potential generation and overall response to drugs and vaccines [4][5]. This often leads to testing failure once the drug has transitioned from 2D systems to the human body [5]. In order to better predict the response of a drug in vivo, in terms of benchmarks such as drug dynamics and kinetics, three-dimensional setups are being developed as alternatives to 2D systems [6]. They provide higher degrees of freedom for tissue growth while simultaneously paving the way for customized medicine via their integration with Human Induced Pluripotent Stem Cells (HiPSC) [5][6]. The differences between two dimensional and three dimensional cell cultures are shown in Table 1.1.

Table 1.1: Comparison of 2D and 3D cellular culture platforms.

2D Cell Culture	3D Cell Culture
Fixed (usually high) stiffness	Variable stiffness based on fabrication parameters
Proliferation space is limited	Higher degrees of freedom in terms of growth
Require assistance from microfluidic technologies to emulate spatial differences (for example, pressure and ionic gradients)	Gradients can be incorporated within the scaffold (for example, scaffolds with variable porosity from one end to the other)
Cell anisotropy/polarity is forced to behave endothelial-like due to absence of multiple layers.	Cultured cells can exhibit all polarities based on phenotype
Suitable mostly for drug efficacy and differentiation studies	Suitable for drug efficacy, differentiation, mechanical, and electrochemical studies.

The development of three dimensional systems is inspired by microfluidic and transistor technology [7]. Termed as organ on chip devices (OoC), they can be integrated with tissues derived from organs such as the heart, brain, and the gut as illustrated in Fig. 1.1 [8]. Functions innate to tissue type can be replicated on these platforms such as contractile forces generated in heart tissue, transport phenomena in the kidney as well as inhalation and exhalation through lung alveoli [8]. Table. 1.2 provides an overview of organ tissues which can be emulated using OOC technology as well as their key properties.
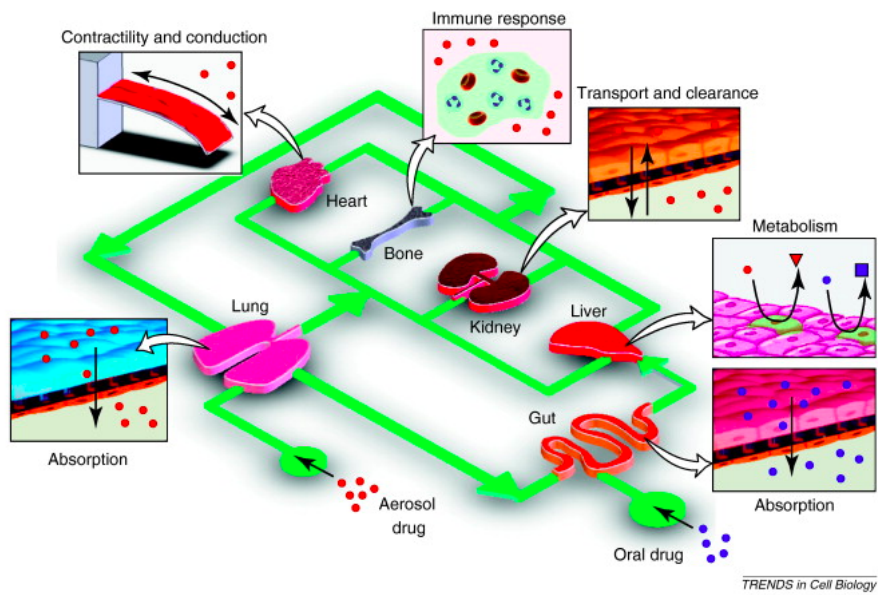

Figure 1.1: Overview of physiological phenomena which can be emulated using OOC devices [8].

Organ-on-Chip models are often constructed using polymers such as polyimide, poly-dimethylsiloxane (PDMS) and polymethylmethacrylate (PMMA) [21]. PDMS is of particular interest due to its biocompatibilty, high transparency, ability to be patterned using microfabrication technology and control over its mechanical properties such as stiffness [22]. Some examples of fabricated OOC devices are shown in Fig. 1.2.

Table 1.2: Properties of OOC devices with respect to organ function

ORGAN-ON-CHIP Devices	
Organ	**Key Properties**
Lung [9][10]	• Emulation of epithelial, endothelial and alveolar space. • Airway simulation using microfluidics. • Drug testing for asthma, MERS, lung cancer, COVID-19, SARS
Liver [11][12]	• Capability for growth of hepatocytes and subsequent analysis of urea production. • Integration with perfusion systems for monitoring of real-time flow. • Drug testing for liver cirrhosis, hepatitis, jaundice
Kidney [13][14]	• Emulation of pressure differences along the height of the nephron. • Development of Na^+-K^+ pumps across microfluidic membranes. • Drug testing for UTIs, Chronic Kidney failure.
Skin [15][16]	• Ability to trigger on-chip inflammatory response on exposure to foreign media. • Fibrin matrix development. • Drug testing for burns, skin cancer and eczema.
Brain [17][18]	• Culturing of on-chip collagenous neural network. • Emulation of the blood-brain-barrier (BBB). • Drug testing for brain cancer, Alzheimer's, ADHD, Epilepsy.
Heart [19][20]	• Generation of the vascular network required for transport of blood. • Development of action potentials in grown tissue. • Drug testing for Coronary Artery Disease, thrombosis, arrhythmia.

Despite their potential advantages, OOCs are not without drawbacks. The maturation of cells integrated with OOC platforms is lower than their physiological counterparts and often require external stimuli for growth [28]. From the perspective of microfluidic technology, efficient transport of fluids and their mixing is hindered due to the changes in fluid flow characteristics at lower dimensions ($< 100 \mu m$) as well as adsorption of chemicals by PDMS which can lead to variations in drug efficacy studies [29].

Research continues to further the developments in OOC platforms due to their promising ability to aid and in the future, replace animal testing as well enable point-of-care testing while providing an improved mimicry of physiological tissue microenvironment [30]. The tissue pertaining to the OOC platform utilised during this thesis is the cardiac tissue of which the platform is discussed in the next section.
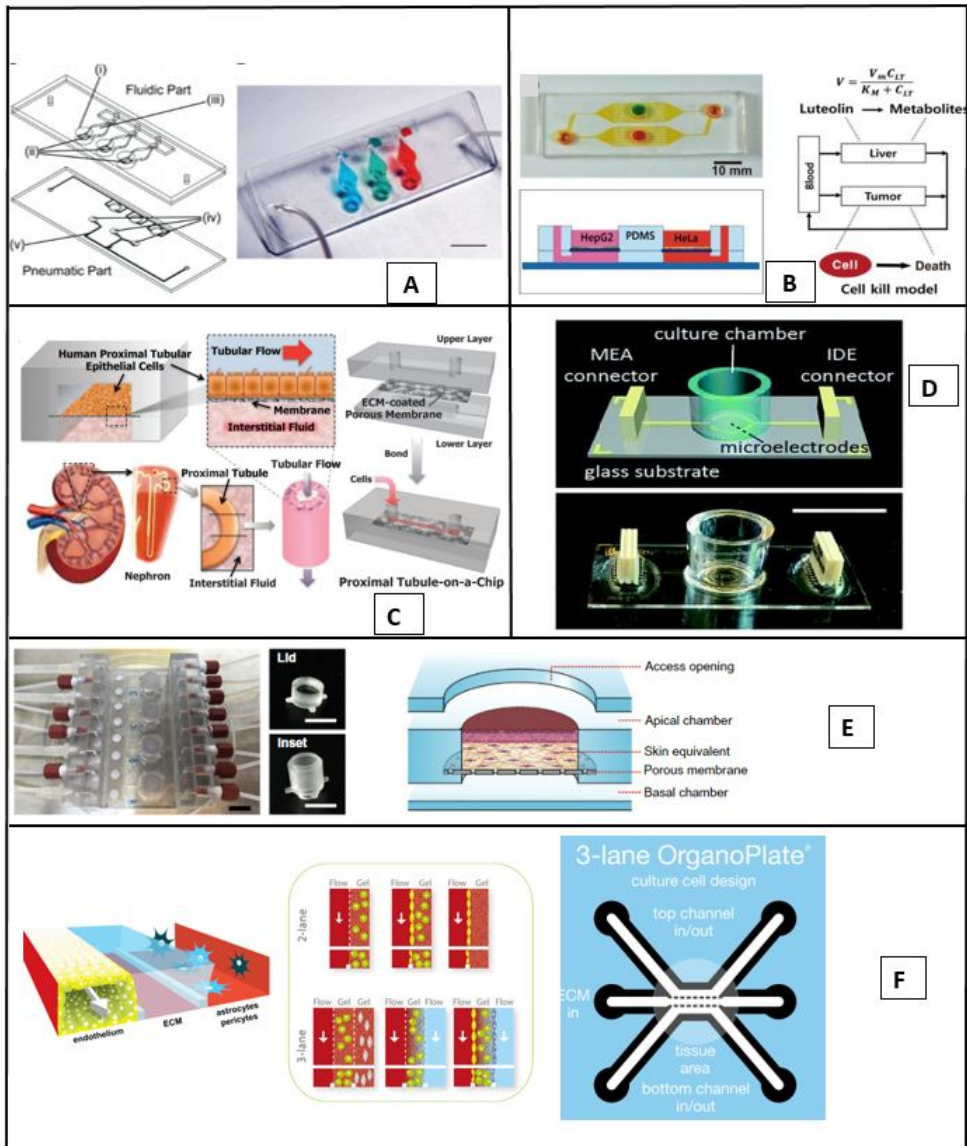
Figure 1.2: Example of organ tissues which can be emulated in one or more aspects by utilising OOC technology. A) Lung-on-chip [23] B) Liver-on-chip [24] C) Kidney-on-chip [25] D) Heart-on-chip [26] E) Skin-on-chip [15] F) Brain-on-chip [27]

1.2. CARDIAC TISSUE MODELS

Cardiac tissues are often modeled by 2D systems in conjunction with external stimuli as shown in Fig. 1.3 [31]. Cardiac tissue material can be split into various components namely, cardiomyocytes, fibroblasts, extracellular matrix, endothelial cells and cytokines

[32]. Physiologically, there exists an intricate and balanced communication system between these components which is currently difficult to replicate. However, multidisciplinary research has lead to discoveries wherein the growth of cardiac tissue can be controlled by utilising external signals such as electrical stimulation and mechanical loading [33]. Combined with microfluidic systems which mimic vascular systems as well as polymeric platforms for growth of biocompatible tissue, cardiac cells can receive better guidance towards maturation.
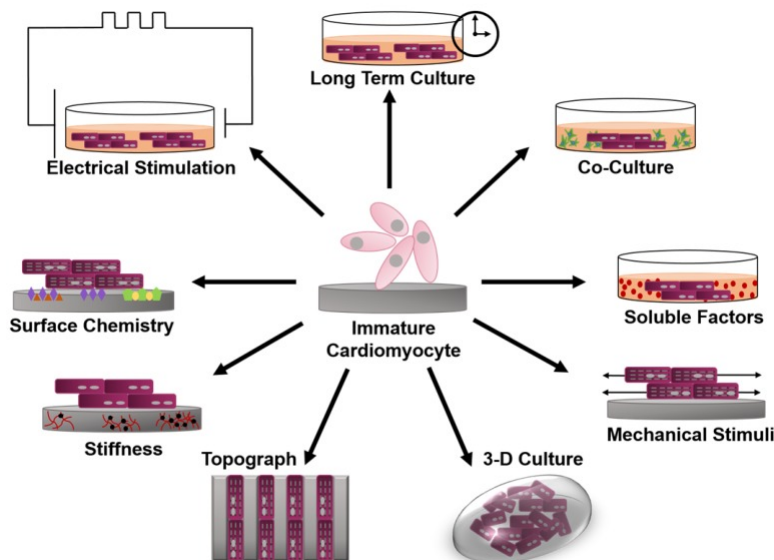
Figure 1.3: External stimuli which have the ability to contribute to cardiomyocyte maturation [31].

1.3. THE ENGINEERED HEART TISSUE (EHT) PLATFORM

Factors which contribute to maturation and efficient proliferation of cardiac tissue are the presence of mechanical pre-load and electrical stimulation [33]. In vivo heart cells are exposed to auxotonic loading which involves a positive force-strain relationship during contraction followed by a stress relaxation phase [34]. Hence there always exists a certain degree of resistance to contraction which can be emulated in heart on chip architectures. The most commonly used platforms for this purpose are shown in Fig. 1.4 and the resulting grown tissues are termed as engineered heart tissue (EHT).

The EHT platform developed at ECTM and fabricated at EKL is inspired by the Heart-Dyno system which consists of micropillars around which cardiac tissue has the ability to grow and contract as shown in Fig. 1.5 [35].
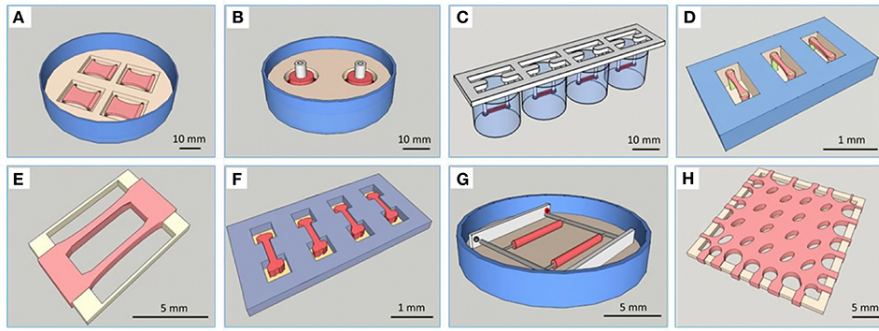
Figure 1.4: Examples of Engineered Heart Tissue (EHT) models. A) Planar EHT B) Round EHT C) Fibrinogenous EHT D) EHT grown around fluorescent pillars E), F), G), H) EHTs grown within a frame [35].
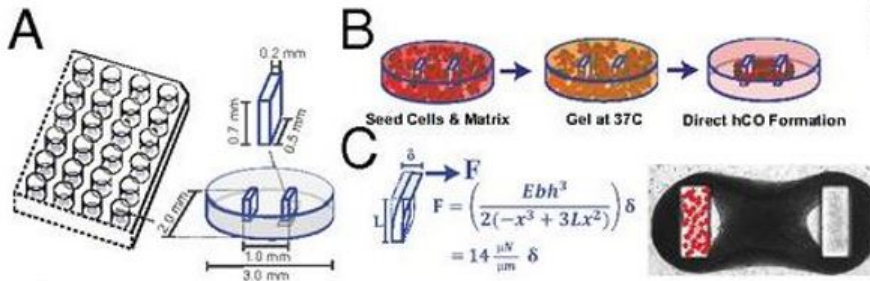
Figure 1.5: Engineered heart tissue with auxotonic loading using PDMS pillars A) Individual EHT platform for each well in a 24 multi-well plate B) Formation of cardiac tissue after incubation C) Correlation of cardiac contractile force (F) with observed displacement of pillar top (δ) during microscopy [36]

The Heart-Dyno system has been scaled down to create micro-pillar EHT platforms which have the ability to provide mechanical loading to cardiac tissue while utilising a lower number of cells and enabling the development of EHT platforms using microfabrication technology which can be implemented in a clean room [37]. This also aids in the development of on-chip measurement and stimulation techniques with the aid of sensors and electrodes. The complete system can be integrated with standard well plates leading to the development of smart drug testing platforms. The EHT platform and its placement within a well is shown in Fig. 1.6 [37]. The micropillars are fabricated using PDMS with the presence of a second polymeric well wherein the cell culture medium is transferred to for further proliferation and growth.

Cardiac tissue is often characterized by generated contractile forces and action potentials [38]. The forces provide an indication of tissue volume, maturation, and their variation due to external stimuli and drug exposure. Optical microscopy is the most commonly used technique for the derivation of cardiac contraction force [36][39]. This is achieved by correlation of observed displacement (shown by δ in Fig. 1.5) with the tis-

sue contractile force. To be able to efficiently correlate pillar displacement with contraction force, the stiffness which relates the force and the displacement of the platform must be known. However as the complexity in geometry of the platform increases, the exact derivation of its stiffness becomes cumbersome and difficult to validate and measurement techniques which aid in validating the results obtained from microscopy must be utilised. Additionally, in order to measure the thickness of the tissue the focal plane must be manually varied which can cause errors in recordings. Human errors such as misalignment can cause significant discrepancies in results as well [39]. In order to circumvent these challenges, the development of a novel integrated sensing technique is explored in this thesis.
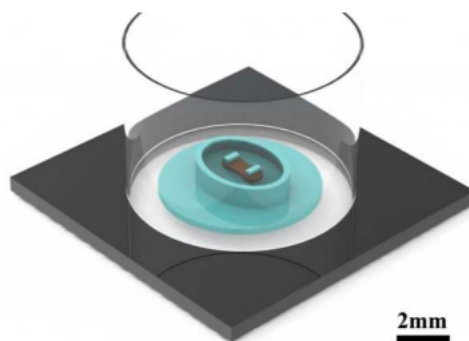
Figure 1.6: Minitiarized EHT platform placed inside a singular well [PDMS EHT platform: blue, cardiac tissue: red] [37]

In literature, only one study has been performed which explores the integration of sensors with micropillar systems (to the best of the author's knowledge) by Kevin et al. [40]. The microfabricated silicone micropillars were embedded with magnetic materials around which tissue growth occurred [40]. The magnetic field is measured using a giant magnetoresistive sensor (GMS) placed outside the platform in the well-plate leading to a semi-integrated system. As the cardiac tissue contracts, the forces displace the pillar and cause an alteration in the electrical output of the GMS [40]. The micropillar platform developed by Kevin et al. utilises one rigid pillar and one flexible pillar in which an embedded magnet is placed while the miniaturized EHT tissue consists of two flexible pillars around which the tissue is anchored.

Aim: This graduation project aims at the development of an integrated sensor for measurement of tissue contractile forces. Since this has not been attempted before for micropillar EHT platforms, inspiration is drawn from domains of flexible sensors and bioMEMS. Transducers which utilise changes in their electrical properties due to external forces are the primary choice of sensing technique due to their innate ability to be incorporated with integrated circuits (IC) and printed circuit boards (PCB).

1.4. Research Objectives and Thesis Outline

In Chapter 2 the first level assessment of a novel integrated sensor is carried out by an in-depth finite element modeling of transduction mechanisms such a piezoresistive, piezoelectric and capacitive techniques inspired from literature, integrated with the EHT platform developed at EKL. Normalized sensitivities of the proposed sensors are qualitatively and quantitatively compared. This analysis provides in-sights into the suitability of the sensors for integration with the EHT platform through the usage of constitutive relations which couple mechanical and electrical domains and aid in understanding sensing principles. An overview of different sensing modalities is provided in Table 1.3 of which one will be chosen to transduce tissue contractile energy to electrical energy.

In a separate study, the PDMS micropillars attached to the substrate will be analysed keeping in mind their continuum with the soft elastic PDMS substrate underneath, via models derived from literature. The research objectives for Chapter 2 are as follows.

- Development of a generalised substrate displacement equation due to the tilting and bending of miniaturized micropillars on application of a boundary load.

- Validation of COMSOL derived substrate response with analytical equations derived from continuum mechanics.

- Analysis of mechanical dependent variables to define optimal positions of the sensors.

- In-depth analysis of different sensing modalities utilising mutiphysics couplings.

- Analytical validation of the electrical properties of the chosen sensor to corroborate finite element modelling.

- Comparative analysis of the designed sensors leading to the choice of a single sensor type which will be utilised for further fabrication.

Once the sensor has been designed, full-wafer masks are developed for the sensors and their integration into the EHT platform taking into account the initial process flow of the fabrication of the EHT platform, in Chapter 3. Along-side the patterning of sensors and their encapsulation in PDMS, the steps required for the development of micropillars are also carried out based on the protocol previously developed at ECTM and fabricated at EKL, TU Delft. The research objectives for Chapter 3 are as follows.

- Patterning of sensors on PDMS without the addition of intermediate layers such as polyimide to simplify the fabrication flow as well as minimize potential losses in sensitivity of mechanical sensors.

- Utilising dry etching instead of wet etching, if sensors have low contact area with PDMS, to avoid their detachment from the substrate. Due to the low selectivity of dry etching processes, the etch rates of masking materials and PDMS are also derived under the conditions utilised for etching of sensors.

- Obtaining the number of cycles required to etch silicon substrates for moulding of PDMS based on recipes previously developed at EKL, TU Delft.

- Adjustment of COMSOL simulations in Chapter 2 taking into account the differences which might occur during fabrication of the sensors as compared to their designed dimensions.

The last stage of the assessment is covered in Chapter 4 wherein the electrical characterization of the designed and developed sensors with respect to their base-line capacitive outputs as well as frequency response is carried out. A statistical analysis is performed on the measurements along with the development of a lumped model circuit to better understand the electrical response of the system. The research objectives of Chapter 4 are as follows.

- Probed wafer measurements of electrical response of the designed and developed sensors.

- Development of a lumped model circuit taking into account parasitic components to discern the appropriate frequency range required for sensor operation.

- Comparison of the measured baseline capacitance with validated simulations to gauge efficiency of mesh sizes and and simulation flow.

- Venturing into the first stage of the simulation of a read-out circuit in SPICE suitable for on-chip measurements of sensor response paving the way towards the development of a one of a kind sensing platform for bio mechanical characterization of engineered heart tissues.

Chapter 5 concludes this thesis and provides a future outlook.

Table 1.3: Sensing materials utilised for modelling of sensors integrated with the EHT platform.

Sensing Mechanisms		
Technique	Key Properties	Materials utilized
Piezoresistive [41][42]	• Change in resistance due to deformations in the material. • Can be integrated with soft materials using Silicon-on-Insulator (SOI) technology. • Influenced by changes in external temperature. • Wheatstone bridges are utilized for read-out. • Anisotropic sensors exhibit different sensitivities depending on orientation.	• Metals, monocrystalline and polycrystalline Silicon, PEDOT-PSS, graphene • Exhaustive list and their compatibility with cardiomyocytes are provided in Appendix A.
Piezoelectric[43][44]	• Polarization of material due to external stress leads to a change in output voltage. • Suitable for high frequency applications and require the presence of additional electronics for quasi-static excitations. • Charge-to-voltage conversion is utilized for read-out, often accompanied by on-chip amplification. • Anisotropic sensors exhibit different sensitivities depending on orientation.	• Lead Zirconate Titanate (PZT), Aluminium Nitride (AlN), polyvinylidene difluoride (PVDF), quartz.
Capacitive [45][46]	• Change in capacitance due to relative displacement of plates and changes in dielectric properties induced due to external stresses. • Sensing often does not rely on change in the dimensions on plates due to external stress. • Exhibit parasitic components with the environment as frequency increases. • Not affected by changes in external temperature • Read-out performed via integration with oscillators and lock in amplifiers.	• Plates constructed using metals and materials with good charge storage capabilities and dielectrics with low leakage. • Exhaustive list is provided in Appendix A.

2

DESIGN, ANALYTICAL AND FEM MODELING OF EHT INTEGRATED SENSORS

Prior to development of integrated sensors it is important to analyse the mechanical response of the EHT system presented in Chapter 1 in order to extract potential placement coordinates and dimensions of the sensor(s). The analytical results additionally serve as a model for validation of the simulated mechanical response. The geometrical characteristics of the pillars are shown in Fig. 2.1 and listed in Table 2.1. The interface of the pillar (green) is in continuum with that of the substrate (blue). In order to better understand the characteristics of the system, analytical equations have been derived in section 2.1 and results of the finite element modelling (FEM) of the system presented in subsection 2.1.1. The aim of this chapter can be sub-divided as follows.

- Analytical derivation of a generalised displacement equation for the mechanical behaviour of the soft PDMS substrate to which the micropillars are attached.
- Design as well as multiphysics modeling of test sensors utilising piezoelectric, piezoresistive and capacitive transduction modalities.
- Design of integrated co-planar capacitive sensors using COMSOL and Co-planar Waveguide (CPW) theory.
- Qualitative as well as quantitative comparative analysis of the proposed sensors.
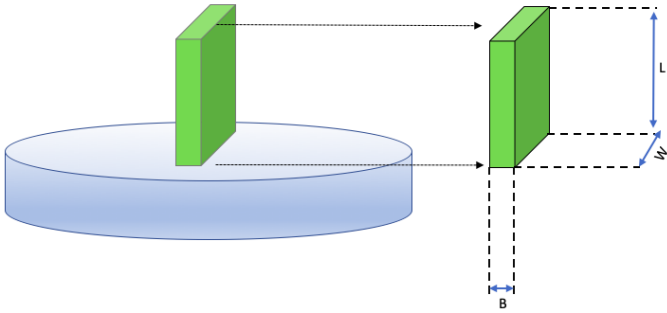
Figure 2.1: Sketch of single-pillar in contact with PDMS substrate.

Table 2.1: Geometrical properties of micropillars P1, P2 and P3 after scaling down of the Heart Dyno system.

Variable	Description	Value		
		P1	P2	P3
L	length	700 μm	560 μm	450 μm
B	breadth	191 μm	169 μm	137 μm
W	width	478 μm	423 μm	343 μm

The dimensions of the pillars have been scaled down from the Heart Dyno system so as to maintain the same pillar stiffness while reducing pillar volume [37]. This approach is utilised so as to test tissue properties at lower scales where device fabrication can be achieved by clean room processing. The volume of the micropillar is correlated to the number of heart cells in the well wherein P1, P2 and P3 are associated with 47000, 31000 and 16000 cells respectively [37].

2.1. ANALYTICAL CHARACTERIZATION OF MICROPILLARS

In order to better understand the reaction of the substrate to external forces, a boundary load of 10 μN is applied at the top boundary of the pillar as shown in Fig. 2.2 which can be considered as the lower limit of contraction force generated due to cardiac tissue [47]. The behaviour of the composite pillar-substrate structure can be split into two coordinate systems.

- (x,y,z): Coordinate space containing the un-deformed body
- (a,b,c): Coordinate space containing the deformed body arising in the continuum due to the resulting stress.

The force applied at the top of the pillar leads to the generation of reaction forces per unit area in the substrate which cause deformation within the substrate. Alternative models to beam theory are required since the rigid substrate assumption is no longer valid.
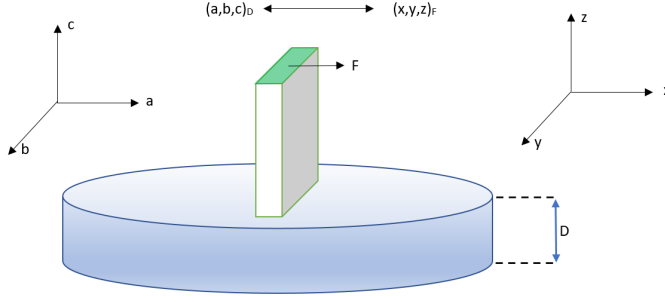
Figure 2.2: Boundary load, F, applied to a pillar in continuum with a soft substrate of height, D.

Table 2.2 lists the necessary material properties of PDMS which are required to further quantify the deformation of the substrate wherein Young's Modulus and Poisson's ratio are denoted by Y and v respectively. The moment of inertia and the torque acting on the pillar is calculated using the equations 2.1 and 2.2, respectively

$$M = \frac{B^3 W}{12} \tag{2.1}$$

$$T = FL \tag{2.2}$$

Table 2.2: Material Properties of PDMS.

Property	Value
Young's Modulus	1.7 MPa
Poisson's ratio	0.5
D	$300\ \mu m$
M_{P1}	$2.775 \cdot 10^8\ \mu m^4$
M_{P2}	$1.7015 \cdot 10^8\ \mu m^4$
M_{P3}	$7.3498 \cdot 10^8\ \mu m^4$

The mathematical analysis carried out assuming a soft substrate is based on studies performed by Kajzar et al. and Ingmar et al. which approximate the forces derived during cellular microscopy to be as high as 40% larger than estimated with rigid beam theory, in micropillar systems[48][49]. The vertical displacement in the substrate is given by Eq. 2.3 wherein G represents the tensor which maps the deformed space (a,b,c) to the undeformed space (x,y,z) while f represents the reaction forces per unit area arising in the substrate due to the applied boundary load [48]. Kajzar et al. have previously analysed the displacement arising the substrate due to equations derived from small strain theory and their approach has been utilised for deriving the behaviour of the substrate-pillar interface arising due to the miniaturized EHT platform.

$$\vec{d_z}(a,b) = \iint_A \vec{G}(a-x, b-y)\vec{f}(x,y)dxdy \tag{2.3}$$

and the tensor is expanded as follows:

$$\vec{\vec{G}} = \begin{pmatrix} L_1 - \frac{a^2-b^2}{\sqrt{a^2+b^2}}L_2 & \frac{-2ab}{\sqrt{a^2+b^2}}L_2 & 0 \\ \frac{-2ab}{\sqrt{a^2+b^2}}L_2 & \frac{a^2-b^2}{\sqrt{a^2+b^2}}L_2 & 0 \\ 0 & 0 & L_3 \end{pmatrix} \tag{2.4}$$

$$L_1 = \frac{(1+v)(2-v)}{2\pi Y \sqrt{a^2+b^2}} \tag{2.5}$$

$$L_2 = \frac{(1+v)(v)}{2\pi Y \sqrt{a^2+b^2}} \tag{2.6}$$

$$L_3 = \frac{2(1-v^2)}{2\pi Y \sqrt{a^2+b^2}} \tag{2.7}$$

On further expansion, the vertical surface displacement (d_z) is given by integrating the tensor along the breadth and the width of the pillar, assuming perfect continuity between the pillar and the substrate [48].

$$d_z = n \int_{a/B-0.5}^{a/B+0.5} dk \int_{b/W-0.5}^{b/W+0.5} \frac{\frac{a}{B}-k}{\sqrt{k^2+l^2}} dl \tag{2.8}$$

The tensor and displacement of the substrate are related via n, a proportionality constant which is dependent on the geometry as well as the material of the continuum. It is written as shown in Eq. 2.9.

$$n = \frac{3B^2 T}{4\pi Y M} \tag{2.9}$$

The solution of Eq. 2.8 is a piece-wise higher-order polynomial which cannot be solved without computational aid. The function is solved by utilizing the Symbolic Toolbox of MATLAB and further simplified to include only the region of interest (ROI) shown in Fig. 2.3. This corresponds to the z = 0 plane at the intersection of the pillar with the substrate. The MATLAB derived closed form of the solution of Eq. 2.8 is presented in Appendix B for reference.
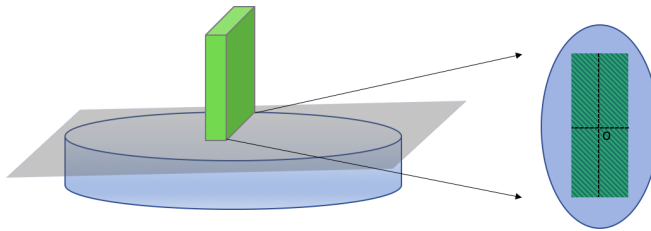
Figure 2.3: Pillar-interface ROI (z = 0) as indicated by the shaded region with the origin at *O*.

The vertical displacement of the substrate is shown in Fig. 2.4. Pillar, P1 has been chosen for analysis and a force of $10\mu N$ has been applied as a boundary load. The figure highlights the anti symmetric nature of the substrate about the neutral axis (indicated by the black line at the center of the curve).
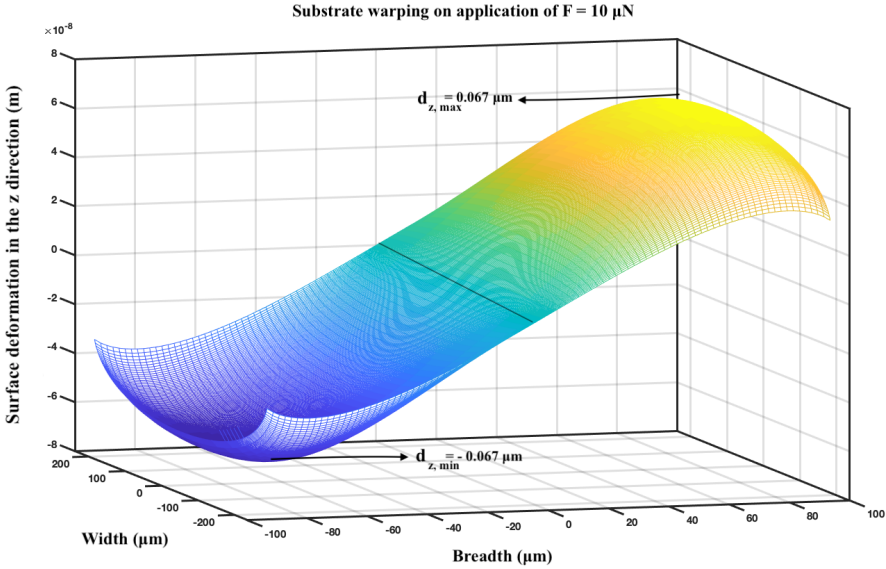
Figure 2.4: Vertical displacement of the substrate due to a boundary load of $10\mu N$ at the pillar top.

2.1.1. FINITE ELEMENT MODELLING

The mechanical response of the system has been analysed using the Solid Mechanics module in COMSOL v5.4. The meshing of the pillar-substrate interface is shown in Fig 2.5. The accuracy is further improved by assigning a cubic discretization to the dependent variables. This generates a higher number of nodes in the system at the cost of increased simulation time. The complete simulation flow is shown in Fig. 2.6.
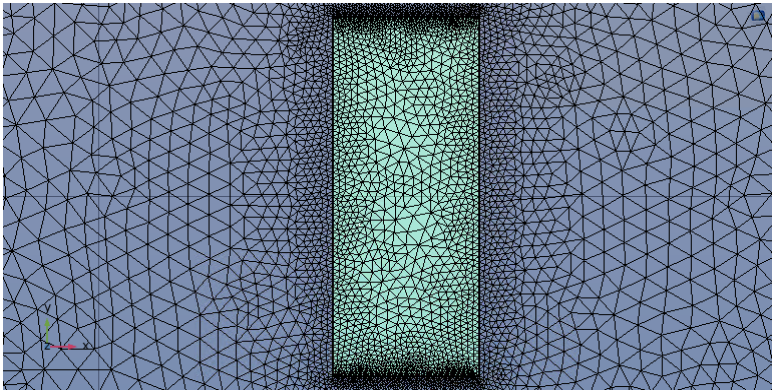
Figure 2.5: Meshing of contact between pillar and substrate.

The response of the system has been characterised using the following variables:

- Pressure (P) $[\frac{N}{m^2}]$

- Vertical Displacement (d_z) $[\mu m]$

- Auxiliary volumetric strain (ϵ_{ax}) [1]. This unit is selected since constitutive relations utilising strain express the variable as a unitless quantity of '1'.

```
                    ┌─────────────────────┐
                    │  Boundary System    │
                    │     Cartesian       │
                    └─────────────────────┘
```

Boundary System
Cartesian

Physics
Solid Mechanics

Material Model
Isotropic linear elastic material with strain mixed formulation

Mesh
- Upper boundary of substrate: Extra fine, free triangular mesh. Distribution of 30 elements across each edge of pillar-substrate interface with an element ratio of 1 and a geometric growth formula.
- Substrate domain: Extra fine, free tetrahedral
- Pillar domain: Extra fine, free tetrahedral

Study and Solver
Stationary (including geometric non-linearity) with Direct, Fully Coupled solver

Dependent variables
- Displacement field
- Auxiliary volumetric strain

Figure 2.6: Solid Mechanics simulation flow.

The auxiliary volumetric strain is linked to the total volumetric strain via Eq 2.10 [50].

$$K(\epsilon_{ax} - \epsilon_1 - \epsilon_2 - \epsilon_3) = 0 \qquad (2.10)$$

where K and $\epsilon_{1,2,3}$ are the bulk modulus and the principle strains of the system, respectively. In order to better understand the role played by the principle stress-strain variables of the system, the normal ($\sigma_{ii}, i = 1, 2, 3$) and transverse ($\sigma_{ij}, i, j = 1, 2, 3$) stress components acting on the face of a cube are shown, resulting from external forces acting on all the faces of the cube as seen in Fig. 2.7a and Fig. 2.7b.

2

Figure 2.7: Representation of various stress components acting on an elastic material A) Original co-ordinate system with non-zero shear components. B) Equivalent co-ordinate system with no shear components.

The response of the system in the geometry frame (A_1, A_2, A_3) can be set equivalent to a spatial coordinate system (A_1', A_2', A_3') wherein the shear stress in the system is equal to 0. The resulting normal stress-strain components are known as principle stresses and strains. The three principle strains are denoted by:
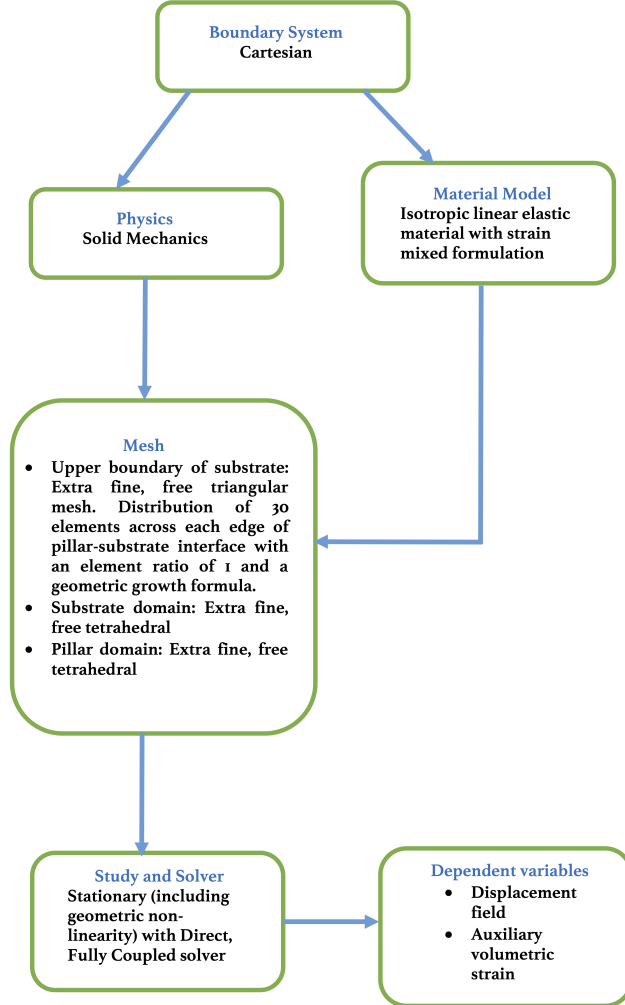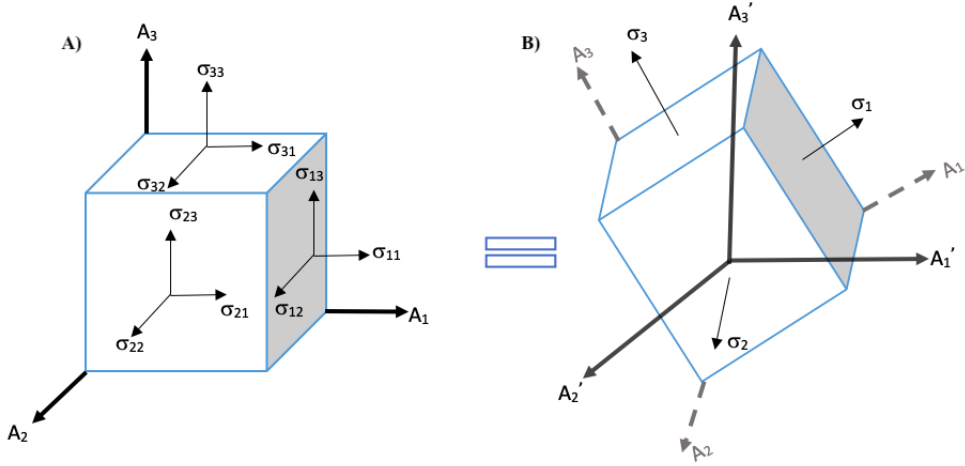
- ϵ_1: First principle strain, most expansive.

- ϵ_2: Second principle strain, both compressive and expansive.

- ϵ_3: Third principle strain, most compressive.

Analysis of the individual strain components in COMSOL for the micropillar system under consideration shows that the second principle strain at the pillar-substrate is 40 times lower in magnitude than the first and third principle strains of the system. The variables of interest have been plotted along cut-lines drawn at the pillar-substrate interface as well as along the depth of the substrate to demonstrate the behaviour of the variables across the dimensions of the system. In order to validate the simulated response, a cut-line has been drawn through the origin along the breadth of the pillar as shown in Fig. 2.8. The origin has been placed on the neutral axes of the pillar and forces of 500 μN and 10 μN have been applied along the positive x-direction. *It can be seen that the solution of Eq. 2.8 is in excellent agreement with that of the simulated results, portrayed in Fig. 2.9a and 2.9b.* The origin of the co-ordinate system is placed at the intersection of the neutral axes of the pillar. Henceforth, the behaviour of the dependent

variables is analysed in the co-ordinate system shown in Fig. 2.8. Cut-lines are also de-
fined within the substrate along the z-axis of the co-ordinate system.

The response of the dependent variables is shown in figures 2.10-2.12. For all further
analysis, the pillar of largest volume (P1) has been chosen since pillar volume is in di-
rect correlation with the volume of subsequent tissue growth [37]. The distance (in μm)
between each cut-line has been defined by "Distance" with respect to the origin with
a distance of 0 corresponding to the cut-line through the origin (indicated by a yellow
line). The direction of the force is indicated by the arrow above the pillar. The neutral
axes along the width and breadth are denoted by dotted lines with the origin assigned
at their intersection. All x- and y- cutlines lie on the plane z = 0 which is at the interface
of the pillar and the underlying substrate. The value of **F** has been fixed at 10 μN for all
analyses.
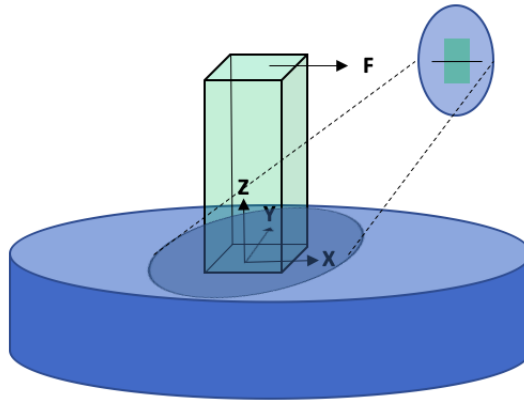
Figure 2.8: Cut-line through origin along breadth of pillar.
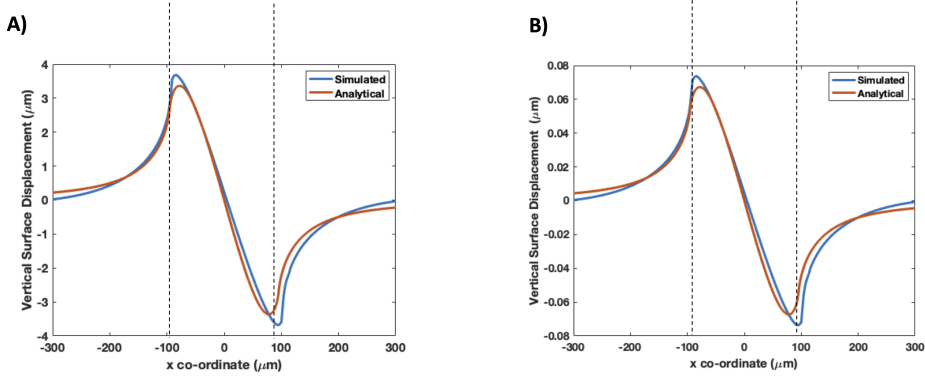
Figure 2.9: Vertical displacement of the substrate along cut line through the origin A) When F = 500 μN B) When F = 10 μN (Dashed lines: Pillar edges).

The relative error between the analytical and simulated displacements in the soft elastic substrate is less than 5% for a low force of $10\mu N$ and for a high force of 500 μN. The source of the error can be attributed to the following factors:

- The simulated PDMS cannot have a Poisson's ratio (v) of 0.5 since this leads to an instability in the solver and an inability to reach convergence. This is linked to the bulk modulus of the system which becomes infinity due to its inverse proportionality to (1-2v). Hence a Poisson's ratio of 0.49 has been defined.

- A Hookean model is assumed in the COMSOL simulations. When the Poisson's ratio is close to 0.5 (0.45-0.49), the system can alternatively be defined as a nearly in-compressible neo-Hookean solid [51]. It must be kept in mind that the accuracy of this model is based on accurate measurements of the Poisson's ratio of PDMS. The approximation of the system as linearly elastic (Hookean) has been tested for tissues applying forces as high as $500\mu N$. The relative error does not change when the force is varied as tested for two extreme cases (F = 500 μN and F = 10 μN) illustrated in Fig. 2.9a and Fig. 2.9b.

The response of the mechanical dependent variables are shown along the breath and width of the pillar as well as the depth of the substrate as shown in Fig. 2.10, Fig. 2.11 and Fig. 2.12 respectively.

Figure 2.10: Variation of dependent variables along the breadth of the pillar (F=10μN).

The following observations can be made:

- The vertical displacement field, pressure and auxiliary volumetric strain are anti symmetric with respect to the neutral axis drawn along the width.

- The pressure and auxiliary volumetric strain are anti symmetric with respect to each other. This is because as the pressure on the volume increases, the volume compresses and vice versa.
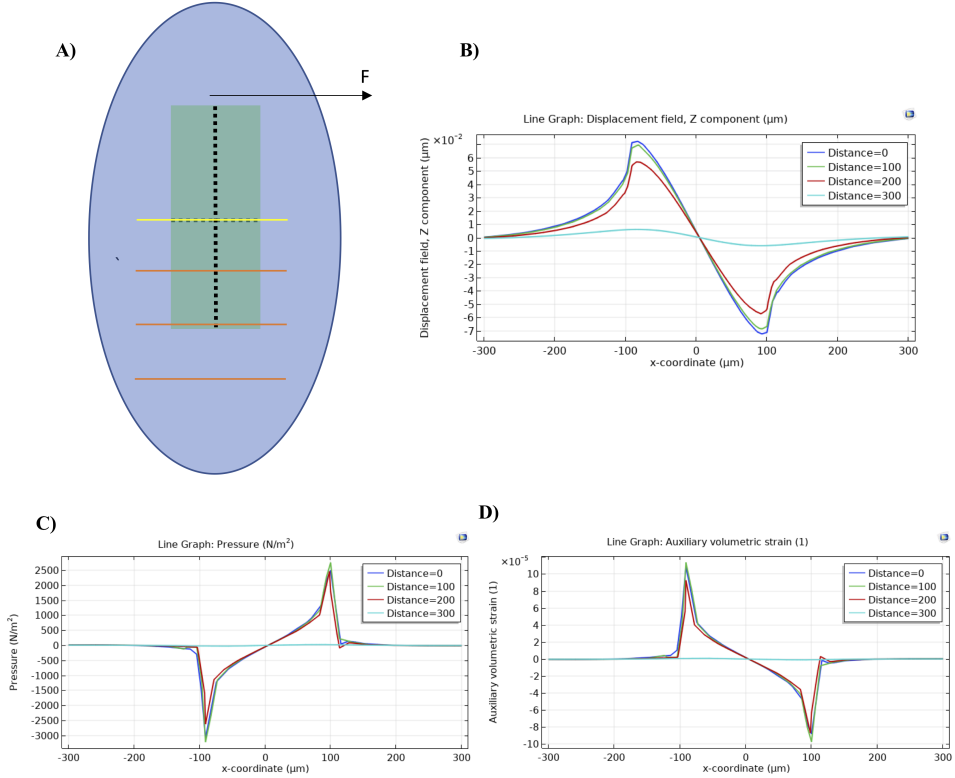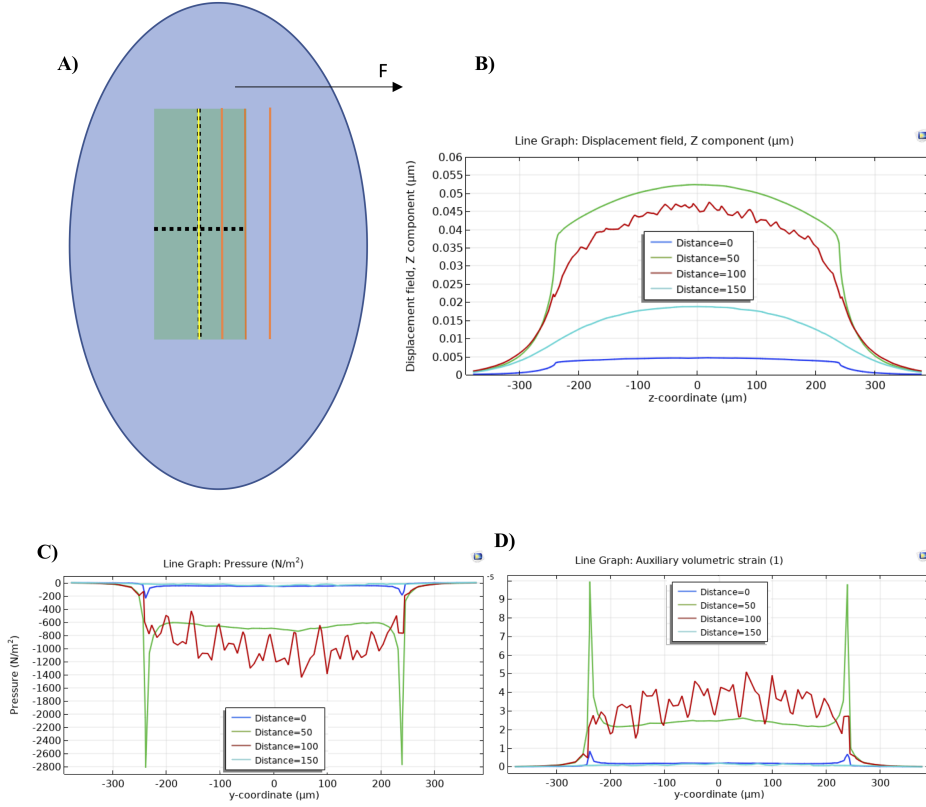
Figure 2.11: Variation of dependent variables along the width of the pillar (F=10μN).

The following observations can be made:

- The vertical displacement field, pressure and auxiliary volumetric strain are symmetric with respect to the neutral axis drawn along the breadth.

- The pressure and auxiliary volumetric strain are anti symmetric with respect to each other.
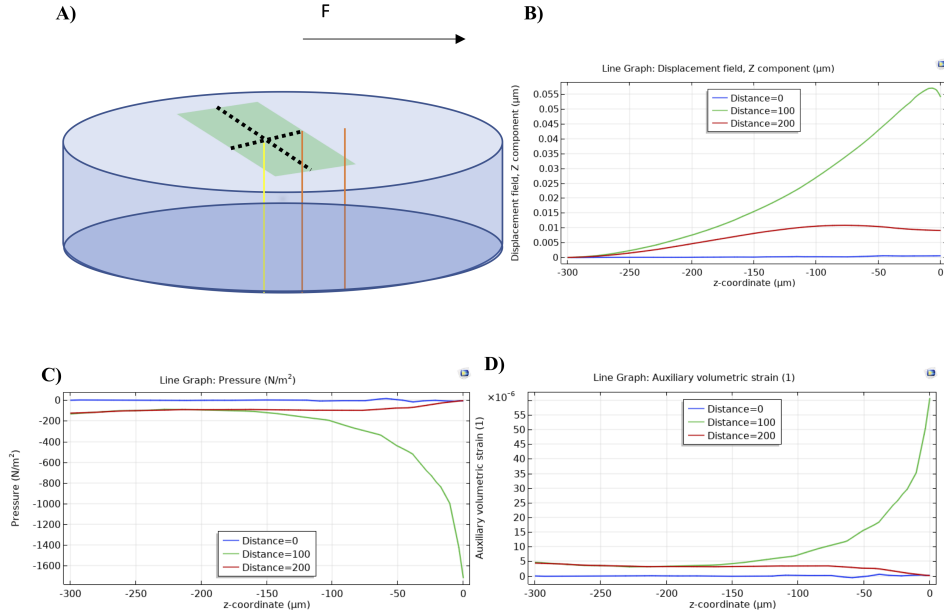
Figure 2.12: Variation of dependent variables along the depth of the substrate (F=$10\mu N$).

The following observations can be made:

- There is an exponential drop in all the variables of interest, along the depth of the substrate.

- The pressure and auxiliary volumetric strain are anti symmetric with respect to each other.

2.1.2. DESIGN CONSIDERATION FOR SENSOR DEVELOPMENT

On account of the exponential drops in the mechanical dependent variables along the depth of the substrate, the sensor should be placed as close to the z = 0 plane as possible and ideally at the z = 0 plane. However, the sensor will be exposed to the surrounding cellular culture media which is not preferable since the sensor material could adversely effect cellular growth. From a fabrication perspective, position of the patterned sensors along the depth of the system is limited by the minimum layer thickness which can be obtained during spin-coating and/or etching of PDMS without generation of non-uniformities which have the capability of effecting the efficiency of sensor patterning.

When considering the x-y plane, the electrical response of the sensor(s) would be intuitively anti symmetric across the neutral axis of the pillar drawn along its width based on the observations deduced in subsection 1.1.1 and shown in Fig. 2.10. Hence the sensor should not cross this neutral axis of the pillar. Due to the symmetric nature of the dependent variables across the neutral axis drawn along the breadth, the sensor can safely

occupy the entire area along the width of the pillar without loss in sensitivity. The pro-
posed positions are shown in Fig. 2.13 wherein the neutral axes are shown by dotted
lines, the sensors by blue frames, and the edges of the pillar outlined with solid black
lines.
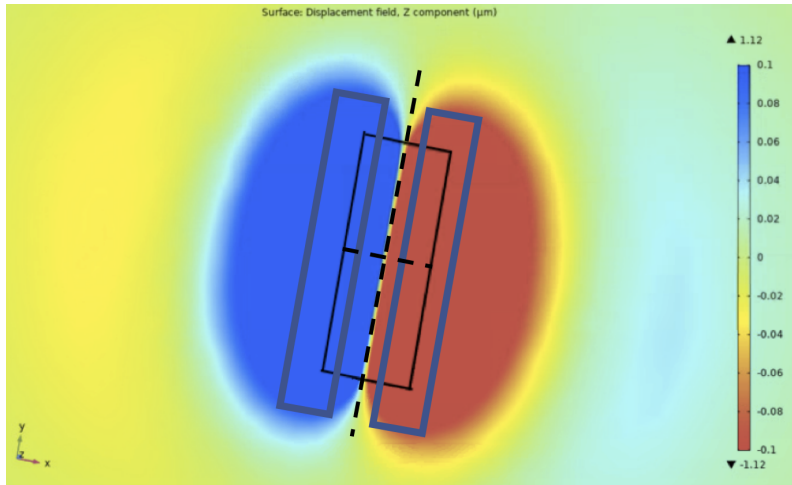
Figure 2.13: Surface-displacement under single pillar [edges of pillar are denoted by the black outline and
neutral axes by dotted lines]. The sensors [blue frames] lie on either side of the longer edges of the pillar.

2.2. TEST SENSOR DESIGN AND ANALYSIS

In order to extract the full potential of the integrated sensors, they are designed and
placed in such a manner so as to enable differential measurement techniques. This is
shown in Fig. 2.14. Owing to the anti symmetric nature of the dependent variables
across the neutral axes of the pillars, the transduction provided by the sensors is anti
symmetric as well i.e. sensors placed at positions S1 and S4 exhibit electrical changes
which are equal and opposite to sensors placed at positions S2 and S3. For all test sensor
designs, single-pillar simulations are carried out with S2 as the sensor position of choice.
It is placed on the substrate at the z = 0 plane to allow for uniform swept meshing within
the substrate as shown in Fig. 2.15a. The sensor is 1 μm in thickness which enables the
addition of a tetrahedral mesh to the sensor domain without increasing the simulation
time. Modeling of sensors of width less than 500 nm embedded within the substrate will
be discussed in section 2.6. Three modifications have been made to the system and its
simulations as compared to the platform utilised for analytical studies. Materials un-
der the MEMS and semiconductor modules of COMSOL have been utilised with in-built
properties pre-defined in the database.

- Rectangular pillars are replaced with pyramidal pillars to account for alterations
  during micro-fabrication. The ratio of the top and bottom surface perimeter is
  0.9.
- Since cardiac tissue wraps around the pillars, the top boundary load has been re-
  placed with a surface load of 100 μm width attached at one-third of pillar height
  from the top [48].

- Cubic discretization has been replaced with quadratic in order to reduce the number of nodes within the system. This is ideal for multiphysics couplings, albeit it leads to a drop in model accuracy. For the sake of uniformity this approach has been used in all test sensor designs.
- The electrical output of the test sensors exhibits a linear relationship with the applied force and the slope is utilised for calculating the sensitivity of the sensors. As an example, a test sensor of which the resistance changes is integrated with the EHT platform as shown in Fig. 2.15b. The slope is calculated as $\frac{264.3359 - 264.3356}{100 - 50} =$ $6\Omega/N$. The piezoresistive test sensor is further discussed in section 2.4.
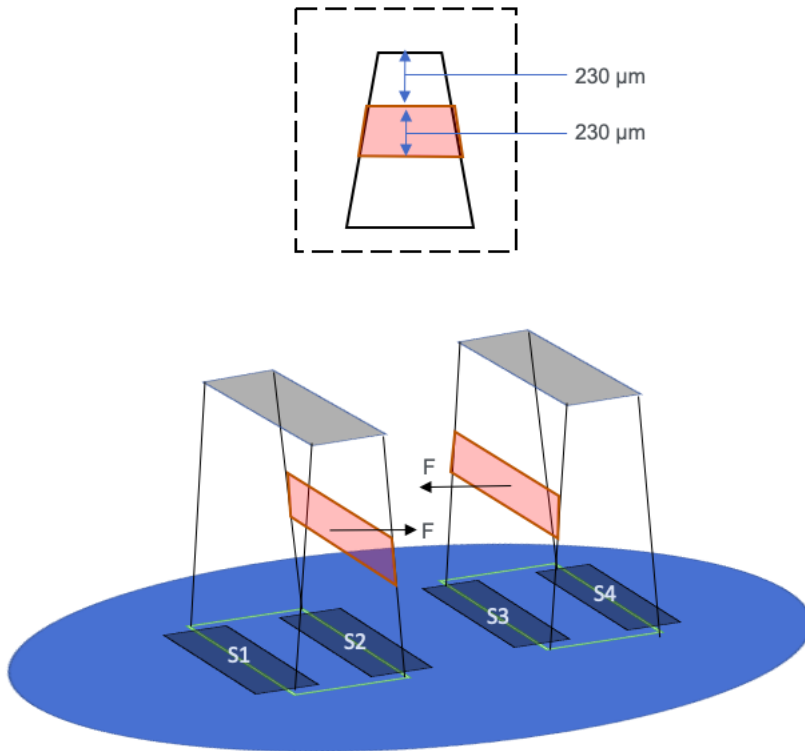
Figure 2.14: Placement of sensors on the EHT platform. The direction of force is denoted by F and is considered as a boundary load as shown in the inset. Sensors placed at positions S2 and S3 are expected to show an anti symmetric response to sensors placed placed at S1 and S4.
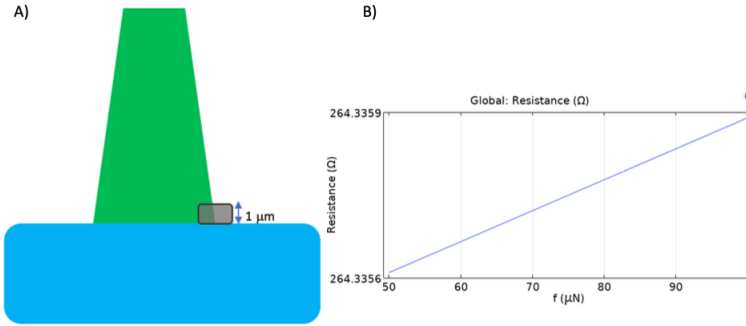
Figure 2.15: A) Single sensor placement under pillar [side-view] B) Change in resistance of test sensor vs applied force. The slope of the graph is utilised for deriving sensitivity of sensors.

2.3. PIEZOELECTRIC SENSOR

Piezoelectric sensors were chosen as the first step towards measuring the contractile forces generated by cardiac tissue on the EHT platform. Based on the previously performed mechanical analysis in sections 2.1 and 2.2, the sensor is placed on the substrate at the edge of the pillar as shown in Fig 2.14, denoted by the position-symbol S_2. The dimensions of the sensor are chosen in such a way so as to occupy all areas wherein the dependent variables are non-zero without any cross-over across the neutral axis of the pillar represented by the dotted line as shown in Fig. 2.16. This is done so as to prevent any reductions in sensitivity which might arise due to the anti symmetric nature of the mechanical dependent variables across the neural axis of the pillar.
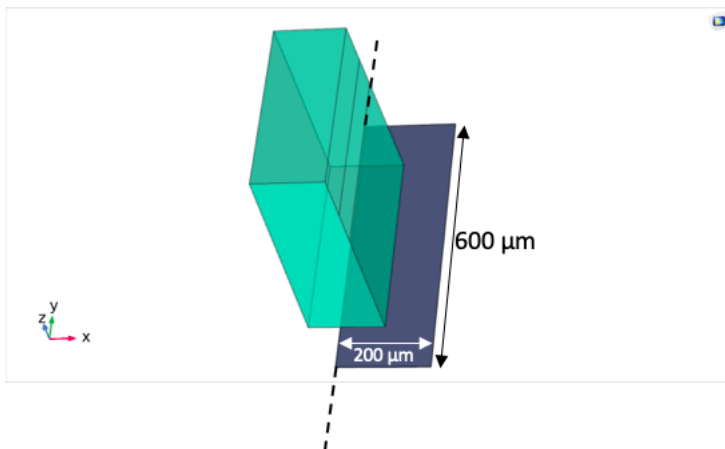
Figure 2.16: Position and dimensions of integrated piezoelectric test sensor.

2.3.1. Finite Element Analysis

The sensor material chosen for this analysis is polyvinylidene difluoride (PVDF), a bio-compatible polymer commonly used in industries for the fabrication of bearings and pipes [52]. In order to couple the dependent variables in the mechanical domain with that of the electrical domain, the strain-charge coupling relation using Eq. 2.11a and 2.11b [53].

$$\epsilon = s_E \sigma + dE \tag{2.11a}$$

$$D = d\sigma + \epsilon_0 \epsilon_r E \tag{2.11b}$$

The material properties s_E, d and ϵ_r are the compliance matrix, coupling matrix, and relative permittivity of the piezoelectric material. The stress applied to the sensor due to bending is denoted by σ and the subsequent strain is denoted by ϵ. The variables E and D are assigned to the dynamic electric field and displacement field generated by the sensor with the permittivity of air denoted by ϵ_0. The strain-charge form is hence utilised to emulate the changes in charge distributions within the material due to the strain in the PDMS substrate.

Table 2.3 highlights the properties of the tensors which couple the mechanical and electrical domains together.

Table 2.3: Properties of PVDF piezoelectric test sensor.

Variable	Value						Unit
s_E	$\begin{pmatrix} 3.78\cdot10^{-10} & -1.482\cdot10^{-10} & -1.724\cdot10^{-10} & 0 & 0 & 0 \\ -1.482\cdot10^{-10} & 3.781\cdot10^{-10} & -1.724\cdot10^{-10} & 0 & 0 & 0 \\ -1.724\cdot10^{-10} & -1.724\cdot10^{-10} & 1.092\cdot10^{-9} & 0 & 0 & 0 \\ 0 & 0 & 0 & 1.428\cdot10^{-9} & 0 & 0 \\ 0 & 0 & 0 & 0 & 1.11\cdot10^{-9} & 0 \\ 0 & 0 & 0 & 0 & 0 & 1.11\cdot10^{-9} \end{pmatrix}$						1/Pa
d	$\begin{pmatrix} 0 & 0 & 0 & 0 & 0 & 0 \\ 0 & 0 & 0 & 0 & 0 & 0 \\ 1.358\cdot10^{-11} & 1.476\cdot10^{-12} & -3.38\cdot10^{-11} & 0 & 0 & 0 \end{pmatrix}$						C/N
ϵ_r	$\begin{pmatrix} 7.4 & 0 & 0 \\ 0 & 9.3 & 0 \\ 0 & 0 & 7.74 \end{pmatrix}$						1
ν	0.34						1
Y	1.1						GPa

In order to measure the change in the voltage within the sensor, it is connected, in a closed circuit to non-zero inputs, to a driving voltage (V_{src}) of a sine wave of 1 V_{pp}, frequency equal to 1 kHz and a resistor (R) of 1kΩ as shown in Fig. 2.16. The second port of the sensor is connected to a variable floating potential, V_{f1}. Changes in the driving voltage and resistance do not theoretically effect the sensitivity of the sensor and are merely used for generation of a closed circuit [54].
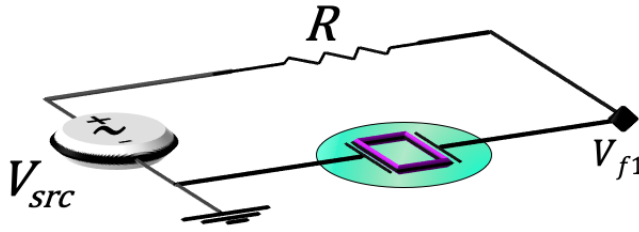
Figure 2.17: Circuit configuration for PVDF piezoelectric sensing.

Since, the change in the potential of the sensor is due to polarization within the domain elements, an external medium of air is not defined to account of subsequent changes in the electric field around the sensor. This aids in reducing the degrees of freedom in the system thereby reducing computation time. The complete simulation flow is shown in Fig. 2.18. On the application of the boundary load of 10 μN, there occurs a displacement within the sensor with the maxima at approximately the center of the sensor as seen in Fig. 2.19. The peak of the harmonic output of the sensor varies at the rate of 0.05 nV/N when considering position S1 and -0.05 nV/N when considering position S2. The lower sensitivity obtained as compared to commonly used piezoelectric materials like PZT [55] can be attributed to two factors:

- The low strain transfer from the substrate to the sensor. The stiffness of the sensor is three orders of magnitude higher than the PDMS substrate which leads to a reduction of the effective gauge factor of PVDF.

- Polymeric materials are not well suited for high sensitivity piezoelectric applications due to their low piezoelectric coefficients which are denoted individually in the coupling tensor, $\boldsymbol{d}$. Alternative materials such as Lead Zirconate Titanate (PZT) demonstrate higher sensitivities and piezoelectric coefficients an order of magnitude higher than polymeric materials. However due to the high lead content of these materials, they do not exhibit bio-compatibility.

Boundary System
Cartesian

Physics
- **Solid Mechanics (SM)**
- **Electrostatics (ES)**
- **Electrical Circuit (EC)**

Multiphysics
Piezoelectric Effect

Material Models (SM)
- **PDMS: Isotropic linear elastic material with strain mixed formulation and quadratic serendipity**
- **PVDF: Piezoelectric material**

Electrical Models (ES)
- **PDMS domain: Solid charge conservation**
- **PVDF domain: Piezoelectric solid charge conservation**
- **Top PVDF surface: Floating potential**
- **Bottom PVDF surface: Ground**

Mesh
- **Upper boundary of substrate: Extra fine, free triangular mesh. Distribution of 30 elements across each edge of pillar-substrate interface with an element ratio of 1 and a geometric growth formula.**
- **PVDF Domain: Extra fine, free tetrahedral**
- **Substrate domain: Extra fine, swept**
- **Pillar domain: Extra fine, free tetrahedral**

Dependent variables
- **Displacement field**
- **Auxiliary volumetric strain**
- **Electric Potential**
- **Charge**
- **Floating potential**

Study and Solver
Stationary (including geometric non-linearity) with Direct, Fully Coupled solver
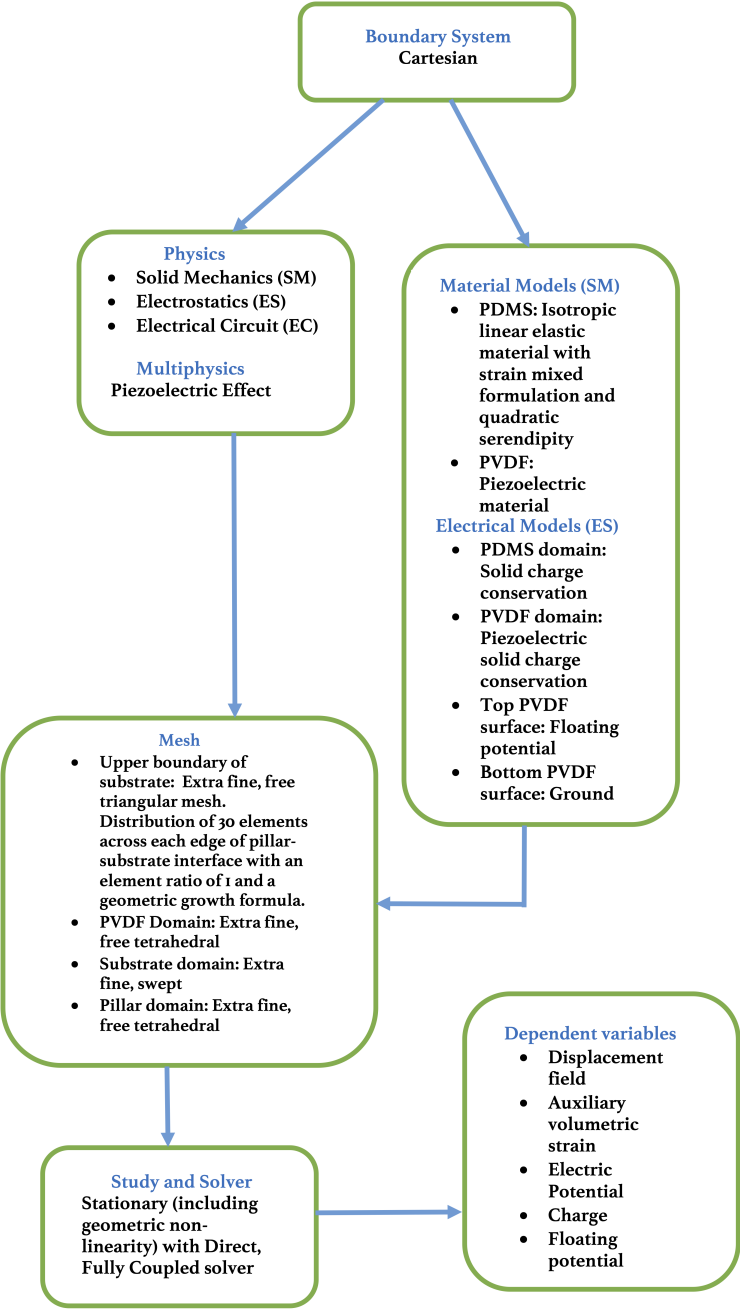
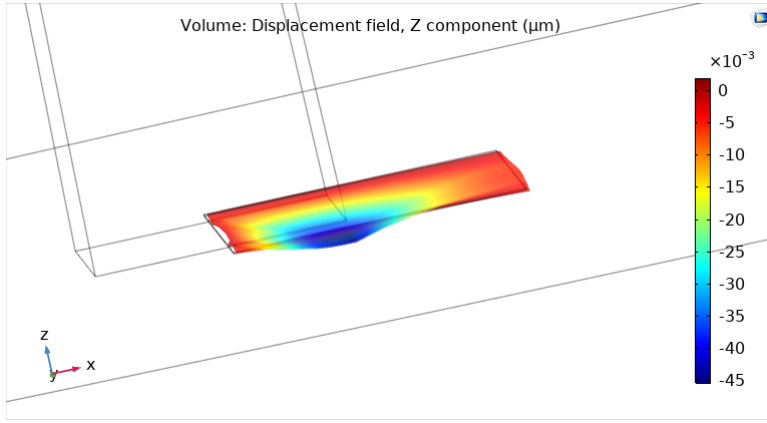Figure 2.18: Simulation flow for piezoelectric sensor.

Figure 2.19: PVDF deformation due to pillar boundary load, F = 10 μN.

The second test has been performed on a piezoresistive sensor as an attempt to utilize a sensor with higher coupling coefficients and by extension a higher gauge factor.

2.4. PIEZORESISTIVE SENSOR

Strain gauges fabricated using piezoresistive materials exhibit a change in their resistance due to deformations in the material. This is shown mathematically in equations 2.12 and 2.13[56]. Due to the anisotropic nature of the sensor, the gauge factor is dependent on crystallographic orientation [56].

$$\frac{\Delta R}{R} = GF \cdot \frac{\Delta L}{L} \tag{2.12}$$

$$GF = 1 + 2\nu + \frac{\Delta \rho}{\rho} \tag{2.13}$$

The resistance of a material is defined as its resistivity times the length of the material per unit area. In materials such as metals, their piezoresistive behaviour is primarily linked to the change in their geometrical dimensions while in semiconducting materials, the relative movement of valence and conduction bands in different crystal directions additionally leads to a change in the resistivity of the material [56]. For this reason, semiconductors are the first material of choice for detecting low strains due to a gauge factor (GF) which is two orders of magnitude higher than those of metals [56].

2.4.1. FINITE ELEMENT ANALYSIS

In order to couple the contractile force with the piezoresistive sensor, the strain within the substrate is primarily relied on. As seen in Fig. 2.20 the drop in the strain within the system is steep with the individual principle strains rapidly dropping to 0 as shown in Fig. 2.20. Hence, the width of the sensor has been reduced to occupy the area with the maximum gradient in the strain which is highlighted in Fig. 2.20. This reduces the width of the sensor while simultaneously reducing computation time. Semiconductors like mono-crystalline and poly-crystalline silicon exhibit anisotropic piezoresistivity along

different directions within the crystals of the materials as seen in Fig. 2.21 [57]. The overall gauge factor depends on the orientation of the crystals with respect to the longitudinal, transverse and shear strain components present within the system [57].
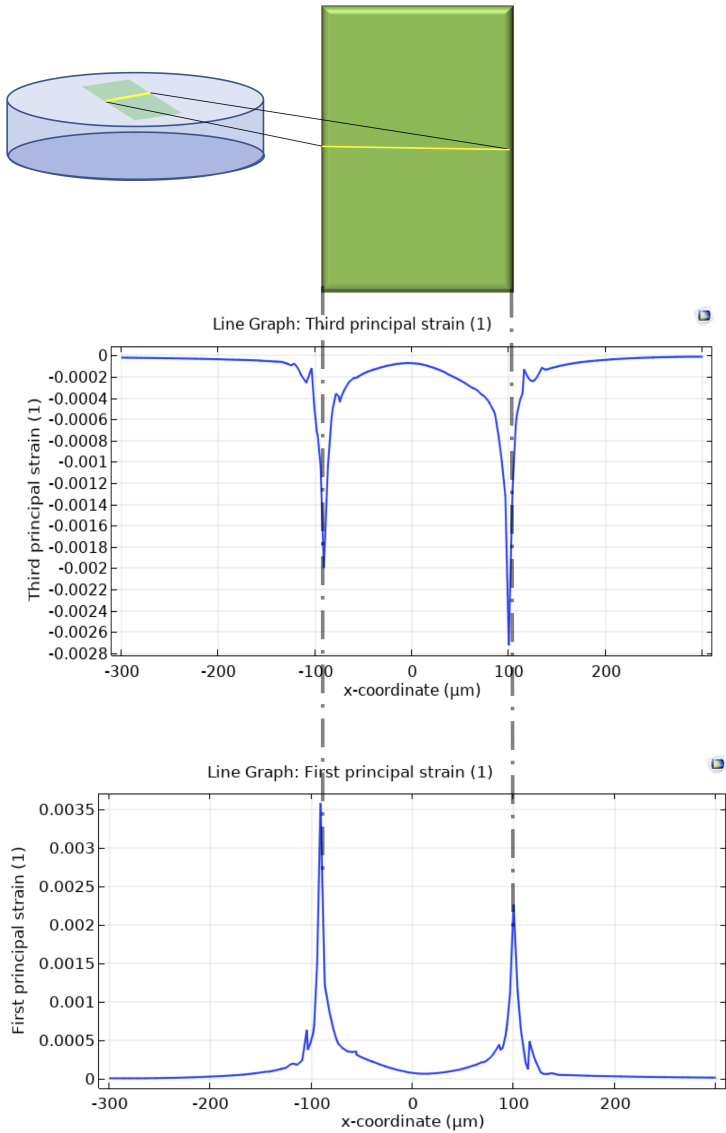

Figure 2.20: Principle strain distribution at substrate-pillar interface. The first principle strain is representative of the expansive deformation while the third principle strain is representative of compressive deformation.

Stresses direction	Current direction	Configuration	Piezoresistives coefficients		Piezoresistive coefficient	p-Si (resistivity =7.8Ω cm)
<100>	<100>	Longitudinal	π_{11}		π_{11}	6.6
<100>	<010>	Transversal	π_{12}			
<110>	<110>	Longitudinal	$(\pi_{11}+\pi_{12}+\pi_{44})/2$		π_{12}	-1.1
<110>	<1-1 0>	Transversal	$(\pi_{11}+\pi_{12}-\pi_{44})/2$			
<111>	<111>	Longitudinal	$(\pi_{11}+2\pi_{12}+2\pi_{44})/2$		π_{44}	138.1

Figure 2.21: Piezoresistive coefficients of Si based on crystal orientation [57].

The constitutive relations for the coupled interfaces are given in Eq. 2.14a and 2.14b [50].

$$\Delta\rho = \Pi \cdot \sigma \tag{2.14a}$$

$$\begin{pmatrix} \Delta\rho_1 \\ \Delta\rho_2 \\ \Delta\rho_3 \\ \Delta\rho_4 \\ \Delta\rho_5 \\ \Delta\rho_6 \end{pmatrix} = \begin{pmatrix} \pi_{11} & \pi_{12} & \pi_{12} & 0 & 0 & 0 \\ \pi_{12} & \pi_{11} & \pi_{12} & 0 & 0 & 0 \\ \pi_{12} & \pi_{12} & \pi_{11} & 0 & 0 & 0 \\ 0 & 0 & 0 & \pi_{44} & 0 & 0 \\ 0 & 0 & 0 & 0 & \pi_{44} & 0 \\ 0 & 0 & 0 & 0 & 0 & \pi_{44} \end{pmatrix} \cdot \begin{pmatrix} \sigma_1 \\ \sigma_2 \\ \sigma_3 \\ \sigma_4 \\ \sigma_5 \\ \sigma_6 \end{pmatrix} \tag{2.14b}$$

The change in resistivity ($\boldsymbol{\Delta\rho}$) is coupled to the stress tensor ($\boldsymbol{\sigma}$) via the piezoresistive coupling matrix ($\boldsymbol{\Pi}$). The stress vectors $\boldsymbol{\sigma_{1,2,3}}$ correspond to the normal stresses and $\boldsymbol{\sigma_{4,5,6}}$ to the shear stresses present in the Cartesian space of the silicon crystal. The coupling matrix is scaled by the resistivity, κ, of the sensor which in-turn depends on the impurity doping of the semiconductor, N_d [1]. Since the variable of interest is the strain ($\boldsymbol{\epsilon}$) generated within the sensor due to external stresses, the stress-strain coupling is done via the elasticity matrix ($\boldsymbol{E}$) as seen in Eq. 2.15.

$$\sigma = E.\epsilon \tag{2.15}$$

For the test sensor analysis, a p-type polycrystalline silicon sensor has been chosen due to its higher gauge factor as compared to n-type silicon [57]. The simulation flow is shown in Fig. 2.22 and the properties of this sensor are highlighted in Table 2.4.

---

[1]A low doping density has been chosen since the displacement of holes in the crystal bands due to strain increases as the number of charge carriers decreases. This leads to an increase in sensitivity [57].

Boundary System
Cartesian

Physics
- **Solid Mechanics (SM)**
- **Electric Currents (ECu)**

Multiphysics
Piezoresistive Effect,
Domain Currents

Material Models (SM)
- **PDMS: Isotropic linear elastic material with strain mixed formulation**
- **Polycrystalline p-type silicon: Piezoresistive material**

Electrical Models (ECu)
- **PDMS & Si domain: Solid current conservation**
- **Si domain: Piezoresistive material ($N_d = 10^{16}$ cm^{-3})**
- **Current through sensor: 5 mA**

Mesh
- **Upper boundary of substrate: Extra fine, free triangular mesh. Distribution of 30 elements across each edge of pillar-substrate interface with an element ratio of 1 and a geometric growth formula.**
- **Silicon Domain: Extra fine, free tetrahedral**
- **Substrate domain: Extra fine, swept**
- **Pillar domain: Extra fine, free tetrahedral**

Study and Solver
Stationary (including geometric non-linearity) with Direct, Fully Coupled solver

Dependent variables
- **Displacement field**
- **Auxiliary volumetric strain**
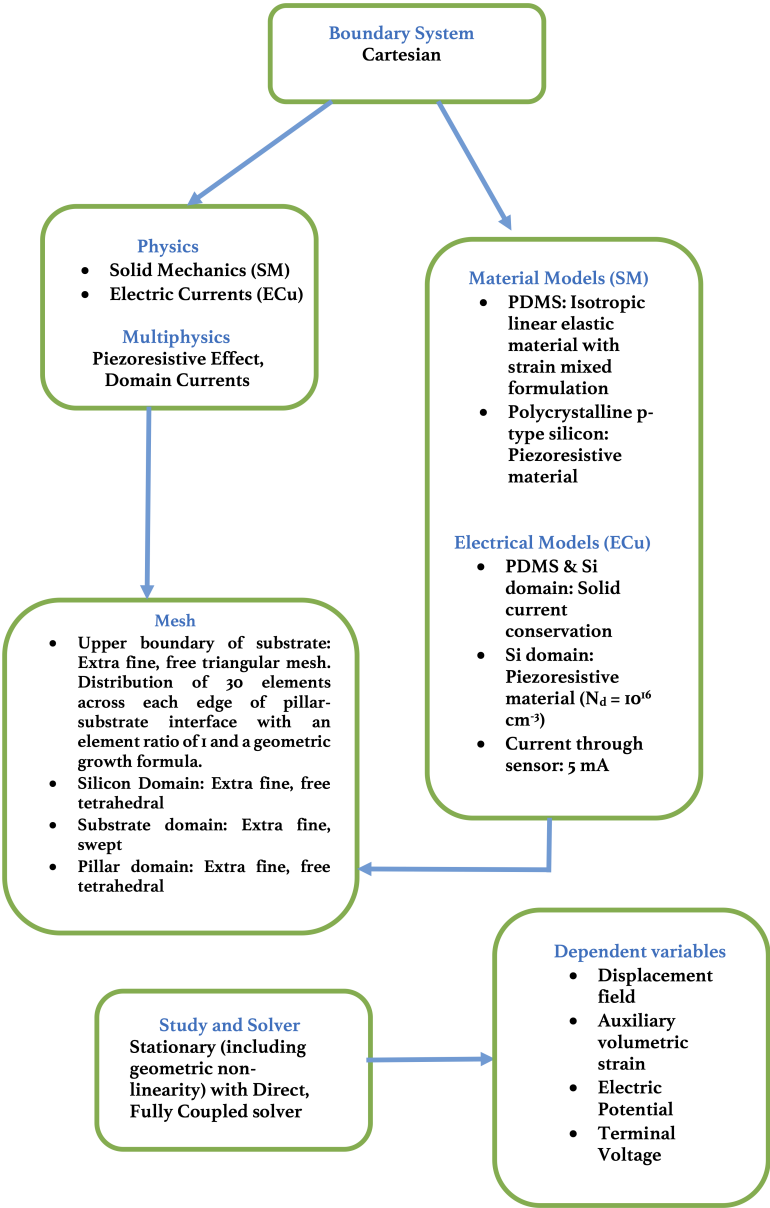- **Electric Potential**
- **Terminal Voltage**

Figure 2.22: Simulation flow for piezoresistive sensor.

Table 2.4: Properties of p-type Si piezoresistive test sensor.

Variable	Value						Unit
Π	$\begin{pmatrix} 58.8\cdot10^{-11} & -27.2\cdot10^{-11} & -27.2\cdot10^{-11} & 0 & 0 & 0 \\ -27.2\cdot10^{-11} & 58.8\cdot10^{-11} & -27.2\cdot10^{-11} & 0 & 0 & 0 \\ -27.2\cdot10^{-11} & -27.2\cdot10^{-11} & -58.8\cdot10^{-11} & 0 & 0 & 0 \\ 0 & 0 & 0 & 85.9\cdot10^{-11} & 0 & 0 \\ 0 & 0 & 0 & 0 & 85.9\cdot10^{-11} & 0 \\ 0 & 0 & 0 & 0 & 0 & 85.9\cdot10^{-11} \end{pmatrix} \cdot \kappa$						$\Omega\cdot m/Pa$
E	$\begin{pmatrix} 182.67 & 51.522 & 51.522 & 0 & 0 & 0 \\ 51.522 & 182.67 & 51.522 & 0 & 0 & 0 \\ 51.522 & 51.522 & 182.67 & 0 & 0 & 0 \\ 0 & 0 & 0 & 65.574 & 0 & 0 \\ 0 & 0 & 0 & 0 & 65.574 & 0 \\ 0 & 0 & 0 & 0 & 0 & 65.574 \end{pmatrix}$						GPa
ϵ_r	4.5						1
ν	0.22						1
Y	160						GPa
N_d	10^{16}						cm^{-3}

The gauge factor of the simulated sensor can be calculated using the following equation [58]:

$$GF = \frac{\pi_{11} + \pi_{12} + \pi_{44}}{2} Y = 95 \qquad (2.16)$$

The design of the sensor was inspired by Yongdae et al. which accounts for both longitudinal and transverse strain components within the system, as shown in Fig. 2.23 [59]. A sensitivity of -3 Ω/N is observed in position S1 while the sensor placed at position S2 exhibits a sensitivity of 3 Ω/N. The anti symmetric nature of the piezoresistive response can be utilised to construct the read-out circuitry shown in Fig. 2.4 with R($\pm\epsilon$) account for piezoresistors at S1 and S2 [60]. The two arms of the bridge which account for a *constant* resistance (R) can be realised by fabricating resistors on the PDMS substrate wherein the value of the mechanical dependent variables is zero. In order to emulate the response of the sensor domain with respect to PDMS, the resulting strain has been plotted within the two materials as shown in Fig. 2.23c. The response verifies the effect of direct integration of high stiffness sensors with polymeric domains.
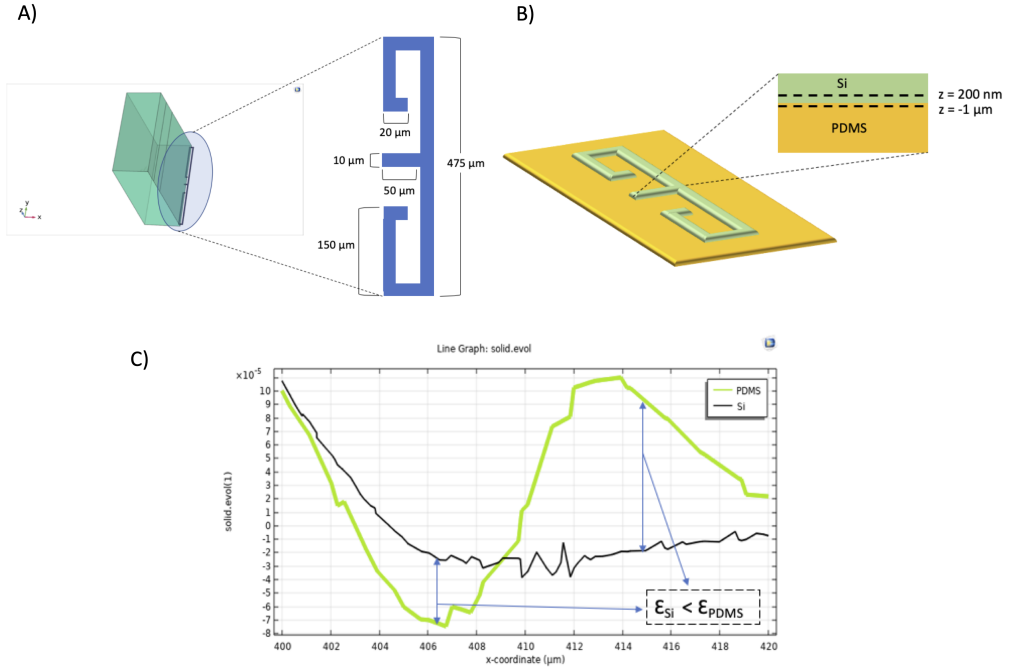
Figure 2.23: Piezoresistive sensor integration A) Geometrical properties of the sensor B) Cut-lines through sensor and PDMS domains C) Resulting strain in Si and PDMS along cutlines.

The effective gauge factor is given by Eq. 2.17 where ϵ_{Si} and ϵ_{PDMS} represent the strains in silicon and PDMS respectively and considering the GF of Si as the value calculated in Eq. 2.16 i.e 95. The solution is in agreement with literature [58].

$$GF_{eff} = 95 \frac{\epsilon_{Si}}{\epsilon_{PDMS}} = 40.7 \tag{2.17}$$
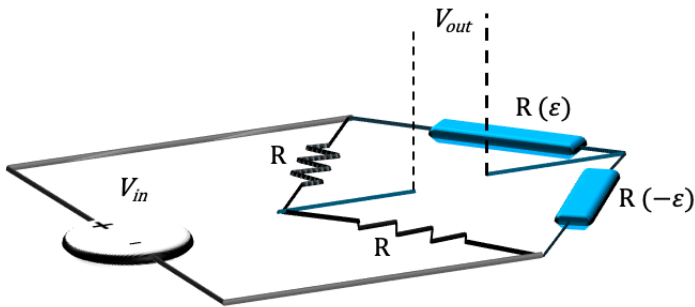

Figure 2.24: Circuit configuration for p-Silicon piezoresistive sensing.

Similar to piezoelectric devices, piezoresistive devices rely on the strain generated within the sensor domain. While Si exhibits a high gauge factor, its high stiffness (> 100 GPa) renders it unsuitable for flexible applications. Inspiration can, however, be drawn from

Silicon-on-Insulator technology for fabrication of nano-ribbons and thin film semiconductor sensors [58][59]. In order to develop a sensing modality which does not depend on the strain generated within the sensor, capacitive sensors have been explored in section 2.5. These sensors rely on the relative displacement between the plates, as opposed to the inherent deformation within the plates, leading to a change in the electrical output of the transducer.

2.5. CAPACITIVE SENSORS

The sensing modalities discussed in the previous sections exhibit a change in their output only via deformations occurring within the boundaries of the sensor. In order to circumvent challenges associated with these techniques, capacitive sensors are viable alternative sensing platforms since the change in capacitance does not depend on the strain transfer efficiency from the platform to the sensor. The change in the mechanical input is converted to a change in the electrical output via relative displacement of the capacitor plates as well as dielectric deformations due to pillar bending. Both these phenomena contribute to the electric field warping and can be fabricated using standard cleanroom fabrication technology without harming the soft polymer platform. The two capacitive test sensors explored are interdigitated capacitive electrodes and spiral electrodes. Since we would like to have minimal interference with the surrounding heart tissue, co-planar capacitors have been analysed as opposed to conventional parallel plate capacitors. The electrical field lines which play a role in detecting the deformation of the material under test (MUT) are the co-planar fields emanating from one plate of the capacitor and terminating on the other as shown in Fig. 2.25 [61].
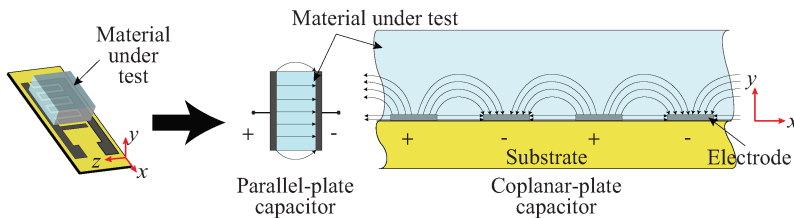

Figure 2.25: Structure of a co-planar capacitor whereing co-planar fields emanate from one plate and land on the next plate through the dielctric [61].

2.5.1. SIMULATION ENVIRONMENT

Since the primary quantity of interest is the electric field in the system, the simulation environment has been modified to include a spherical air domain around the sensor (in grey) integrated with the EHT platform as shown in Fig. 2.26. Additionally, a moving mesh has been assigned to this air domain to account for the changes in the electrical field due to the application of a boundary load to the pillar. The distortion in the spatial electric field is then coupled to the change in the terminal capacitance of the system. The plates are modelled as pure conductors and charge storage entities responsible for the generation of electric field while the outer boundaries of the air domain are assigned zero charge boundary conditions and act as perfect insulators. Aluminium has been chosen for analysis due to its lower stiffness as compared to other metals as well as its

biocompatibilty. The fully coupled solver has been replaced with a segregated solver to account for the high degrees of freedom introduced due to the moving mesh. Due to the differences between the dielectric constant of the EHT platform and the surrounding medium, the electric field lines and their gradients are not uniform. This leads to a further increase in the sensitivity. The cross-sectional view of the system is shown in Fig. 2.27 and the stream-line of the spatial electric field in Fig. 2.28. It can be seen that field lines are closer together in the MUT and exhibit a varying degree of curvature depending on their position within the medium as well as the dielectric constant of the medium. The complete simulation flow is shown in Fig. 2.30.
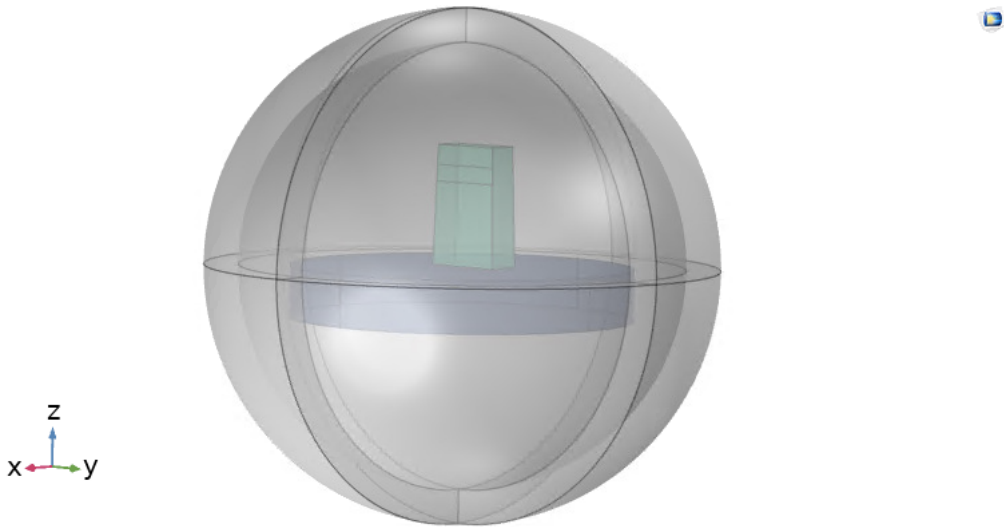

Figure 2.26: Spherical air domain around EHT platform ($2\phi = 3$ mm).
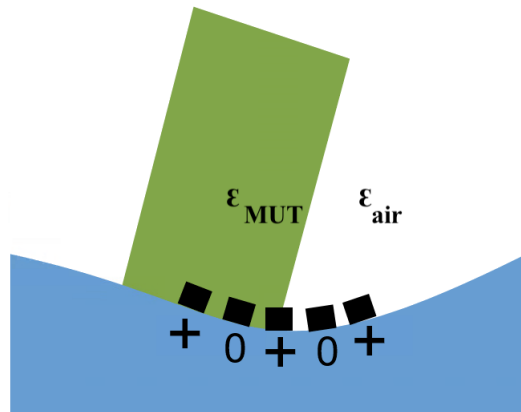

Figure 2.27: Surface cross section of EHT with capacitive sensor.

The electrical field lines due to the plate travel from a higher potential to a lower po-

tential, in this scenario, from the positively charged plates (+) to the grounded plates (0). The relative dielectric constant of PDMS (ϵ_{MUT}) has been considered isotropic and equal to 2.75 while that of air (ϵ_{air}) as 1. The cross-section surface is utilised to plot the electric field lines as shown in Fig. 2.27 in the original geometry frame.
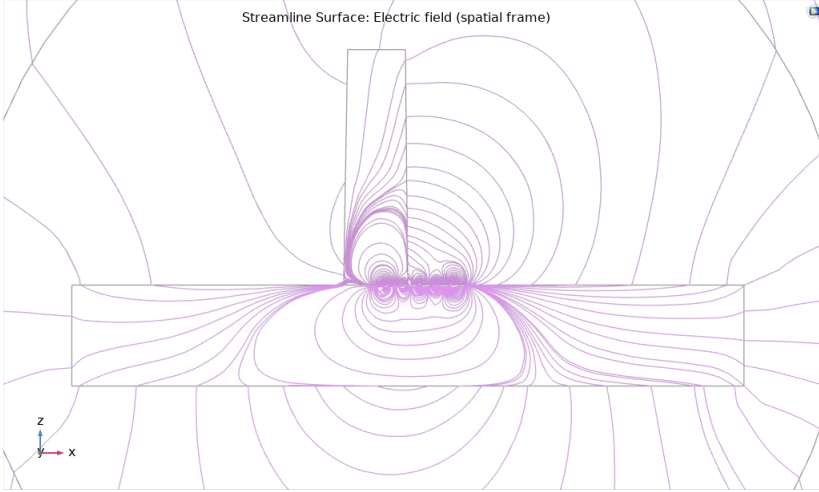

Figure 2.28: Surface spatial electric field due to integrated capacitive sensors [cross-sectional view].

The total capacitance of the co-planar structure is a superposition of all the co-planar field and parallel plate capacitances present in the model. As an example, a capacitor consisting of three plates constitutes of four individual capacitors arising due to the generated co-planar field as shown in Fig. 2.29. They are denoted by C_{1a}, C_{2a}, C_{1b} and C_{2b}. The former two capacitors consist of air as the dielectric while the latter capacitors consist of PDMS as the dielectric. The parallel plate capacitance can be considered negligible for large surface area thin film capacitors.
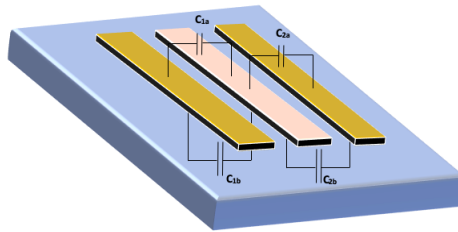

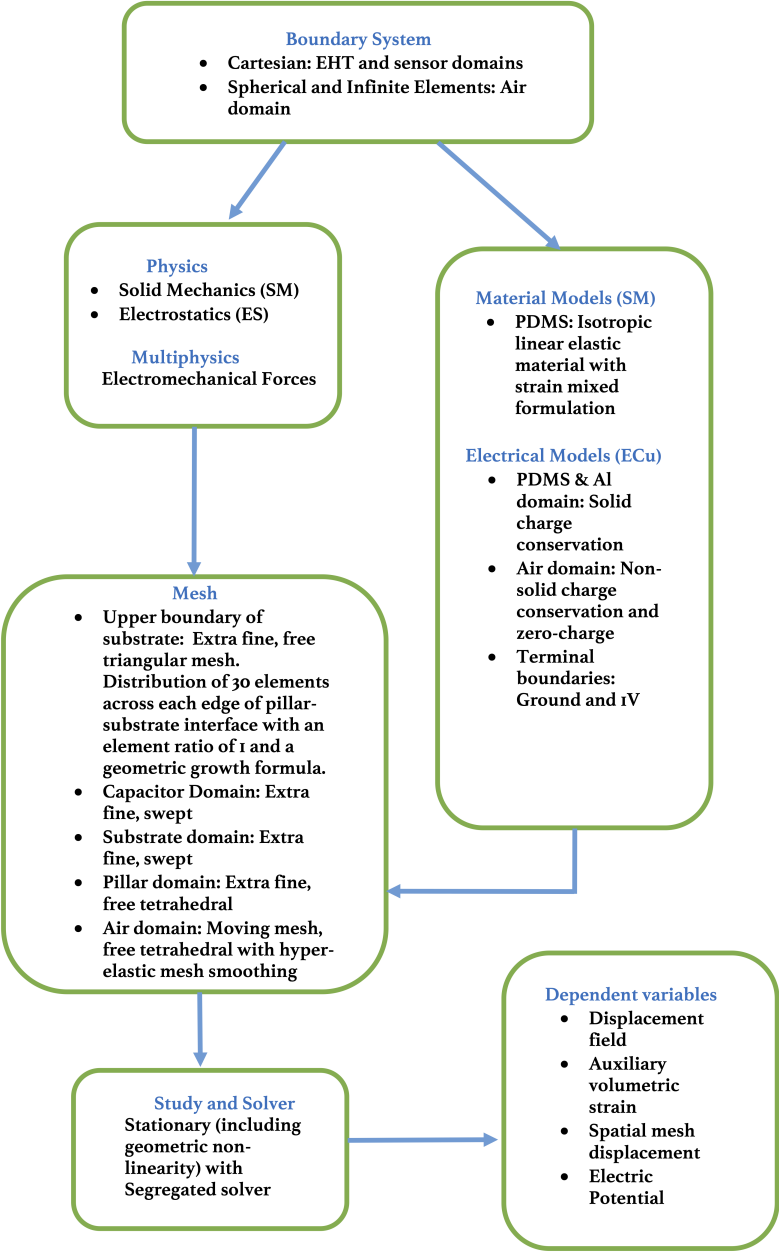Figure 2.29: Co-planar field capacitors in a three-plate capacitor.

Boundary System
- Cartesian: EHT and sensor domains
- Spherical and Infinite Elements: Air domain

Physics
- Solid Mechanics (SM)
- Electrostatics (ES)

Multiphysics
Electromechanical Forces

Material Models (SM)
- PDMS: Isotropic linear elastic material with strain mixed formulation

Electrical Models (ECu)
- PDMS & Al domain: Solid charge conservation
- Air domain: Non-solid charge conservation and zero-charge
- Terminal boundaries: Ground and 1V

Mesh
- Upper boundary of substrate: Extra fine, free triangular mesh. Distribution of 30 elements across each edge of pillar-substrate interface with an element ratio of 1 and a geometric growth formula.
- Capacitor Domain: Extra fine, swept
- Substrate domain: Extra fine, swept
- Pillar domain: Extra fine, free tetrahedral
- Air domain: Moving mesh, free tetrahedral with hyper-elastic mesh smoothing

Dependent variables
- Displacement field
- Auxiliary volumetric strain
- Spatial mesh displacement
- Electric Potential

Study and Solver
Stationary (including geometric non-linearity) with Segregated solver

Figure 2.30: Simulation flow for capacitive sensor.

A capacitive divider can be utilised to measure the change in capacitance (C_s) as shown in Fig. 2.31. The reference capacitor (C_{ref}) can be fabricated on the PDMS substrate on areas where the dependent variables have a zero gradient.
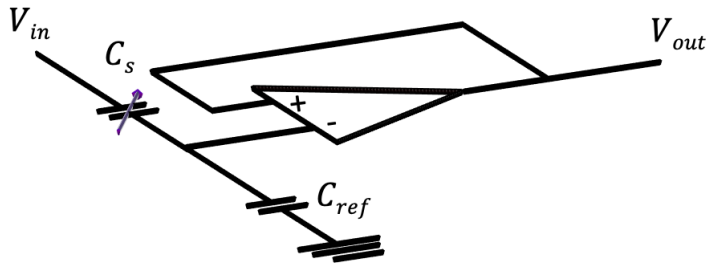
Figure 2.31: Circuit configuration for co-planar capacitive sensing.

2.5.2. Interdigitated Electrode Sensor

The design for the test strain sensor is based on the comb-drive model commonly used in accelerometers and gyroscopes. The strain in the substrate translates to a relative change in the distance between the "fingers" of the electrodes [62]. The dependent variable of interest in this test simulation is the strain in the PDMS arising due to bending of pillars. The interdigitated electrode design is shown in Fig. 2.32. The gap (g) and the electrode width (w) have been assigned a value of 5 μm keeping in mind the limits of micro-fabrication [63]. The sensitivity of this structure is -0.566 pF/N when considering S1 and 0.564 pF/N when considering S2. As the plates come closer due to compressive strain, the gap reduces leading to an increase in capacitance.
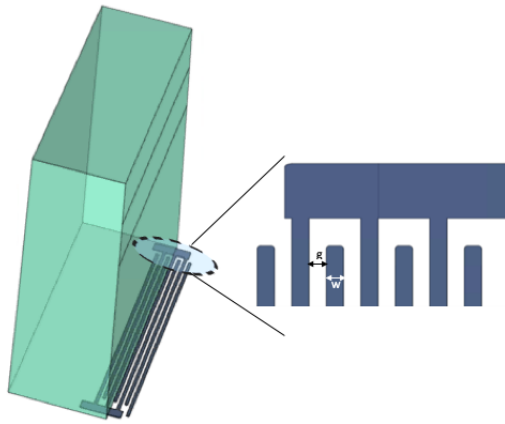

Figure 2.32: Interdigitated strain sensor position at the pillar -substrate interface

2.5.3. Spiral Co-planar Sensor

In order to utilise the full extent of the gradients in the dependent variables, spiral capacitors have been chosen for analysis. The spiral design leads to a higher base capacitance in the device as well as maximal exposure to the pressure within the system. By placing

the center of the sensor at the position of peak pressure, a relative displacement occurs between the spirals leading to a change in capacitance. The spiral geometry can be either circular or rectangular. Since our aim is to maximise the sensitivity of the device, rectangular spirals are chosen on account of the high gradient of electric field which arises at the sharp corners of the turns in the device. The metallization ratio (MR) of the sensor is defined by Eq. 2.18.

$$MR = \frac{w}{w+g} \tag{2.18}$$

Where the width of the plates is denoted by w and the gap between the plates by g. The major and minor axes length are denoted by L_a and L_b respectively as shown in Fig. 2.33. Their values are chosen to be equal to the dimensions of the piezoelectric sensor discussed in section 2.3 in order to maintain uniformity. Table 2.5 highlights the sensitivities for spirals with different metallization ratios. The design of the sensors has been performed using the following constraints:

- Outer dimensions (L_a and L_b) have been kept constant where $L_a = 800 \ \mu m$ and $L_b = 100 \ \mu m$

- The sensors exhibit no crossover across the neutral axis along the breadth of the pillar.

- The center of sensor lies at the edges of the pillars, along the width.

Considering an initial value of MR = 0.5, as the metallization ratio increases, the sensitivity reduces. This can be linked to the drop in the surface area of the sensor which occurs due to the reduction in the number of turns in the spiral as w increases while keeping the gap at a constant value of 5 μm. Metallization ratios below 0.5 have not been considered since they lead to gaps higher than plate width which in-turn reduces the base capacitance. The sensor at position S2 has been considered for all analyses, of which the displacement and strain are negative.
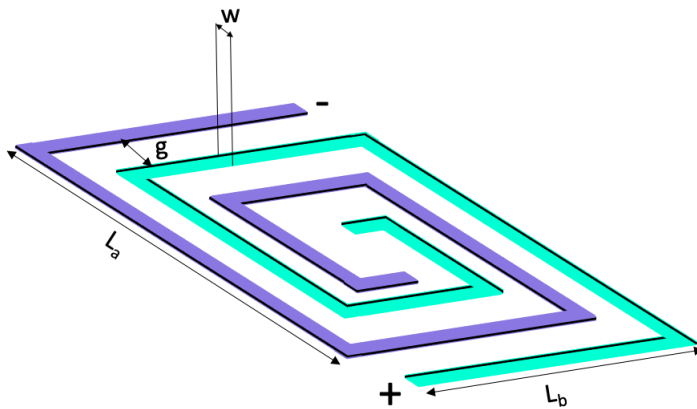

Figure 2.33: Geometrical properties of spiral capacitive sensor.

Table 2.5: Magnitude of sensitivity of rectangular spiral sensors with varying metallization ratio.

	MR = 0.3	MR = 0.4	MR = 0.5	MR = 0.6	MR = 0.7	MR = 0.8
Sensitivity	0.222 pF/N	2.256 pF/N	4.866 pF/N	3.149 pF/N	2.508 pF/N	1.51 pF/N

When the center of the sensor lies on intersection of the neutral axes of the pillar the sensitivity is equal to 0 pF/N since this is analogous to placing two capacitors in parallel which exhibit an equal and opposite change due to applied force. This further validates the antiymmetric nature of the dependent variables across the neutral axes. Due to the comparatively better sensitivity of spiral capacitor sensors, they have been chosen as the sensor of choice and explored more deeply in section 2.6.

2.6. FINALISED SENSOR SIMULATIONS

In this section, a more in-depth analysis of the properties of co-planar spiral capacitors is performed. The outer dimensions of the sensor have been kept constant while the metallization ratio has been changed by varying the gap and width of the sensor. The position of the sensor within the substrate has been varied as well. Once the sensor is shifted within the substrate, a swept mesh cannot be applied due to non-uniformity in the volume of the substrate and instead a finer tetrahedral mesh is used. Due to the thin-film property of the sensor, the number of degrees of freedom of the complete simulation exceeds 2 million leading to a long computation time and difficulties with convergence. In order to curb this, the mechanical modeling of the sensor is defined via a Shell interface wherein the electrodes are defined as boundaries rather than domains with infinitesimal thickness. This model is then fully coupled to the EHT platform and the mesh is refined to generate a constant base capacitance on every iteration. The size of the sensors has been increased as compared to the test capacitive simulations so as to occupy all the displaced area. Each pillar is integrated with two spiral sensors. This is shown in Fig. 2.34. The outer dimensions are now:

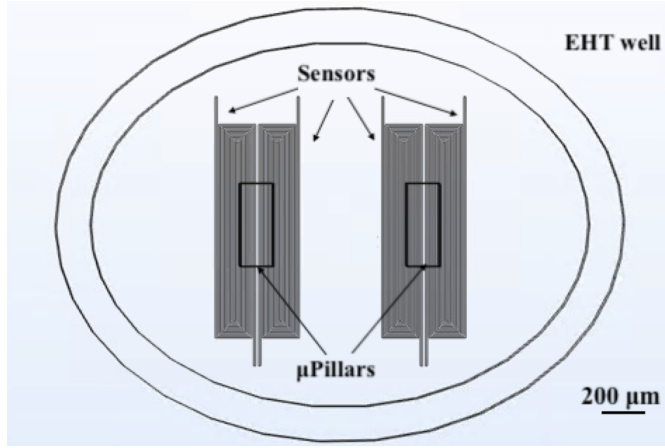- $L_a = 1200 \ \mu m$

- $L_b = 200 \ \mu m$

Figure 2.34: Sensors integrated with the EHT platform. Each chip consists of four capacitors, two micro-pillars and one well.

The base capacitance per unit length is first derived analytically using co-planar waveguide (CPW) theory [64]. This is followed by electro-mechanical COMSOL simulations to analyse the response of the sensor to the applied contractile force.

2.6.1. Analytical Derivation of Base Capacitance using Co-planar Waveguide (CPW) Theory

In this section an analytical derivation based on co-planar wave-guide theory has been done and this is used as a benchmark for further finite-element simulations. The classical model of the parallel-plate capacitor is mapped to a co-planar system while preserving geometry by utilising elliptical integrals [64]. The dimensions of the cross-section of a three-plate capacitive system shown in Fig. 2.35 along with polarity of the electrodes. The plates are encapsulated in a medium of relative permittivity $\epsilon_2 (= 2.75, PDMS)$ and this medium is in-turn placed in an infinitely large system with permittivity $\epsilon_1 (= 1, air)$. Since the capacitance is derived per unit length, the average path length of the spiral is used as the multiplying factor to calculate the total capacitance. The average path length, l_{av}, is denoted by the dotted lines shown in Fig. 2.36. The base capacitance is derived as the capacitance when there is no micropillar displacement (boundary load = 0).

Table 2.6: Geometrical properties of integrated spiral sensors.

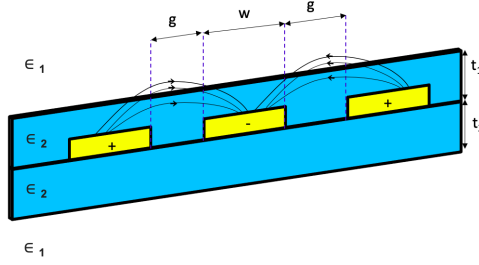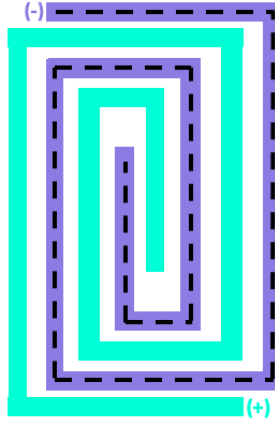|	Sensor A	Sensor B	Sensor C	Sensor D	Unit
Gap (g)	5	10	5	10	μm
Electrode width (w)	20	10	5	40	μm
l_{av}	6310	7554	13521	3995	μm

Figure 2.35: Cross section of embedded co-planar capacitor. The depth of the sensor is indicated by t_1

Figure 2.36: Average path length of spiral capacitor plate.

Table 2.6 highlights the properties of the sensors. The total polymer thickness $t_1 + t_2$, where t_1 is the depth of the sensor, has a maximum and constant value of 300 μm and is limited by micro-fabrication restrictions. The thickness of the electrodes is lower than 1 μm keeping in mind fabrication strategies. The sensor with the least electrode width has the highest average length due to a higher number of turns in the spiral. Sensors A and D constitute the capacitors with MR = 0.5 and sensors B and C constitute the capacitors with MR = 0.8.

The permittivity of the system is given by Eq. 2.19 [64].

$$\epsilon_{eff} = 1 + (\epsilon_2 - \epsilon_1)(a_1 + a_2) \tag{2.19}$$

wherein a_1 and a_2 are the proportionality constants derived in the following equations.

$$m_1 = 0.5w \tag{2.20a}$$

$$m_2 = m_1 + g \tag{2.20b}$$

$$m_3 = m_2 + w \tag{2.20c}$$

$$m_4 = m_2^2 - m_1^2 \tag{2.20d}$$

$$m_5 = m_3^2 - m_1^2 \tag{2.20e}$$

$$k_0 = \frac{m_3}{m_2} \sqrt{\frac{m_4}{m_5}} \tag{2.21a}$$

$$k_0' = \sqrt{1 - k_0^2} \tag{2.21b}$$

$$C_0 = \epsilon_0 \frac{K(k_0)}{K(k_0')} \tag{2.21c}$$

Wherein $K(k_i)$ denotes the elliptical integral of the first kind and ϵ_0 is the permittivity of free space ($8.85 \cdot 10^{-12}$ F/m).

$$k_i = \frac{\sinh\left(\frac{\pi m_3}{2t_i}\right)}{\sinh\left(\frac{\pi m_2}{2t_i}\right)} \sqrt{\frac{\sinh^2\left(\frac{\pi m_2}{2t_i}\right) - \sinh^2\left(\frac{\pi m_1}{2t_i}\right)}{\sinh^2\left(\frac{\pi m_3}{2t_i}\right) - \sinh^2\left(\frac{\pi m_1}{2t_i}\right)}} \qquad i = 1,2 \tag{2.22a}$$

$$k_i' = \sqrt{1 - k_i^2} \qquad i = 1,2 \tag{2.22b}$$

$$a_i = \frac{K(k_o) K\left(k_i'\right)}{2K\left(k_o'\right) K(k_i)} \qquad i = 1,2 \tag{2.22c}$$

Equations 2.19a-2.22c can be utilised to calculate the capacitance per unit length of a co-planar capacitor embedded in stacked media. The final co-planar capacitance (C_{cop}) is given by:

$$C_{cop} = \epsilon_{eff} C_0 l_{av} \tag{2.23}$$

Due to the finite radius of curvature of the electric field lines shown in Fig. 2.35, the capacitance derived in Eq. 2.23 becomes constant only after a certain depth into the PDMS. An example has been shown in Fig. 2.37 when sensor A is embedded in the polymer. At a depth (t_1) less than 50 μm, some electric field lines escape into air and as the sensor is pushed further into the substrate, the concentration of field lines in the PDMS increases which leads to a capacitance independent of depth. The capacitance reduces at the second threshold depth ($t_1 = 250 \ \mu m$). The total capacitance as a function of gap and width keeping the average length constant is given in Appendix C.
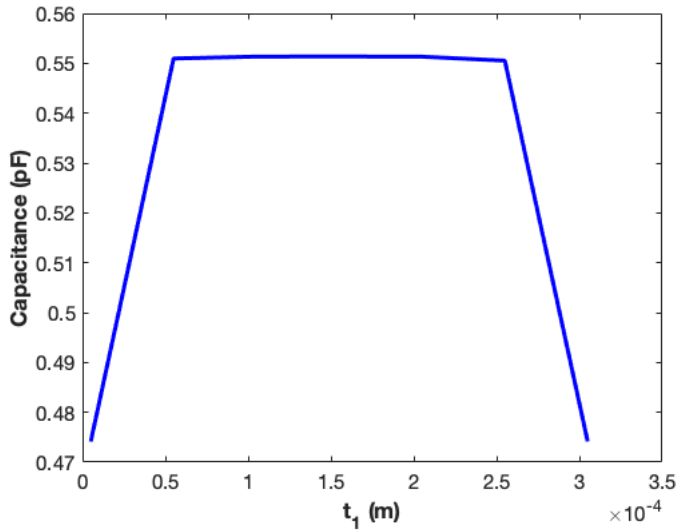
Figure 2.37: Change in capacitance of embedded co-planar capacitance with depth of sensor.

The first threshold depth of 50 μm is applicable for all four sensors under consideration. Hence, the base capacitance is derived when $t_1 = t_2 = 150 \ \mu m$. This is compared with the simulations performed in COMSOL and shown in Table 2.7. The aim of this analysis is to check and validate if the results provided by COMSOL lie within the same order of magnitude as CPW theory. If not, the meshing characteristics must be further analysed along with the derivation of the analytical base capacitance. The sensitivity (S) is calculated using Eq. 2.24.

$$S = \frac{C_2 - C_1}{F_2 - F_1} \tag{2.24}$$

- C_1 = base capacitance when $F_1 = 0$. This must be calculated on every iteration in COMSOL due to any minor changes in sensor positioning and meshing sequence(s).

- C_2 = new capacitance when $F_2 = 10 \ \mu N$

The change in capacitance exhibits in linear relationship with the applied force which can be explained by the linear trend associated with the peak displacement in the substrate as a function of force.

Table 2.7: Comparison of analytical and simulated base capacitance of the integrated sensors.

	Sensor A	Sensor B	Sensor C	Sensor D	Unit
Base capacitance (CPW theory)	0.55092	0.41017	0.73418	0.34865	pF
Base capacitance (COMSOL)	0.59279	0.43321	0.77640	0.36013	pF
| Sensitivity | (COMSOL), $t_1 = 5 \ \mu m$	1.51	3.1	4.864	0.86	pF/N

It must be noted that co-planar wave-guide theory is sufficient to gauge the order of the simulated output and may not be applicable as a benchmark to find the precise base

capacitance of the spiral sensors. The validity of the equation is dependent on number of plates forming the spiral. One wave-guide constitutes of three plates as shown in Fig. 2.29, a geometrical necessity which might not be satisfied by the designed sensors as can be seen in Fig. 2.38. Additionally, the COMSOL derived capacitance is highly dependent on the meshing of the air domain as well as the substrate as shown in Appendix D.
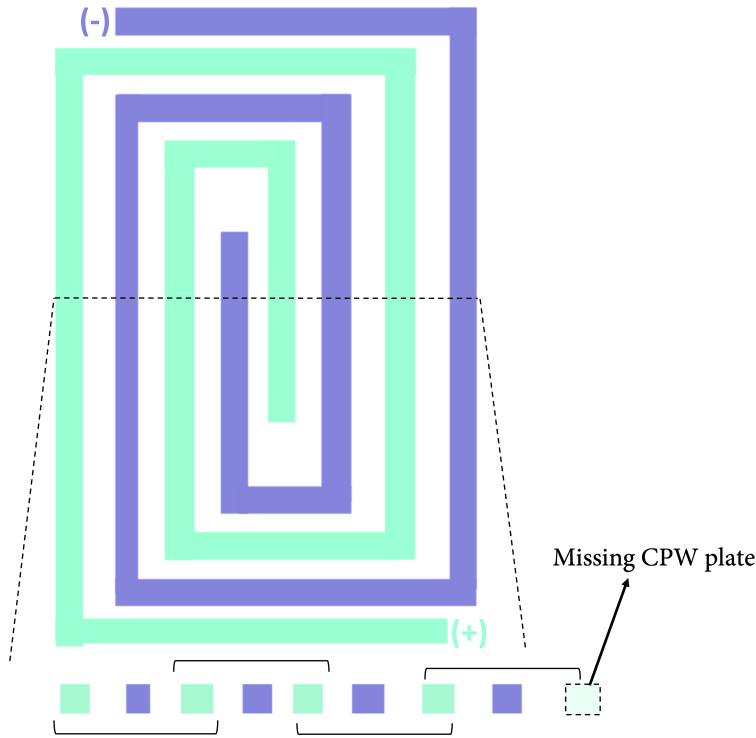

Figure 2.38: Cross-section of spiral sensor. Each wave-guide is respresented in groups of 3 plates.

2.7. INTEGRATED SENSOR ANALYSIS

The sensors exhibit an exponential drop in sensitivity as their depth within the substrate increases on account of the behaviour of the mechanical dependent variables discussed in section 2.2 as seen in Fig. 2.40. In order to test the sensitivity as a function of EHT substrate thickness, sensor D is chosen for analysis due to the generation of lesser number of nodes on meshing. As the substrate thickness reduces, the sensitivity drops as well and this phenomena can be explained by the mechanical behaviour of the substrate as a response to the plane strain problem which occurs in materials whose thickness is much lower than their dimension in the other plane[65]. The assumption of half-space elasticity is not valid anymore and the thin substrate begins to show a more rigid behaviour due to the reduced volume of polymer available. This result is in-line with literature analysing limits in warping of substrates due to bending of pillars which reduces as the thickness of the substrate reduces [48]. On Comparing Fig. 2.10 and Fig. 2.39 we observe that the peak displacement has dropped by $1/4^{th}$ of its initial value with both compres-
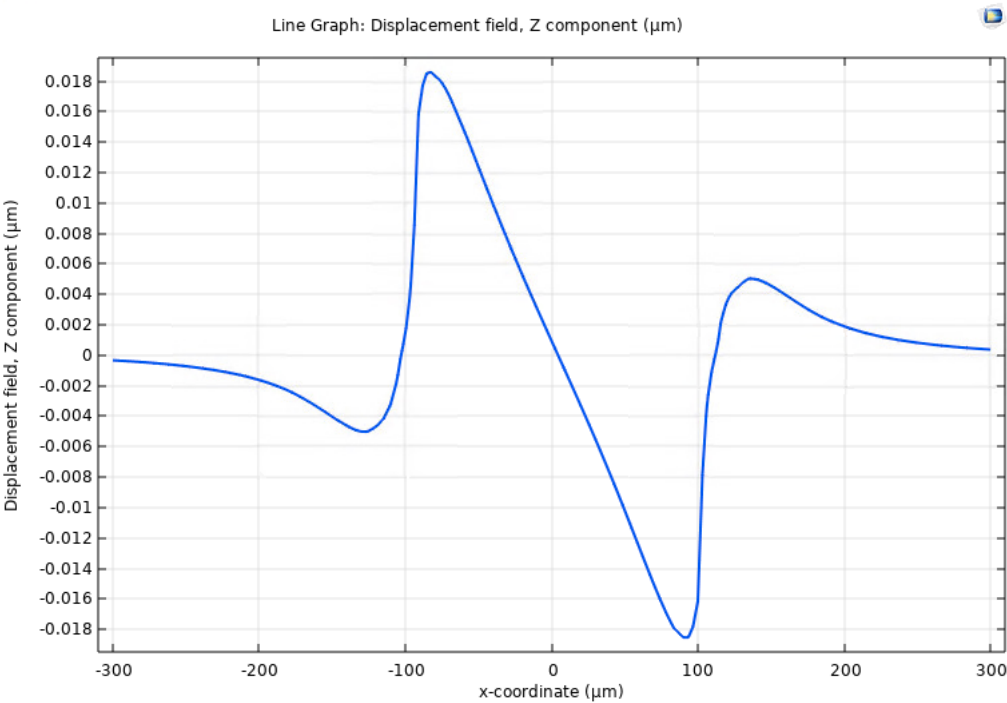
Figure 2.39: Vertical displacement field of substrate of the EHT platform with substrate thickness of 50 μm.

sive and tensile responses on the same side of the neutral axis of the pillar. This leads to a drop in the effective displacement arising in the sensor which leads to a drop in sensitivity. This drop occurs only below a critical thickness (t_c) of 200 μm. There is no change in sensitivity when $t_1 + t_1 \geq 200$ μm. An additional advantage provided by increasing the width of the substrate is the increased availability of media with a higher dielectric constant.
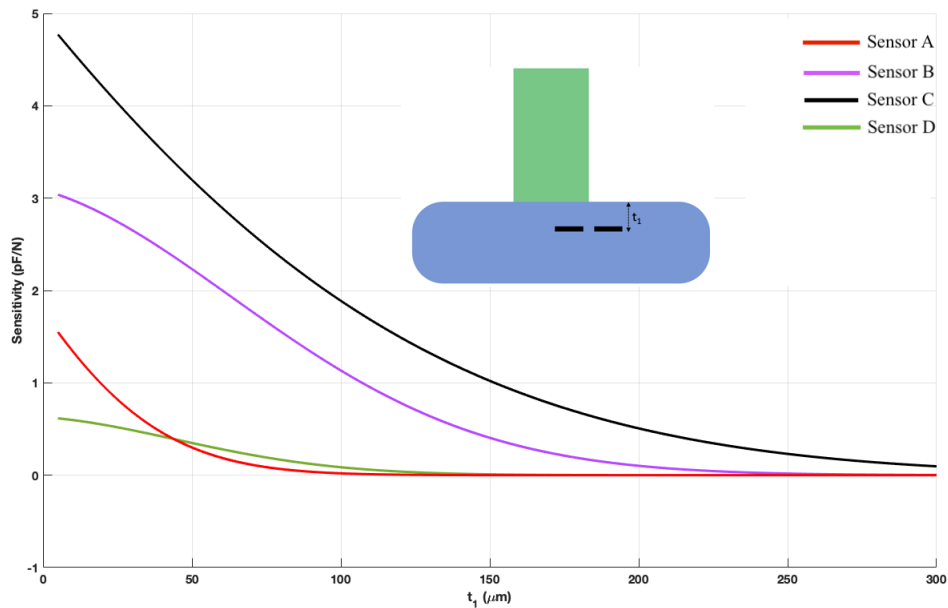
Figure 2.40: Sensitivity vs depth (t_1) of sensor within PDMS.

The sensor (D) is also modeled as a time varying capacitor using a time-dependent study in COMSOL as shown in Fig. 2.41. A sinusoidal boundary load analogous to a heart beat is defined on the pillar with a peak value of 10 μN and a frequency of 0.3 Hz is defined.
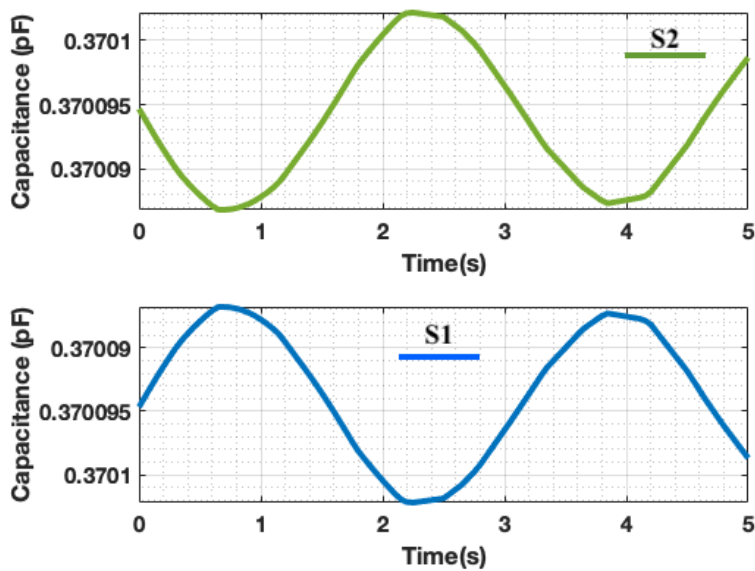

Figure 2.41: Capacitance of sensor D at positions S1 and S2 on application of sinusoidal boundary load.

2.8. Conclusion

A quantitative (Table 2.8) as well as a weighted qualitative comparison (Table 2.9) between the different sensitivities and potential integration of the tested sensing techniques shows the aptness of a spiral capacitive sensor as compared to other sensing modalities. The quantitative comparison has been performed by normalising the change in the electrical quantity with respect to its base value when there is no force applied on the pillar and is expressed as $\frac{\Delta M}{M}$ where M can represent the base resistance, voltage or capacitance.
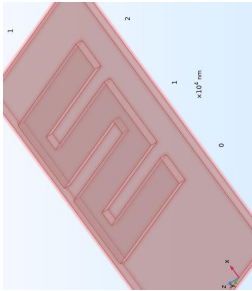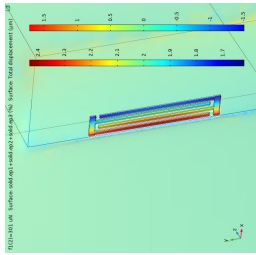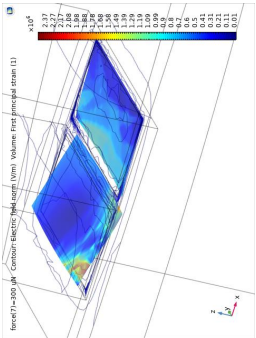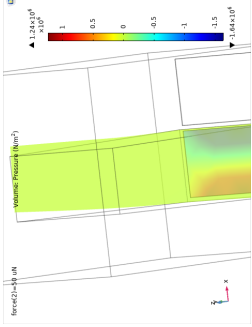
Table 2.8: Normalised sensitivity of integrated test sensors.

Transduction Technique	Sensitivity	Normalized Sensitivity [N⁻¹]
Piezoelectric	0.05 nV/N	0.05 x 10⁻⁹
Piezoresistive	6 Ω/N	0.022
Capacitive (Strain)	0.566 pF/N	1.712
Capacitive (Displacement)	1.51-4.864 pF/N	6.8 - 8.33

Capacitive sensors primarily based on detection of substrate displacement provide a significant advantage over strain sensors which rely on dimensional changes developed within their domains. The encapsulation of these sensors within the EHT platform serves the additional advantage of an improvement in baseline capacitive properties due to the presence of a medium with dielectric constant higher than air.

In order to efficiently gauge the performance of piezoelectric and piezoresistive sensors, their characterization is required along with experimental derivation of their coupling matrices. For less standardized materials such as PVDF, significant time and resources are required for its characterization. Since piezo materials provide no distinct advantage in their sensing abilities with regards to the EHT platform developed at EKL as indicated by their normalised sensitivities, capacitive sensors are used for further fabrication. The anisotropic nature of peizo electro-mechanical coupling coefficients combined with the presence of compressive and expansive principle strains on the same side of the pillar at the interface with the substrate further increases the complexity of piezoelectric and peizoresistive sensors in terms of design and orientation.

Table 3.3: Weighted comparison between different strain sensing techniques

Piezoresistive Strain Sensor	Capacitive Strain Sensor	Capacitive Tilt Sensor	Piezoelectric Pressure Sensor

Piezoresistive Strain Sensor

Advantages:

↑ Low fabrication complexity (+++)
↑ High dynamic range (++)
↑ Low sensor degradation over time (++)
↑ Good compatibility with clean room processing (++)
↑ Sensitive sensors can be fabricated using highly doped Silicon (+)
↑ Efficient integration with on-chip electronics (+)
↑ Good control over sensor properties (++)
↑ High sensitivity (++)

Disadvantages:

↑ Output varies with ambient temperature changes (-)
↑ **Low suitability for soft substrates on account of reduction in sensitivity due to strain transfer (SOI technology can be used but leads to a complex fabrication process) (- - -)**
↑ Output shows hysteresis (-)
↑ MEMS scale resistors consume high power (-)

Capacitive Strain Sensor

Advantages:

↑ Low fabrication complexity (+++)
↑ High dynamic range (+++)
↑ Low sensor degradation over time (+)
↑ Good compatibility with clean room processing (++)
↑ Change in output does not rely on electrode property change but on strain in the underlying substrate. Higher suitability for soft substrates (++)
↑ Output does not change with temperature (+)
↑ Good control over sensor properties (++)
↑ High sensitivity (++)
↑ Little to no hysteresis (+)

Disadvantages:

↑ Presence of parasitic and stray capacitance, especially at low strains (- -)
↑ Complex read-out electronics (- -)
↑ Non-linearity in output (-)
↑ Lower reliability in the sub-micrometre regime due possible shorting of capacitive plates on soft substrates (-)

Capacitive Tilt Sensor

Advantages:

↑ Low fabrication complexity (+++)
↑ High dynamic range (+++)
↑ Low sensor degradation over time (+)
↑ Good compatibility with clean room processing (++)
↑ Change in output does not rely on electrode property change but on relative displacement of the capacitor plates (+++)
↑ Output does not change with temperature (+)
↑ Good control over sensor properties (++)
↑ High sensitivity (++++)
↑ Little to no hysteresis (+)

Disadvantages:

↑ Presence of parasitic and stray capacitance, especially at low strains (- -)
↑ Complex read-out electronics (- -)
↑ Non-linearity in output (-)
↑ Lower reliability in the sub-micrometre regime due possible shorting of capacitive plates on soft substrates (-)

Piezoelectric Pressure Sensor

Advantages:

↑ Low fabrication complexity (+++)
↑ High dynamic range (+++)
↑ Low sensor degradation over time (+)
↑ High sensitivity (++++)

Disadvantages:

↑ Low resolution (- -)
↑ Can only be utilised in highly dynamic setups
↑ Complex read-out electronics (- -)
↑ Non-compatibility with standard clean room fabrication (the most widely used material is PZT which is lead based) (- -)
↑ Poor control over sensor properties (-)

3

MICROFABRICATION STRATEGY

In this chapter an overview of the fabrication steps for the patterning of spiral sensors on PDMS is outlined. As a step towards the first level assessment of sensor performance, they have been fabricated on flat Silicon (Si) wafers and utilised for further baseline electrical characterization. The process flow for the fabrication of sensors is presented followed by their integration with the EHT platform. *The developed sensors have been designed in such a manner so as to provide seamless integration with the previously developed EHT platform at ECTM, TU Delft and manufactured at EKL, TU Delft*. The choice of pure aluminium as sensor material aids in the development of integrated flexible sensors without the need of a stress buffering layer. Traditional forms of encapsulation involve additional deposition of polymeric layers such as parylene and polyamide of which the stiffness is an intermediate between the metallic layer and the PDMS, in order to curb cracking in films and improve adhesion [66]. In terms of mechanical actuation and electrical sensing this is a robust method. However, due to the low displacements present in the mechanical sensor ($< 5\mu m$), its encapsulation in a stress buffer/adhesive layer can lead to reduction in sensitivity due to increase in sensor depth as well as low displacements generated in the plane of the sensor. Hence, the spiral sensors are patterned and encapsulated between two layers of PDMS.

3.1. MASK DESIGN AND LAYOUT

The sensors have been classified based on their width (w) and gap (g) as discussed previously in Chapter 2. Each quadrant of the wafer has been assigned to one type of sensor as shown in Fig. 3.1 along with the mask design flow shown in Fig. 3.2. Since during further fabrication, positive photoresist will be utilised, dark digitization is used in the quartz photo-mask (Compugraphics International Ltd). Pure Aluminium has been chosen as the material for the capacitive plates due to its lower stiffness (40-70 GPa [67]) as compared to other metals (> 100 GPa [68]), excellent electrical conducting properties (resistivity = $3 \cdot 10^{-8} \Omega m$ [69]) and good bio-compatibility [70]. Three full wafer masks have been designed and their properties are as follows.

- Quartz mask comprising of sensors (S), contact pads (CP) and interconnects (I) for front-side patterning. Each die consists of two capacitors underneath each micropillar leading to a total of four capacitors. Each capacitor is separated by the neutral axis of the pillar denoted by the vertical dotted line as shown in Fig. 3.3.

- Foil mask comprising of only contact pads (CP) for front-side patterning as shown in Fig. 3.4a.

- Foil mask comprising of contact pads (CP) and wells (W) for back-side patterning as shown in Fig. 3.4b.
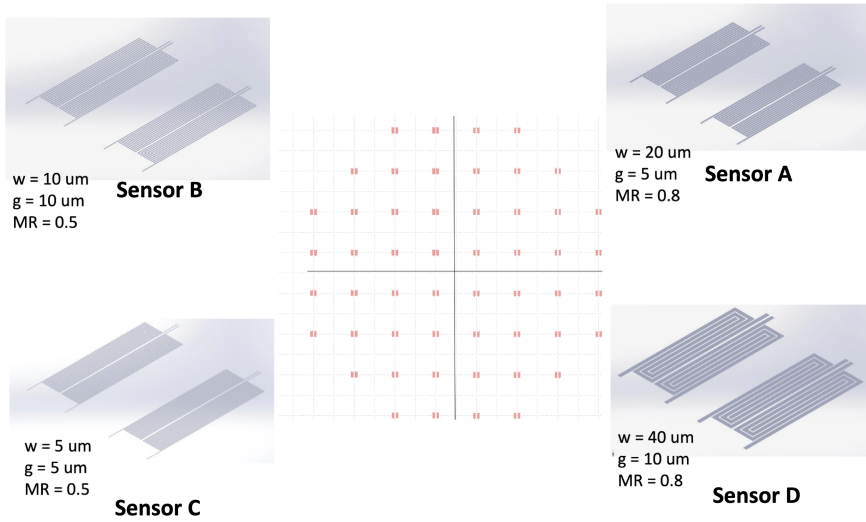

Figure 3.1: Wafer-level sensors characteristics ['g': gap, 'w': width, 'MR': Metallization Ratio].
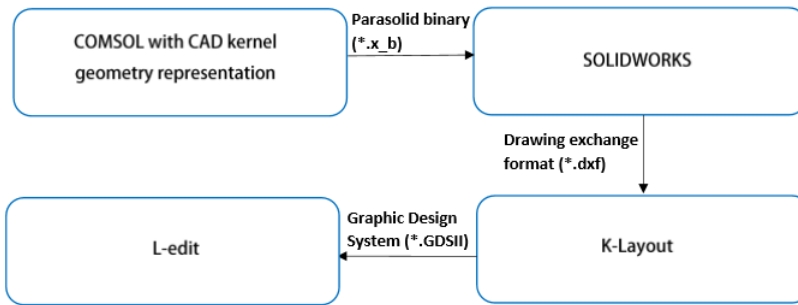

Figure 3.2: Quartz mask design flow.

Taking into account the integration of the sensors with the EHT platform, two additional masks have been designed as shown in Fig. 3.4a. The contact pad mask (CP) serves the

purpose of achieving thicker contact pads without changing the thickness of the sensors. A back side mask is composed of contact pad and well openings (CP+W) for wirebonding as shown in Fig. 3.4b. The actual layout of the masks is given in Appendix E.
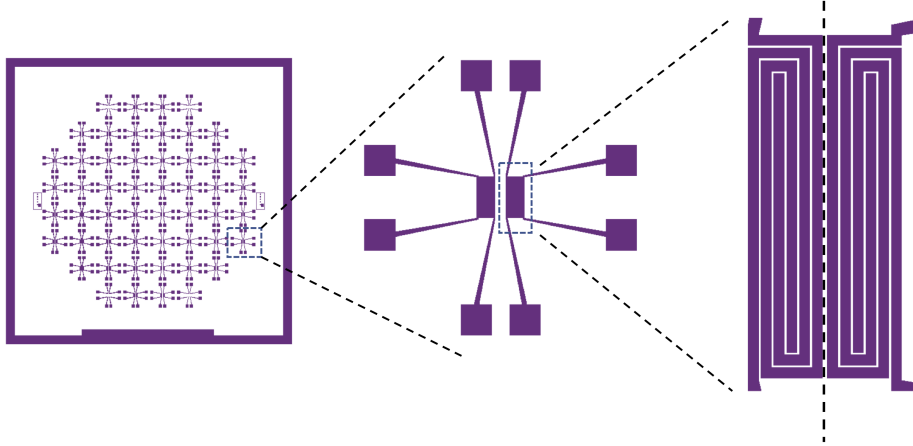
Figure 3.3: Quartz mask for contact pads, sensors and interconnects (CP+S+I).
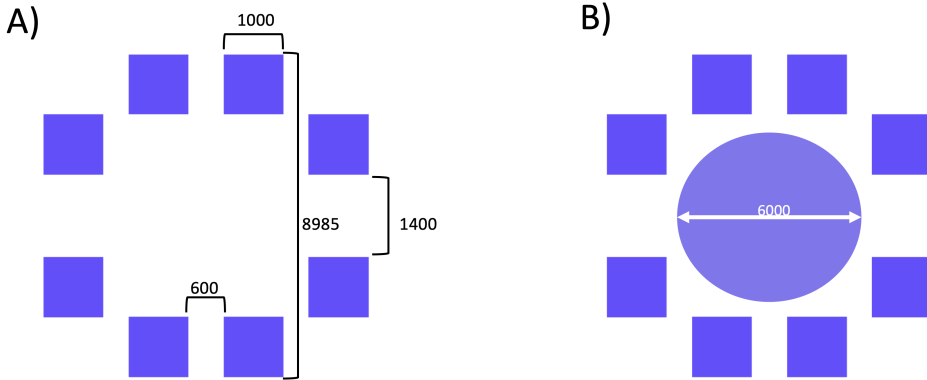
Figure 3.4: Foil mask for A) Contact pads (CP) B) Contact pads and wells (CP+W). All dimensions are in μm.

3.1.1. INTERCONNECT STRATEGY

The electrical connections between the sensors and the contact pads is done via tapered interconnects. Keeping the limits of micro-patterning on PDMS in mind, the interconnect width is always kept above 5 μm [63]. Tapered interconnects provide two distinct advantages:

- The gradually increasing width leads to a more piece-wise distribution of stress induced in the PDMS due to the difference in the elastic modulus of the soft sub-

strate and the metal (40-70 GPa, Al; 0.5-4 MPa, PDMS) coupled with the mismatch introduced due to the thermal coefficients of expansion (16-19 ppm/°C, Al; 300-350 ppm/°C, PDMS [71]).

- Tapered designs are often used in high-speed circuits due their contribution in reducing the RC delay in the device [72]. Since the sensors rely on capacitive sensing, a reduction in the interconnect delay provides a secondary advantage in improving the response of the device. Thin interconnects pose a high degree of parasitic resistance whereas wide interconnects pose a high degree of parasitic capacitance. Tapered interconnects provide an intermediate advantage wherein the interconnect width terminating at the contact pad is four times higher than the originating width at the sensor.

3.2. MICROFABRICATION

The patterning of the sensors on PDMS has been summarized in Fig. 3.5 and is performed on a single side polished (SSP) wafer with resistivity higher than 1 $k\Omega$ cm. Due to their comparatively small feature sizes and spiral nature, reactive ion etching (RIE) in plasma is preferred on account of its anisotropic nature as opposed to wet etching which constitutes of both lateral and vertical etching. Dry etching however, has lower etch selectivity and requires careful control over etching parameters such as gas flow, power and duration. Pure aluminium films can be etched using Chlorine (Cl_2) and Hydrogen Bromide (HBr) chemistry. The chlorine flow is always kept lower than HBr due to its very high reactivity with photoresist mask as well as Al as compared to HBr. The steps A1-C1 are utilised for developing wafers for further electrical characterization while steps A-G are presented for development of wafers with thick contact pads with metal-on-metal patterning.
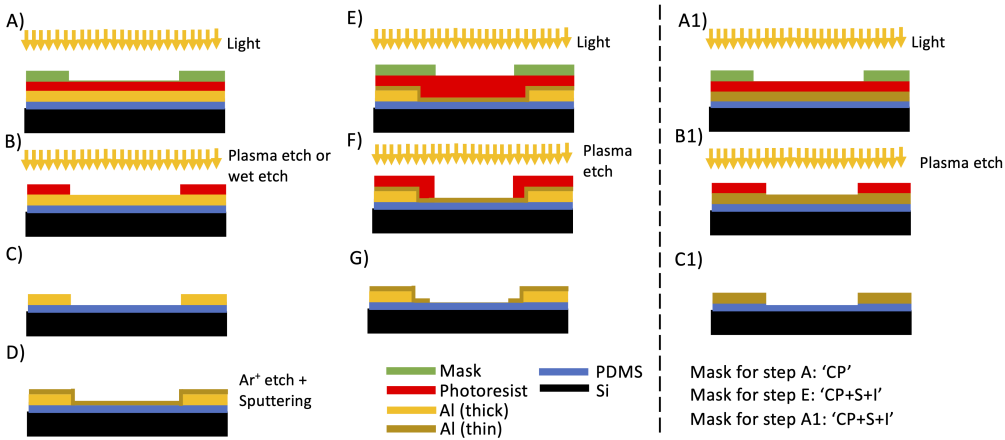

Figure 3.5: Microfabrication of spiral capacitive sensors on PDMS.

The integration of the spiral sensors with the EHT platform has been subdivided into three processes as follows. Due to the presence of both front-side as well as back-side

patterning, the integration is performed on a double side polished (DSP) wafer.

- Si ethcing for PDMS micro-moulding: Prior to micropillar fabrication, the front-side of the silicon wafer is etched by deep reactive ion etching in order generate a mould for the PDMS pillars as shown in Fig. 3.6.

- Patterning of the spiral sensors on the PDMS: Depending on the limitations of wire-bonding, either a single full wafer mask can be used (steps A1-C1 in Fig. 3.5) or metal-on-metal patterning can be attempted if contact pads more than 1 μm are desired (steps A-G in Fig. 3.5). The thickness t_1 should be as low as possible due to the drop in the sensitivity with depth as discussed in section 2.7. This is shown in Fig. 3.7 with the steps between 3.7n and 3.7o comprising of the fabrication steps presented in Fig. 3.7.

- The back-etching of the Si wafer leading to opening for the well and contact pads which is used for wire bonding as shown in Fig. 3.8. The finalised devices are diced into chips which have the capability for further PCB and/or well-plate integration. The total thickness of the PDMS substrate has been kept at $300\mu m$ so as to minimize any drop in sensor sensitivity due to the presence of a thin substrate.

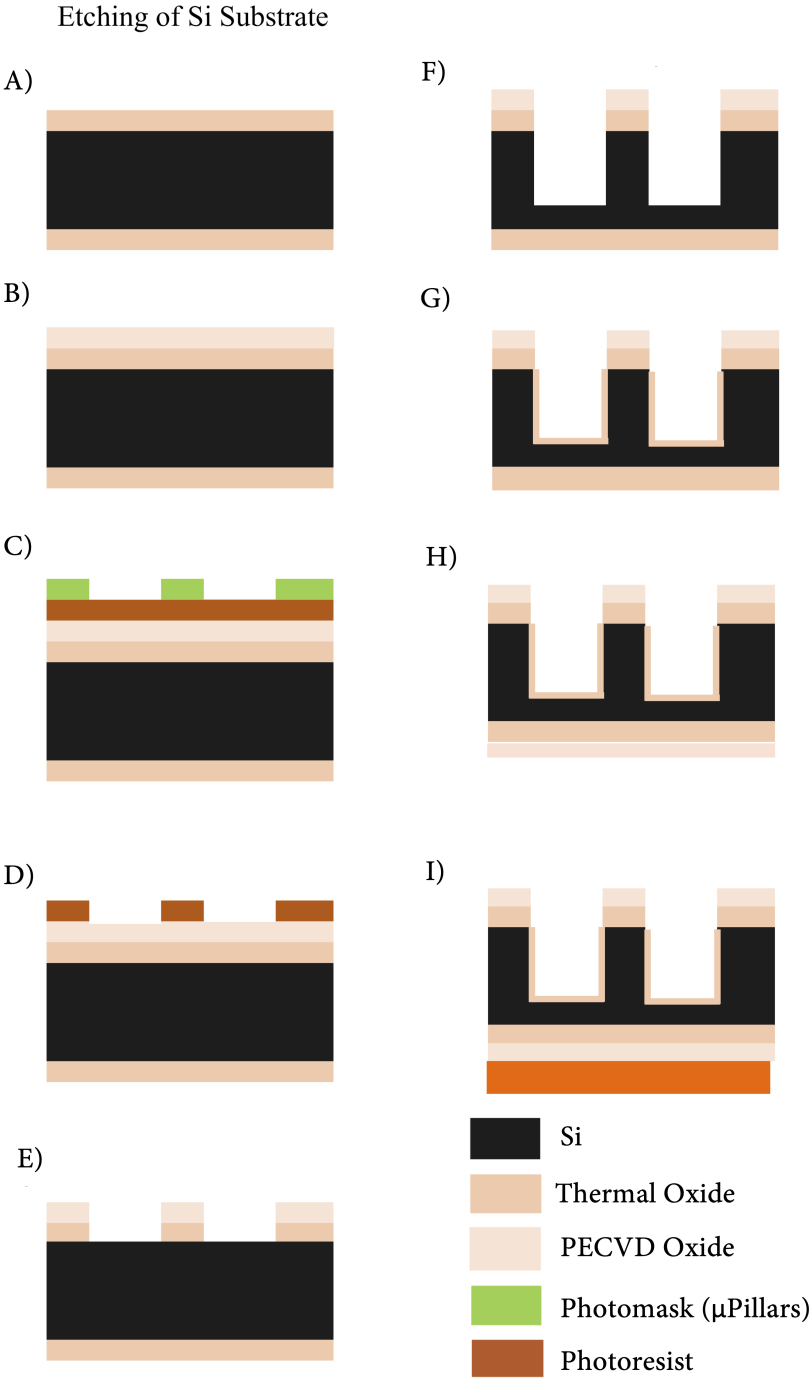Etching of Si Substrate

Figure 3.6: Molding of Si wafer by front-side etching.

Spiral Sensor and Pillar Integration

J)

K)

L)

M)

t_1

N)

.
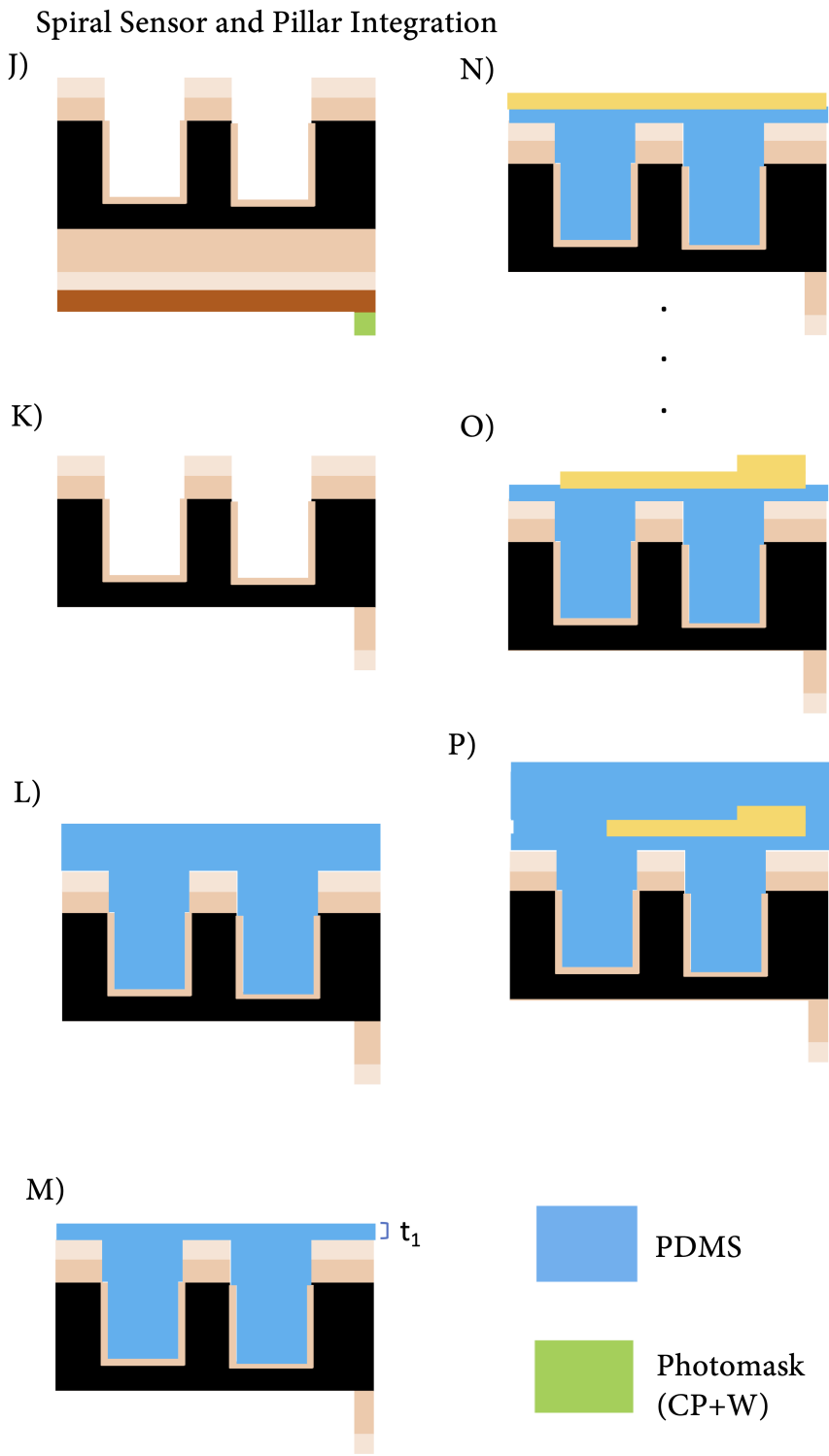.
.

O)

P)

PDMS

Photomask
(CP+W)

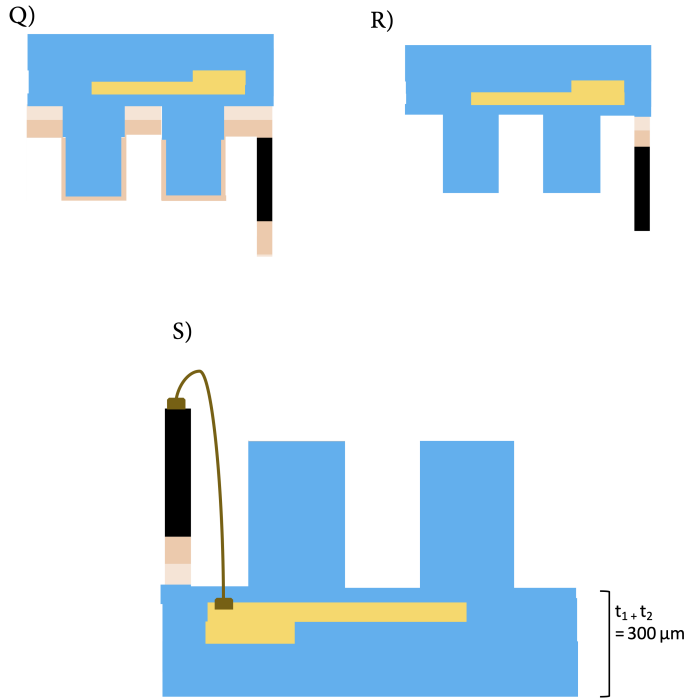Figure 3.7: Integration of spiral sensors with micropillars.

Figure 3.8: Back etching of Si for wire-bonding.

3.3. MICROFABRICATION OF SPIRAL SENSORS

3.3.1. PDMS DEPOSITION

PDMS SPIN-COATING AND CURING

In order to obtain a thin layer (~5 μm) of PDMS on the Silicon wafer, a spin speed of 8000 rpm for a period of 60 seconds has been chosen as the initial step. Thin PDMS films have been previously reported for spin speeds above 7000 μm [73][74]. The motivation behind beginning with a thin layer of PDMS is to replicate the sensor integration process presented in Fig. 3.7 wherein t_1 is minimized in step M. The PDMS base and curing agent (SYLGARD ^{TM} 184 Silicone Elastomer) have been mixed in a ratio of 10:1 w/w. In order to ensure efficient mixing and removal of trapped bubbles, the mixture is centrifuged for 30 seconds (THINKY ARE-250 Mixer). It is then poured on the wafer for spin-coating (Brewer Science Manual Spinner). The spin speed is initially ramped at 300 rpm for 5 seconds to assure uniform distribution of uncured PDMS over the substrate. The quality of the PDMS film is determined by a combination of the following factors:

- The mixing ratio between the base and curing agent.

- Spin speed of the substrate. The maximum available spin speed is limited by the composition of the PDMS. Uniform thin films ($< 5\mu m$) can be obtained on re-

ducing the concentration of the mixture by lowering the mixing ratio to 5:1 and spinning for longer durations [63].

• Surface topography of the substrate.

The PDMS layer obtained exhibits an edge-bead due to the antagonistic effects of centrifugal forces and surface tension in the viscous PDMS layer during rotation as shown in Fig. 3.9. This edge bead is manually removed with a cotton bud while rotating the wafer at 200 rpm. An additional advantage provided by this step is the prevention of PDMS over-flow to back of the wafer, particularly due to any expansions which might occur during high temperature curing.
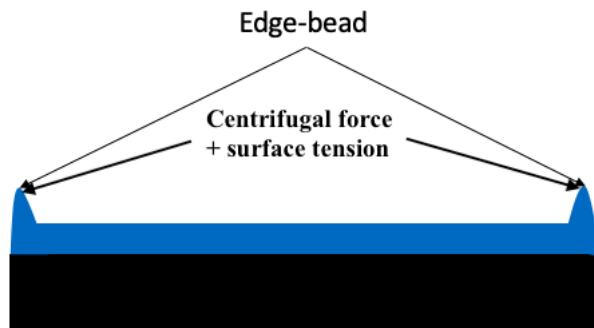

Figure 3.9: PDMS edge-bead due to centrifugal force generated during spin coating.

After spin coating, the wafer with PDMS is cured at 90°C for 60 minutes (Memmert Oven). If the curing is insufficient, the wafer should be cured for a longer duration as opposed to increasing the temperature of curing. This is to ensure thermal stability and efficient cross-linking in the polymer. It was found that at a spin speed of 8000 rpm and a spin duration of 60 seconds, the PDMS exhibited pinholes. The probable cause behind this behaviour is the viscous nature of PDMS and the threshold thickness which can be obtained at a given spin speed. If this threshold is crossed, high degrees of non-uniformity are developed as the forces acting on the mixture (centrifugal, viscous and surface tension) are no longer balanced and this effect is shown in Fig. 3.10 using laser microscopy (Keyence VK-X250). The same process has been performed on wafers which have been cleaned in nitric acid and rinsed in water in order to eliminate the presence of any probable particles that can lead to pinhole formation. Ideally, wafers which have been removed directly from the wafer box do not require any cleaning steps prior to fabrication.

In order to improve the uniformity of the PDMS, both the spin speed and duration were reduced. Care must be taken while performing this since the resulting thicker PDMS layer might require degassing for 30-60 minutes before further processing to remove trapped air bubbles. The new spinning conditions were set at 6000 rpm for a duration of 30 seconds corresponding to a thickness of ~10 μm [63].
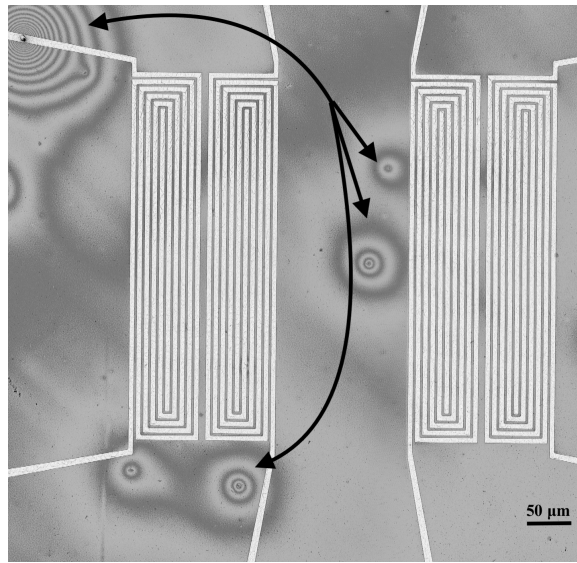
Figure 3.10: B/W laser microscope image of patterned structures on PDMS [black arrows].

SURFACE TREATMENT

The surface of cured PDMS is inherently hydrophobic [75]. This can reduce the adhesion of materials deposited on PDMS. The impact of an imperfect adhesion is more pronounced in processes which involve submerging of the wafer in liquids for example, during wet etching as well as cleaning and rinsing. Keeping this in mind, an oxygen plasma treatment of the PDMS surface is done in a low power plasma tool (ATTO Diener) for 1 minute at 200W. This leads to the formation of a thin silica layer on the surface of PDMS leading to exposed hydroxyl bonds as well as higher surface energy which contribute to improving adhesion between deposited metals and PDMS [75]. A secondary advantage provided by plasma treatment, is the generation of a thin buffer layer between metal and polymer which assists in reducing the mechanical mismatch between the two layers. Aluminium thin films and PDMS exhibit different Young's Moduli (40-70 GPa, Al; 0.5-4 MPa, PDMS) and coefficients of thermal expansion (16-19 ppm/°C, Al; 300-350 ppm/°C, PDMS) which induces stress at the interface between the metal and polymer layers leading to cracked metallic structures. The presence of a thin layer of intermediate stiffness has the potential of reducing the adverse effects generated due to this mismatch. Since surface plasma treatment is a reversible process, the time between treatment and subsequent layer deposition should be minimized. Plasma treatment has also been attempted for a longer duration of 5 minutes at a power of 200W in order to increase longevity of the silica layer. This however lead to cracking of the PDMS as seen in Fig. 3.11 due to the oxygen plasma which can cause generation of discontinuities in capacitor plates and the treatment duration was brought back down to 1 minute.
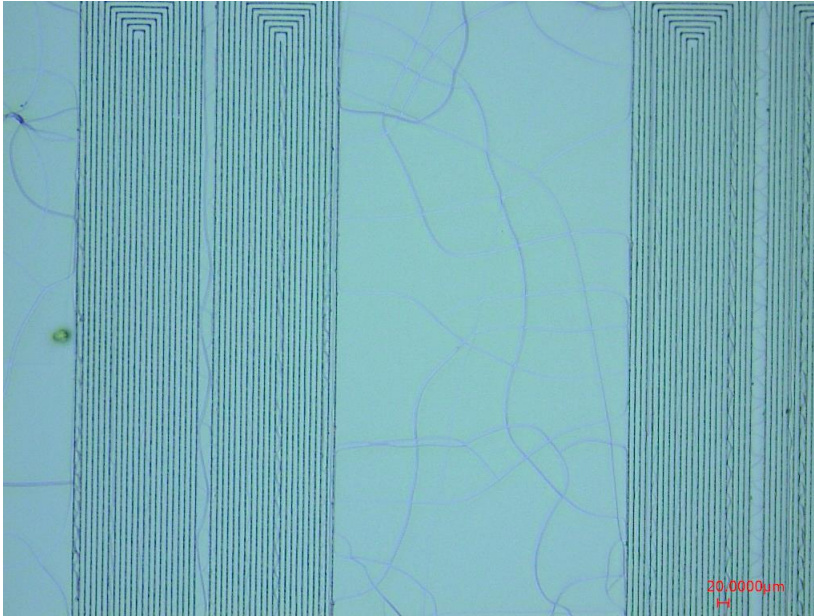
Figure 3.11: Cracking of PDMS due to oxygen plasma.

3.3.2. PHYSICAL VAPOUR DEPOSITION

Prior to exposure, aluminium thin films have been sputtered using physical vapour deposition (PVD) in the Sigma®fxP system (Orbotech SPTS Technologies). Since the substrate material is polymeric, a leak-up rate (LUR) test must be performed to ensure that any bubbles which escape from the polymer do not disrupt the partial pressure of the gas flow in the system and by extension the vacuum conditions which might lead to tool contamination. A rate lower than $2 \cdot 10^{-6}$ T.l/s is acceptable. If the rate is higher, the PDMS must be degassed further and/or a lower thickness must be used. Keeping in mind the stark differences between PDMS and metal coefficients of thermal expansion as well as thermal stability of PDMS, all sputtering steps are carried at 25°C and at a target power of 1kW. The Argon gas flow has been kept constant at 100 sccm. As a result of the bombardment of Argon ions with the Aluminium target, metal atoms are deposited on the wafer surface. Multiple durations have been used on different wafers keeping in mind the probing of sensors during electrical characterisation. The thickness has been measured using the Dektak profilometer system after subsequent etching leading to the formation of steps.

Due to the room temperature and the DC excitation used, the quality of the deposited films is inferior as compared to chemical vapour deposition and high temperature PVD. However, for low thickness ($<1 \ \mu m$) films on PDMS, this technique is sufficient to obtain films which can be utilised for further fabrication and characterization. At higher thicknesses, cracks begin to develop on the surface, which have the capability to propagate during further processing and external force applications. This is highlighted in Fig. 3.12a using laser microscopy. Post room temperature deposition, wrinkling can still

Table 3.1: Pure Aluminium sputtering at 25 °C and 1 kW.

Wafer	Duration (s)	Thickness (nm)
W_Al_1	87	150
W_Al_2	115.9	200
W_Al_3	144.8	250
W_Al_4	289.6	500
W_Al_5	405.5	700
W_Al_6	868.8	1500

3

be observed on the PDMS surface as shown in Fig. 3.12b using brightfield microscopy (Axitron Microscope, Carl Zeiss). The stress induced in the deposited film can be expressed quantitatively by Eq. 3.1 [71]. This leads to wrinkling in the film as well as PDMS to account for the produced mismatch.

$$F_c = 0.083 \cdot E_f \, t_f^3 \left[\frac{4\pi^2}{\left(1 - \nu_f^2\right) \lambda_{wr}^2} + \frac{E_{PDMS}}{4\pi \left(1 - \nu_f^2\right) \cdot 0.083 \cdot t_f^3 E_f} \lambda_{wr} \right] \tag{3.1}$$

The quantities denoted by Eq 3.1 are as follows:

- E_f: Young's Modulus of thin film.

- E_{PDMS}: Young's Modulus of PDMS substrate.

- t_f: Thickness of sputtered thin film.

- ν_f: Poisson's ratio of thin film.

- λ_{wr}: Wrinkling wavelength $\propto t_f$.

The induced compressive force (F_c) is directly proportional to the film thickness. As the thickness increases, cracking begins to substitute the wrinkling in the film to account for mismatch.

The resulting surface wrinkling of Al is shown in Fig. 3.13 using laser microscopy. This behaviour results in the sensors exhibiting a higher sensitivity as opposed to sensors with a perfectly flat surface as shown in Fig. 3.14. This is due to the high amount of variations in the electric field gradients caused due to the hill-valley like nature of the surface.

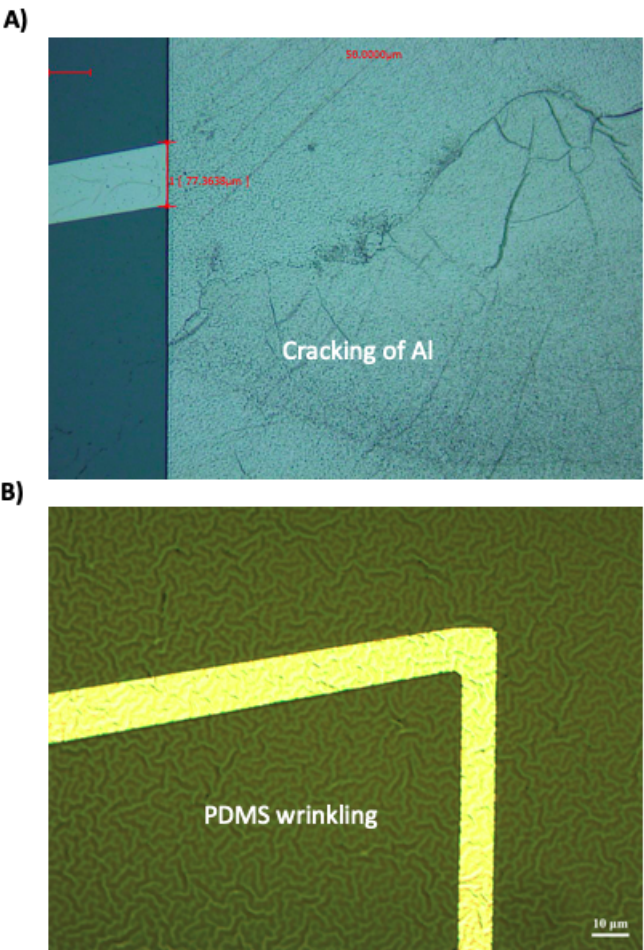Figure 3.12: A) Cracking of 1.5 μm thick Al sputtered at 25°C. B) Surface wrinkling of PDMS (spin speed = 8000 rpm).

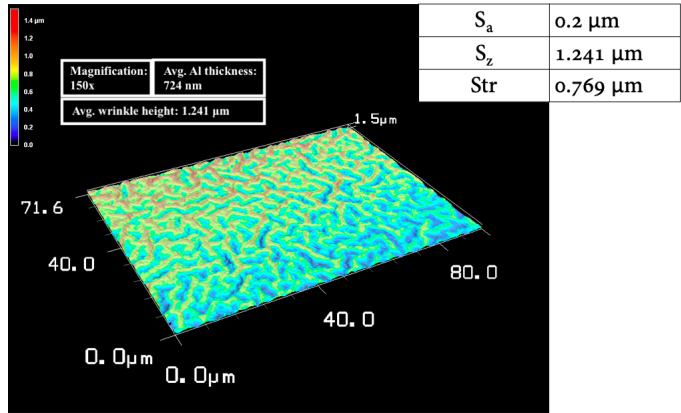|	
S_a	0.2 μm
S_z	1.241 μm
Str	0.769 μm

Figure 3.13: 3D laser microscopy of sputtered Al film on PDMS

The mean height, maximum height and uniformity are represented by S_a, S_z and Str respectively, along a cut-line drawn at the center of the surface. The maximum value of Str is 1 denoting a completely flat surface. The maximum height has been chosen for 2D analysis of a wrinkled capacitor in COMSOL. The base capacitance as well as the change in capacitance under deformation is higher in the case of wrinkled capacitor (C_{rough}, ΔC_{rough}, Str < 1) as opposed to a capacitor with flat plates (C_{flat}, ΔC_{flat}, Str = 1) as seen in Fig. 3.14. This is due to the increase in surface area of the plates as well gradient of electric field lines on plate wrinkling.
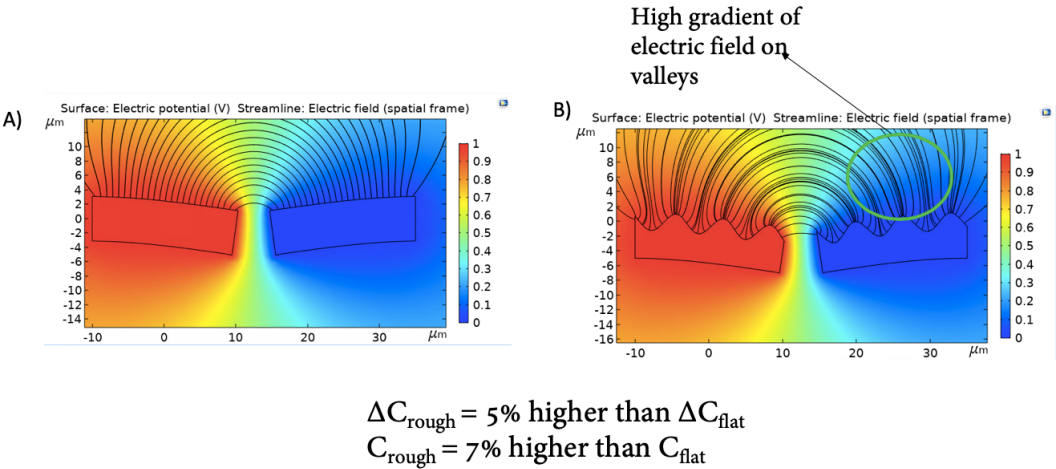
3

$$\Delta C_{rough} = 5\% \text{ higher than } \Delta C_{flat}$$
$$C_{rough} = 7\% \text{ higher than } C_{flat}$$

Figure 3.14: Capacitive response of a two-dimensional dual plate co-planar capacitor with A) Flat plates (Str = 1). B) Wrinkled plates (Str < 1).

Metal-on-Metal patterning: Patterning of metal on metal can also be achieved utilising a similar method as described above. Since aluminium forms a native insulating oxide on its surface in ambient environments, prior to deposition of the second layer, an etch step is required to remove this oxide and ensure an electrical connection between the top and bottom layer. This is performed using an Argon plasma in Sigma for 15 seconds driven by an alternating current. The summary of the parameters is given in Table 3.2. *It must be kept in mind that the necessity for metal-on-metal patterning arises only when thick contact pads (> 1µm) are desired for wire-bonding, while keeping the thickness of the sensors lower in order to improve compliancy.*

Table 3.2: Sigma RF etch parameters prior to second Al deposition.

Gas Flow (sccm)	Duration (sec)	RF Power (W)
40	15	300

On account of the Argon ion bombardment the bottom Al layer exhibits non-uniformity which can be visualised using Scanning Electron Microscopy as shown in Fig. 3.15a. The bottom Al film has a thickness of 1.5 μm which assists in reducing any adverse effects such as electrical disconnections which might occur due to ion bombardment. However,

due to the large difference in step height, uniform step coverage is challenging as seen in Fig 3.15b. Due to the vertical side-wall obtained after dry etching of the bottom Al film, deposition of a low thickness (in this case, t_f = 250 nm) thin film on top exhibits discontinuity. In order to curb this, the following steps can be carried out individually or in combination.
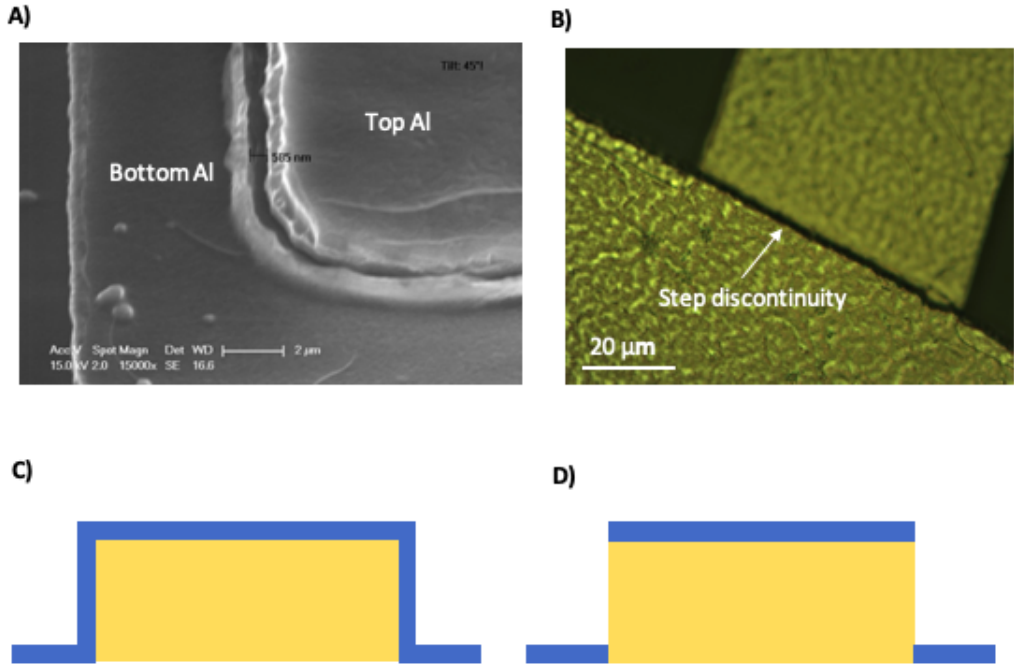
Figure 3.15: A) SEM micrograph of metal-on-metal patterning. B) Non-conformal deposition of metal on metal. C) Expected conformity. D) No conformity due to steep sidewall [yellow: thick bottom Al, blue: thin top Al].

- Wet etching of the bottom Aluminium film instead of dry etching. Due to the more pronounced isotropic nature of the etch, under-etching takes place leading to gentler side-walls and better sputtering conformation.

- Thickness reduction of bottom Al film so as to enable a reduced etching duration. Due to the chlorine content of the plasma, a certain degree of isotropy is present during the dry etch [76] which leads to removal of aluminium close to the mask edges. This effect can be better visualised with the plates of the sensors in Fig. 3.16.

- Increase in the thickness of the top Al film to account for etching of PDMS during RIE over-etch steps.

Figure 3.16: Optical micrograph of etched Al and PDMS at mask edges.

3.3.3. PHOTOLITHOGRAPHY

After deposition of the metal, 1.4 μm of positive photoresist (Shipley SPR3012) is spin coated on the wafer which acts as the masking layer using the EVG 120 coater-developer system. All the baking st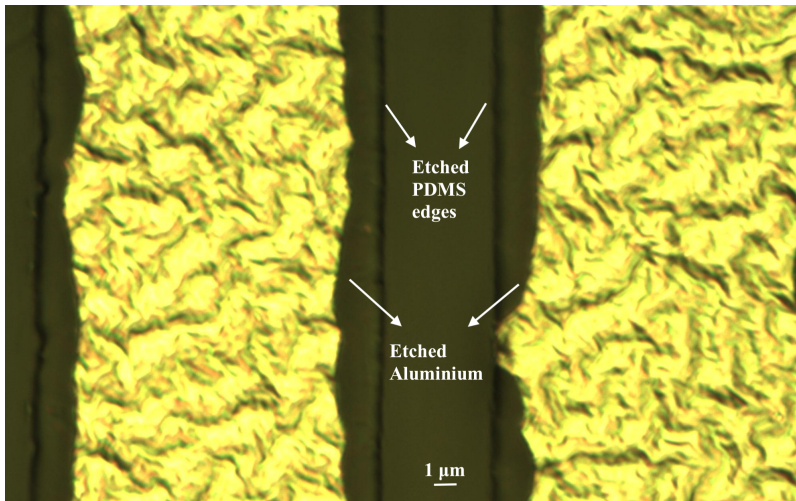eps, from coating to post development, have been carried out manually at a temperature of 90°C for a duration of 90 seconds. The full-wafer mask exposure is performed using a hard contact between the wafer and mask (SUSS MicroTec MA/BA8 Mask Aligner). The duration of exposure depends on the exposure dose and light intensity. Due to Aluminium's high reflectivity, the standard dose associated with the photoresist is reduced to 80% of its value leading to a required exposure time of 8-10 seconds. Longer durations lead to over-exposures which cause further thinning of sensor dimensions. This is shown in Fig. 3.17 for an exposure time of 20 seconds. The reduction in line-width leads to sensors with metallization ratios less than 0.5 which results in a drop in surface area and by extension base capacitance and sensitivity.

The reduction in plate width is shown in Fig. 3.18a-d which occurs due to the combined effects of over-exposure as well as chlorine etching. These effects are more pronounced in sensors with gaps and widths lower than $10\mu m$ wherein discontinuities arise in the capacitor plates.

3.3.4. ETCHING

After exposure, Al is etched using a HBr/Cl$_2$ inductively coupled plasma (ICP) in Omega with a plate temperature of 25°C and at a gas pressure of 5 mTorr. The process consists of an aluminium oxide removal followed by bulk etching of aluminium with end-point detection. Over-etching is done with end-point detection disabled in order to remove any Al residues on the PDMS. This process is also necessary in order to reduce the leakage of the sensors since metal residues can generate current paths as well as increase the conductivity of the PDMS leading to sub-optimal dielectric properties. The etching pa-
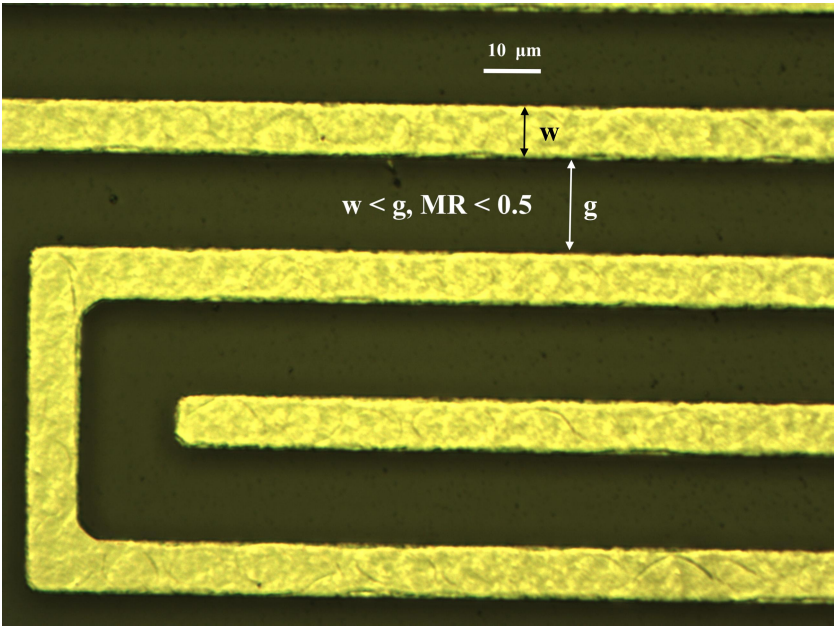
Figure 3.17: Reduction in metallization ratio due to photoresist over-exposure during lithography.

rameters are summarized in Table 3.3 and an Al etch rate of 1285 nm/min was observed.

Table 3.3: Plasma etch parameters of 1.5 μm thick Al

Etched material	Cl_2 flow (sccm)	HBr flow (sccm)	ICP power (W)	RF Power (W)	Duration (sec)
Aluminium Oxide	30	40	500	50	Endpoint enabled
Bulk Al	30	40	500	35	Endpoint enabled
Over-etch 1	15	30	500	35	60
Over-etch 2	15	30	500	35	90

In order to derive the selectivity of the resist mask and PDMS to Cl_2/HBr, height measurements have been done after each patterning step as shown in Fig. 3.19. The etch rate is hence approximately 114 nm/min for positive resist and 400 nm/min for PDMS for the etching conditions mentioned in Table 3.3.

(a) Mean plate width = 15 μm (Expected = 20 μm)

(b) Mean plate width = 7.5 μm (Expected = 10 μm)

(c) Mean plate width = 2 μm (Expected = 5 μm)

(d) Mean plate width = 35 μm (Expected = 40 μm)
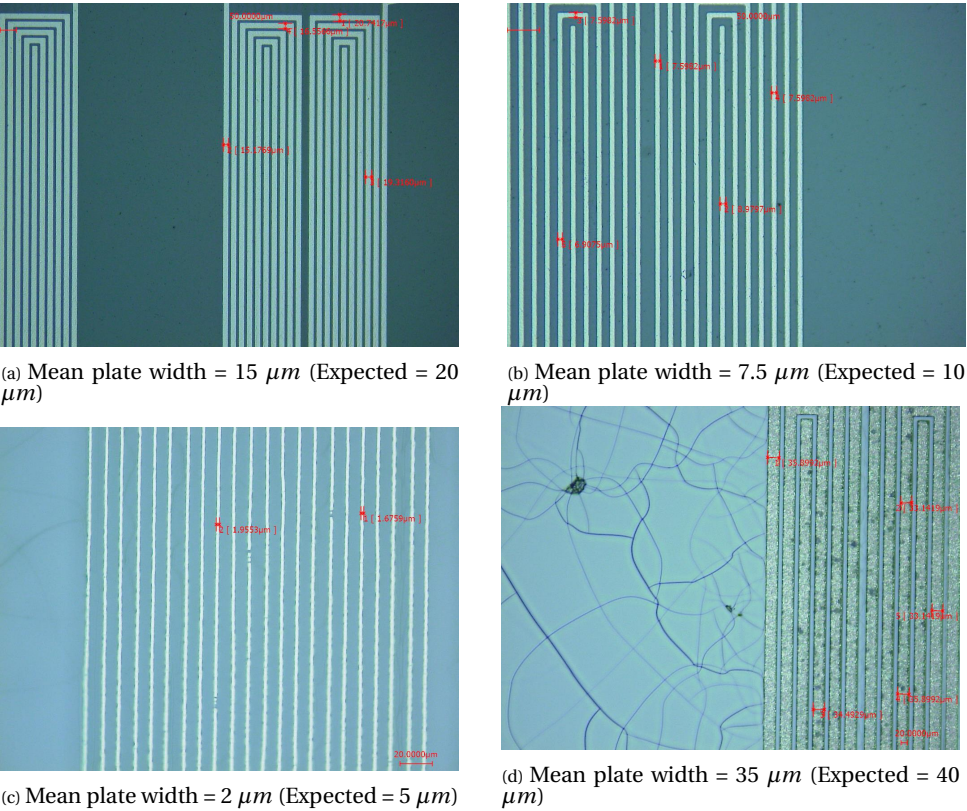
Figure 3.18: Expected vs fabricated width of capacitor plates.

Figure 3.19: Step height results A) Prior to resist exposure. B) After exposure and plasma etching. C) After resist strip.
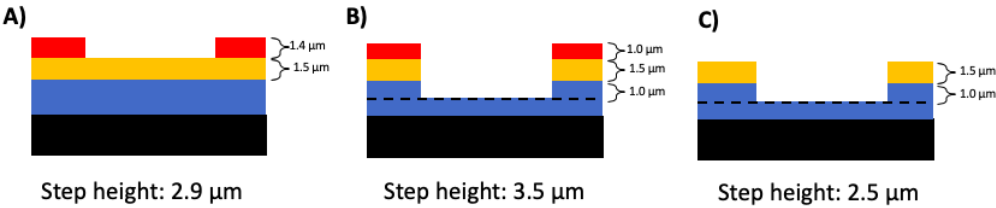
The etching of the surrounding PDMS can be reduced by removing the second over etch step and reducing the duration of the first over etch as well, with the parameters listed in Table 3.4. This technique is sufficient to etch all pure Al films with thickness lower than 1 μm.

Table 3.4: Plasma etch parameters of $< 1~\mu m$ thick Al.

Etched material	Cl$_2$ flow (sccm)	HBr flow (sccm)	ICP power (W)	RF Power (W)	Duration (sec)
Aluminium Oxide	30	40	500	50	Endpoint enabled
Bulk Al	30	40	500	40	Endpoint enabled
Over-etch 1	15	30	500	40	10

If the etching is insufficient, the recipe can be re-done by disabling end-point detection and etching for 2-5 seconds. If the desired thickness is more than 1 μm, wet etching of the metal is a viable alternative as compared to RIE. Thick Al contact pads of 1.5 μm are etched at room temperature in a mixture of phosphoric acid, nitric acid and acetic acid (PES 77-19-04, Selectipur®) for 35 minutes with 5 minutes of over-etch. Due to the high selectivity of wet etchants, neither photoresist nor PDMS are etched. This method is however unsuitable for etching thin film spiral sensors due to the following factors:

- The isotropic nature of wet etching leads to an under-cut below the masking layer which leads to a reduction in sensor width.

- The low contact area between the sensors and the PDMS coupled with the poor adhesion of metal to PDMS leads to removal of sensors from the substrate during etching and/or rinsing in water as shown in Fig. 3.20. It is known that the drop in contact area is the primary reason behind detachment of sensors since the contact pads (1 mm x 1 mm) were still intact after wet etching and rinsing.
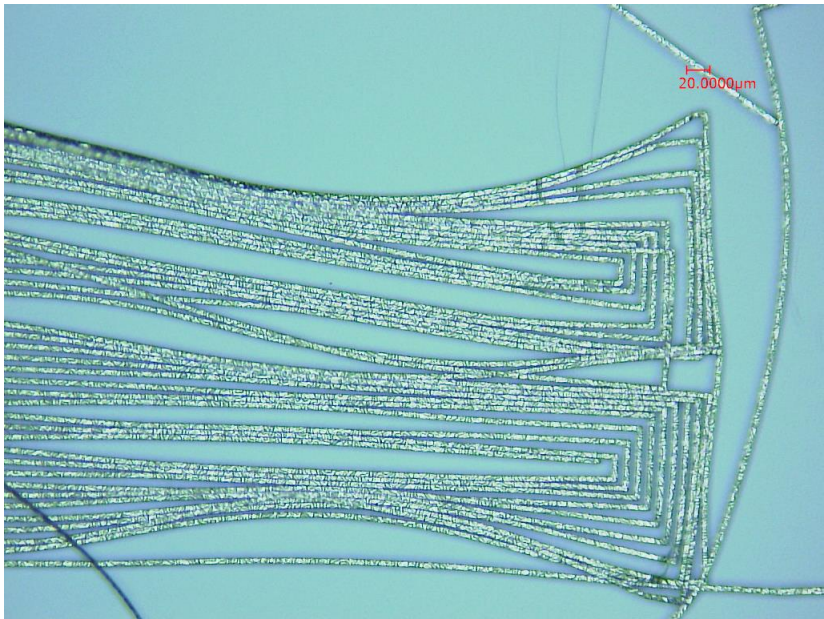

Figure 3.20: Detachment of spiral sensor from PDMS after wet etching in PES.

3.3.5. RESIST REMOVAL

For structures which have been patterned using only wet etching, rinsing of the wafer in acetone at room temperature for a duration of 5 minutes is sufficient for resist removal.

However, due to hardening of resist in HBr/Cl$_2$, structures which have been dry etched would require exposure to oxygen plasma for resist stripping. Since oxygen also effects PDMS, the duration and the power must be carefully controlled. It has been found that cracking of PDMS occurs after exposure to 600 W plasma for 1 minute. A similar outcome is observed when exposure is done at 200 W for 5 minutes. Hence, both acetone and low power plasma can be utilised to remove resist after dry etching by first rinsing in acetone for 15 minutes followed by a plasma exposure at 200 W for 1 minute. The imaging contrast between resist and the underlying metal can be best observed using SEM at low beam power (1 kV to 5 kV) as shown in Fig. 3.21.
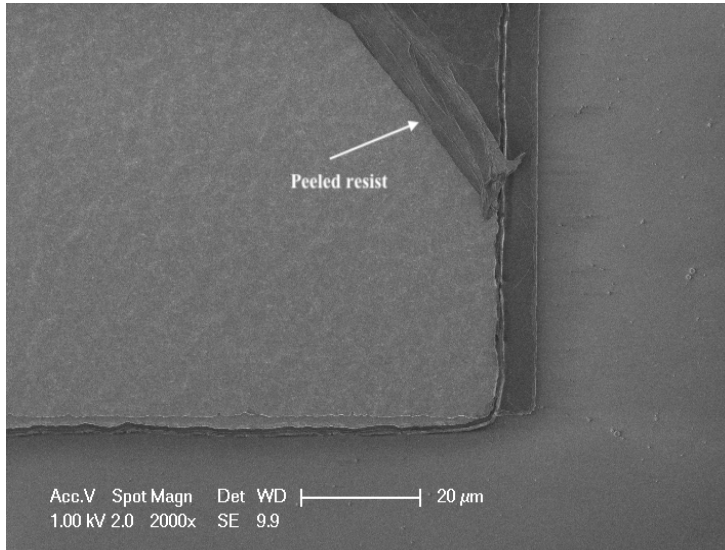
Figure 3.21: SEM image of peeled resist in acetone.

The resist begins to peel away in acetone after which it is completely removed in oxygen plasma. It must be noted that in this process, incomplete removal of resist does not adversely effect the properties of the sensor. Since the thickness of the resist layer is only 1.4 μm, probing as well as wire bonding can be well accomplished. However, for metal-on-metal patterning, complete removal of resist is a necessity so as to avoid disruptions in current flow between the two metal films.

Encapsulation: In order to further emulate the encapsulation step in Fig. 3.7p, a second layer of PDMS is spin coated at a spin speed of 2000 rpm for 30 seconds leading to a thickness of approximately 50 μm. After spin-coating, a uniform layer of PDMS was obtained with the sensors intact and sandwiched between two PDMS layers. An optional step of plasma treatment can be performed in order to improve PDMS-PDMS bonding prior to spin-coating of the second layer. The wafer after encapsulation is shown in Fig. 3.22.

The peeling of the second layer of PDMS causes partial detachment of the flexible sensors as shown in Fig. 3.23a and 3.23b.

Figure 3.22: Intact spiral sensors after encapsulation between two layers of PDMS.

3.4. SILICON PATTERNING FOR FABRICATION OF MICROPILLARS

In addition to patterning of sensors on PDMS, the initial steps required for their integration into the EHT platform have been carried out as well, up-to moulding of the Silicon wafer using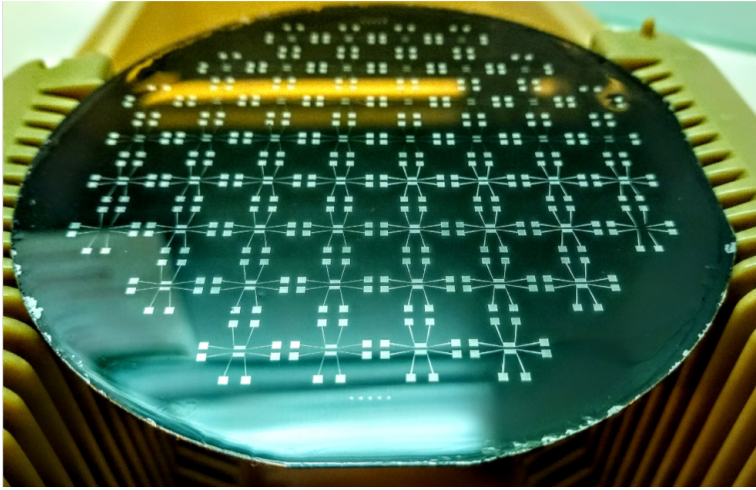 Deep Reactive Ion Etching (DRIE). For this purpose, double sided polished wafers have been utilised for patterning on the front-side (FS) as well as back-side (BS) of the Si(100) wafer. The steps have been summarised in Fig. 3.6. Due to the presence of multiple layers, alignment marks have been dry etched into the Si wafer as the zero layer prior to oxide growth.

The patterning of the zero layer alignment marks is done on both the front as well as back side of the wafers while ensuring FS-to-BS alignment. Prior to oxide growth, the wafers are cleaned in 99% nitric acid and water to ensure efficient oxidation. Wet oxidation is carried out for a period of 14 hours at a temperature of $1100°C$ (Tempress Furnace) homogeneously on both sides of the wafer. The resulting oxide thickness is measured using interferometry by the Leitz MVP-SP system (Hexagon MI). The measured average thickness is 2668.49 nm and 2667.30 nm on the front and back side of the wafer, respectively. Post thermal oxidation, a second layer of oxide is deposited utilising plasma enhanced chemical vapour deposition (PECVD) in the Novellus system (Lam Research Corp.) at a temperature of $400°C$ on the front side of the wafer. The thickness of the layer is linearly dependent on the duration of deposition. Since the refractive index (N_f) of the PECVD deposited oxide is similar to that of thermal oxide ($N_{f(ThermalSiO_2)} = 1.42$, $N_{f(PECVDSiO_2)} = 1.39$ [77]), the same recipe can be utilised to calculate the composite oxide thickness using interferometry after PECVD with the results highlighted in Table 3.5.

Table 3.5: Front-side composite oxide mask thickness.

PECVD Duration (s)	Avg. Thermal + PECVD Oxide Thickness (nm)
47.6	5974.21
49	6172.55

Figure 3.23: Partial detachment of flexible spiral sensors on peeling of second PDMS layer.

After oxide deposition, photoresist of thickness 3.1 μm (Shipley SPR3027) is spin-coated on the substrate. The resist is then patterned using contact lithography (SUSS Mask Aligner) for a duration of 30 seconds. The oxide is etched in SF_6 and O_2 plasma by RIE (Drytek Triode 384T Plasma Etcher) for 10 minutes. Residual oxide ($<= 100$ nm) is etched in BHF at room temperature for 14 minutes. The isotropic nature of wet etching leads to angled side walls in the oxide-mask which might effect the size of the pillars. Hence wet etching of residual oxide on the front-side of the mask is not recommended for more than 15 minutes. The step height was measured using the Drytek profilometer as shown in Fig. 3.24.
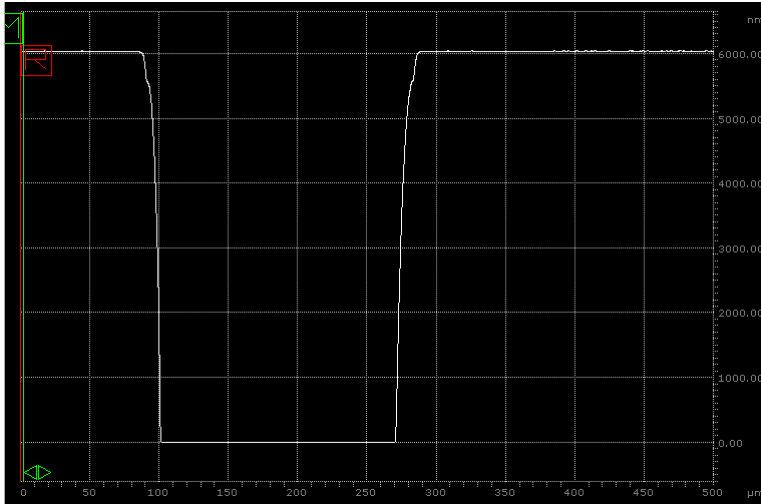
Figure 3.24: Step profile of SiO$_2$ after etching in BHF for 14 minutes.

The side-wall generation can be seen in the trace of the output with a lateral etch of 17 μm on either side of the pillar. After completion of etching, the resist is stripped in oxygen plasma (Tepla) at a power of 1000 W. The patterned mask is shown in Fig. 3.25 and is used for further deep reactive etching of micropillars in the Si substrate which is discussed in subsection 3.4.1.

Figure 3.25: Micropillar oxide mask after etching.

3.4.1. Deep Reactive Ion Etching of Silicon

In order to fabricate a mould for the PDMS pillars, deep reactive ion etching (DRIE) of Si is utilised. DRIE process are often beneficial for the development of high aspect ratio structures which require careful etching of the substrate and high selectivity with oxide and resist masks. Alternatively called the Bosch process, the steps are summarized in Fig. 3.26 with the Si substrate represented in black.

The etching cycle can be split into four sub-processes which are mentioned below:

- Break-through of the substrate with SF_6 plasma followed by first etch of Si.

- Deposition of a passivation layer on the exposed Si surface using CF_4 plasma. The deposited polymer layer exhibits properties similar to Teflon.

- Anisotropic etch using SF_6 plasma. During this step this Si is etched vertically while being laterally protected by the passivation layer.

- Re-deposition of polymer on the exposed surface of Si in CF_4 plasma followed by the second SF_6 etch.

The alternate etch-passivation cycle leads to the scalloping effect which generates a tapered structure as shown in Fig. 3.27 for an etch depth of 660 μm. The ratio of the top and bottom perimeter is usually above 0.9 (the ideal being 1). This effect was considered in Chapter 2 as well, during integrated sensors simulations.
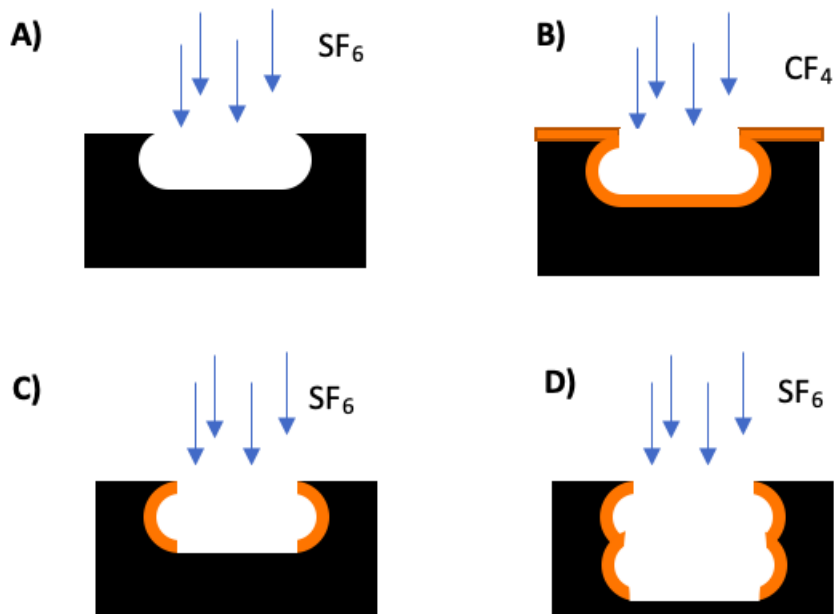
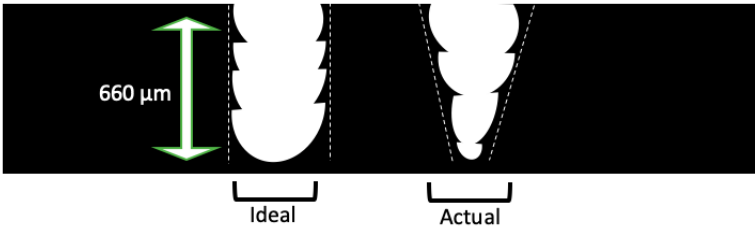Figure 3.26: Deep reactive ion etching of Si.

Figure 3.27: Ideal vs actual profiles of Si after DRIE.

The etching steps have been performed in Rapier Omega RIE system at a plate temperature of 20°C. A total of 930 cycles are required to etch 660 μm considering an average etch rate of 700 nm/cycle.
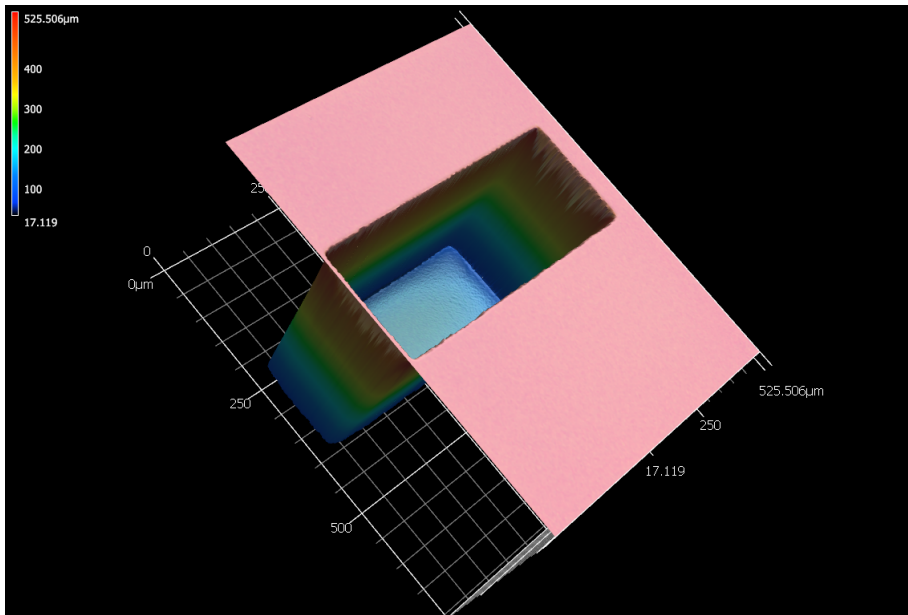
Figure 3.28: Laser microscopy of etched Si after 700 cycles.

Due to the deposition of protective polymeric layers during the etching step, the wafers are exposed to oxygen plasma in Tepla (PVA TePla America, Inc.) for a duration of 15 minutes at a power of 1000 W and then cleaned in nitric acid and water prior to second oxide growth. The wafers are kept overnight in a furnace in an oxygen flow for 19.5 hours for the growth of protective oxide layer. Subsequently, PECVD oxide is deposited on the back side of the wafer, leading to an oxide of average thickness equal to 8.5 μm which will be further utilised as a mask for etching through 1000 μm of Si as shown in Fig. 3.6i. The patterning of the back-side oxide mask can be achieved using SF$_6$ and O_2 plasma in the Drytek Triode systems as well. There however exists a possibility of stress development in thick wafers due to mechanical clamping mechanism. Hence wet etching of oxide can be alternatively carried out.

3.5. CONCLUSION

In this chapter the patterning of spiral capacitive sensors has been carried out on PDMS followed by their successful encapsulation in a second layer of PDMS. Due to the low line widths of the sensors, wet etching was replaced by dry etching in order to preserve geometry as well as ease the fabrication of the sensors. The effects of plasma treatment on the adhesion of metal to PDMS require further investigation. It has been found out that the combination of plasma treatment along with exposure to chemicals such as Sodium Dodecyl Sulfate (SDS) contribute to adhesion enhancement of metal to PDMS as well as the quality of deposited metallic films [78].

The exposure and etching duration during photo-lithography and dry etching respectively have been reduced so as to accommodate for the high reflectivity of Al and the

rapid etch rate of Al in Chlorine plasma as the first attempt towards achieving optimised sensor structures. However, due to equipment unavailability the proposed improvements are yet to be carried out. Fortunately, the first set of sensors developed have the ability to be successfully utilised for their first level assessment using wafer level electrical characterization. The COMSOL simulations have been re-adjusted keeping in mind the changes in the dimensions of the sensors during microfabrication.

From the perspective of micropillar fabrication, the Si substrate has been etched using DRIE for the purpose of PDMS moulding. At this stage the uncured PDMS once poured into the holes will obtain the form of micropillars. A critical juncture occurs during step M in Fig. 3.7 where the PDMS is etched so as to minimize t_1. Etching of PDMS in CF_4 and oxygen is a promising method to achieve the same and can be carried out without the presence of a mask since we require etching of the entire un-patterned layer [79]. Subsequently, the sensors are patterned using the process flow in Fig. 3.5 followed by encapsulation. In order to etch away the substrate for the development of the final sensor-integrated EHT platform, a second DRIE is carried out. It is still yet to be deduced if thicker contact pads ($> 1\mu m$) are required for wire bonding. The procedure of wire bonding is shown in Fig. 3.29. Metal-to-metal contact is achieved via either ultrasonic energy and/or thermal energy. Since the metal is encapsulated within a soft polymer, wire-bonding could be challenging and has the ability to damage the contact pads. Low energy alternatives such as flip chip bonding are not achievable due to the presence of interfering structures.
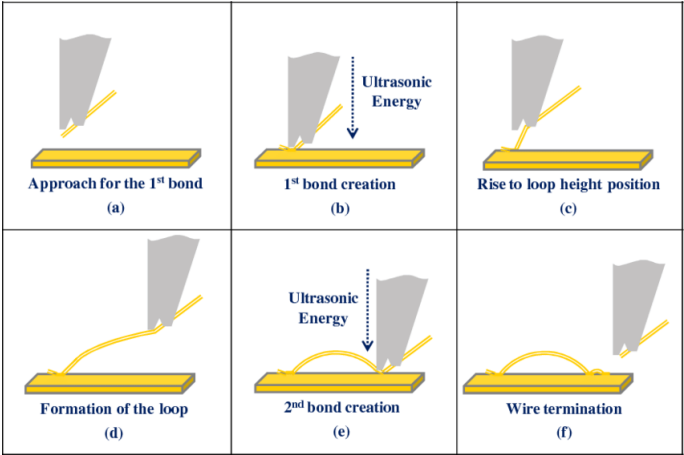
Figure 3.29: Wire-bonding procedure for interconnection of sensors to external environments such as PCBs [80].

The flowchart of the process carried out at EKL, TU Delft is attached to Appendix F. The fabricated sensors prior to their encapsulation in the second layer are characterized using capacitive measurement techniques and modeled in Chapter 4.

ELECTRICAL CHARACTERIZATION AND READ-OUT CIRCUITRY

This chapter presents the preliminary measurements performed on the fabricated co-planar capacitors and derivation of appropriate measurement setup parameters. Details of the procedures and experimental results are presented in this chapter. A potential read-out circuit is designed and simulated with SPICE, which is the final step towards the development of a fully integrated EHT sensor. Lumped element models of the designed and fabricated sensors are proposed and their suitability is tested by on-chip probed measurements.

4.1. MEASUREMENT SETUP

On-wafer probing of the sensors and test structures is performed in a multi-needle probe station with electromagnetic shielding (FormFactor, formerly Cascade Microtech) at room temperature as shown in Fig. 4.1. Two channels are utilised for both IV and CV measurements. Depending on the desired output the following instruments are used:

- I-V measurements: 4156C Precision Semiconductor Parameter Analyzer (Keysight Technologies).

- C-V measurements: 4284A Precision LCR Meter (Keysight Technologies).
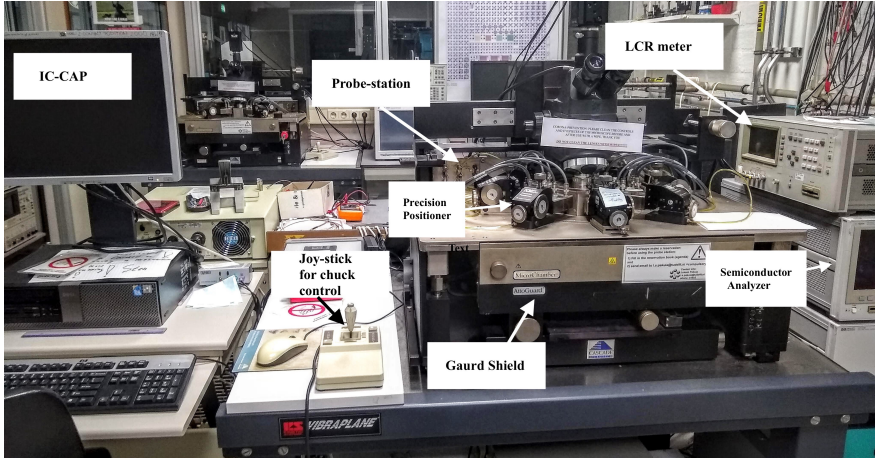
Figure 4.1: Measurement setup for I-V and C-V measurements.

The measurements are semi-automated with the IC-CAP (IC Characterization and Analysis Program) modelling software which is also utilised for defining the electrical channel inputs such as driving voltage as well as instrument calibration prior to measurements. The sensors utilised for the preliminary characterization studies have a thickness of 250 nm while the PDMS is $\sim 5\mu m$. As discussed in Section 3.3, overexposure during photolithography has led to the reduction in width of the plates of the capacitors. In order to account for this, all simulations in COMSOL have been re-run with the new geometrical parameters and used as a benchmark for the experimentally derived baseline properties of the sensors.

4.2. I-V MEASUREMENTS

Prior to C-V measurements, I-V characteristics of the four different test structures are obtained. These structures comprise of tapered metal lines having the same layout as the interconnects implemented for connecting the on-chip spiral capacitors to the contact pads as shown in Fig 4.2. The terminating width of the interconnect is denoted by W_{CP} and is defined for each sensor type as shown in Table 4.1.

Table 4.1: Terminating width of test metal lines.

Sensor Type	W_{CP}
A	80 μm
B	40 μm
C	20 μm
D	160 μm
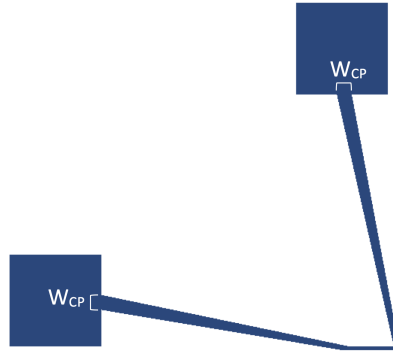
Figure 4.2: Test structures for on wafer I-V measuremets

The I-V measurements of the test interconnects provide the following advantages.

- Compatibility check between the simulated and measured value of the interconnect resistance.

- Conformity check of bimetallic layers with bottom and top layer thickness of 1.5 μm and 250 nm respectively.

- Compliance limit as per electromigration rules are tested. The derivation of input conditions such as current compliance and input voltage sweep limits for I-V measurements will be further utilised while confirming extremely low leakage behaviour of the PDMS.

The input conditions defined in IC-CAP are shown in Table 4.2. Medium integration mode is used to average the values corresponding to every measurement point.

Table 4.2: Setup of IC-CAP for I-V measurements.

		Unit
Input parameter	Voltage	V
Sweep type	Linear	
Min. value	-100	mV
Max. value	100	mV
Measured parameter	Current	A
Compliance limit	10	mA

As shown in Table 4.2, current compliance is set at 10 mA to avoid electromigration effects considering a typical value of approximately 1mA/μm as the safe limiting current density. The output current is shown in Fig. 4.3 for each test structure with respect to the swept input voltage. The inverse of the slope (V/I) is the resistance of the interconnect path.
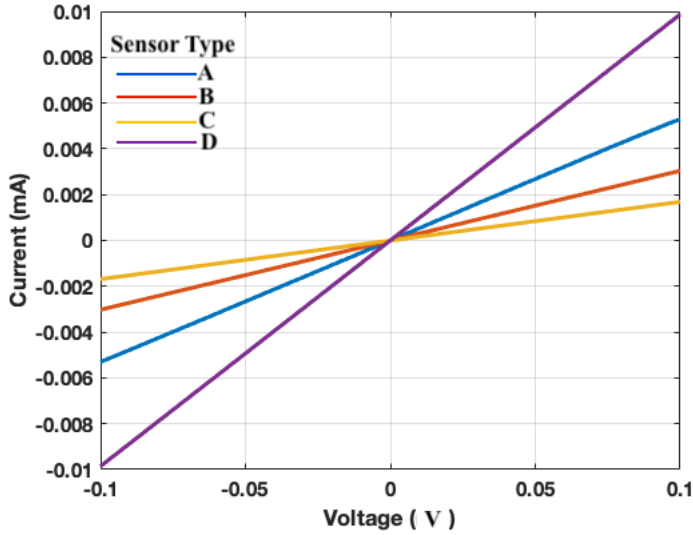
Figure 4.3: Measured I-V behaviour of test structures in IC-CAP.

It can be seen that the measured resistance is in excellent agreement with the simulated results.

Table 4.3: Measured vs simulated resistance of test structures

Sensor Type	Measured Resistance (Ω)	Simulated Resistance (Ω)
A	18.86	19.20
B	32.89	32.70
C	59.20	57.32
D	10.13	10.11

Structures represented by the pattern shown in Fig. 4.2 were also fabricated with thick contact pads (1.5 μm) along with thin sensors and interconnects (250 nm) by metal on metal patterning as descried previously in section 3.2. With the help of I-V measurements, the disconnectivity arising during bimetallic fabrication is confirmed. Due to the large step height, an open contact is formed as seen in Fig. 4.4. Hence, metal on metal patterning was not utilised for fabrication of sensors for C-V measurements.

The current measured when the substrate was grounded and the sensor probed using the setup parameters mentioned in Table 4.2 was in the order of pA as well indicating good insulating and low leakage behaviour of the spin-coated PDMS as well as removal of aluminium particles during RIE over-etching.
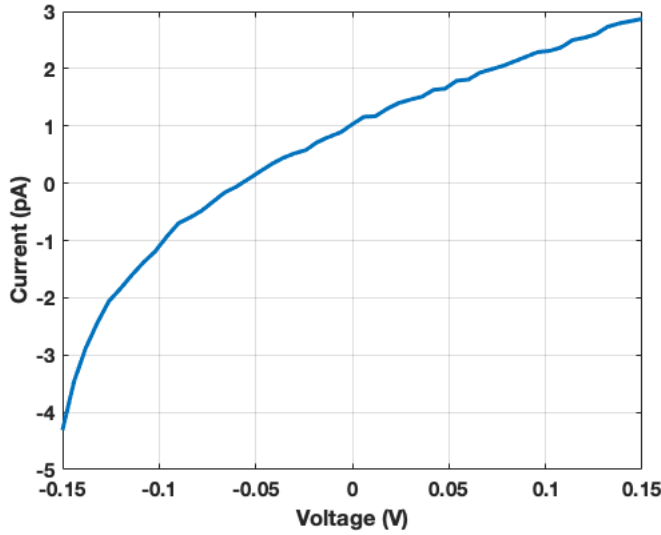
Figure 4.4: I-V measurement of test structure fabricated using metal-on-metal patterning.

4.3. C-V MEASUREMENTS

To measure the base capacitance of the spiral sensors, the appropriate frequency range will be chosen in accordance with the best possible measurement accuracy which can be obtained using the LCR meter. Prior to carrying out the measurements, the approximate electrical model of the capacitive sensors on the Si wafer is presented. The derived model is further used during the instrument setup for C-V measurements. Subsequently, the measurement results are presented in subsection 4.3.2.

4.3.1. EQUIVALENT ELECTRICAL CIRCUIT MODEL

Prior to electrical characterization, the equivalent electrical model of the capacitors on PDMS and Si substrate is derived while taking into account parasitic components as shown in Fig. 4.5a when the substrate is floating and Fig. 4.5b when the substrate is grounded. The main parasitic components which arise when the substrate is floating and when an AC input signal (V_{AC}) are:

- R_{PDMS}: Conduction current leakage path. This is negligible for PDMS on account of its very high resistivity ($10^{15}\Omega cm$ [81]).

- C_{par}: Parasitic capacitor between each electrode and the Si substrate. Since the substrate is floating, the bottom plates formed by these capacitors are connected through the parasitic resistance, R_{par}, representing the AC leakage path through the substrate. The latter effect is dependent on the effective value of R_{par}. Since the resistive path occurs near the surface of the substrate, R_{par} is high enough to diminish the effect of C_{par}.

When the substrate is grounded as represented by Fig. 4.5b, additional displacement current leakage paths are generated to the ground via resistors R_{par1} and R_{par2} during

AC excitation. The lumped electrical circuit model can be analysed in the frequency domain based on the effective admittance, Y_{eff}
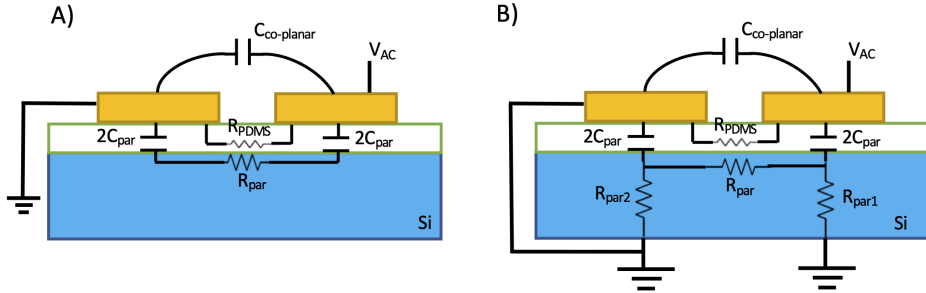
Figure 4.5: Equivalent circuit model of Metal-Insulator-Semiconductor with A) Floating substrate B) Grounded substrate.

$$Y_{eff} = j\omega C_{co-planar} + \frac{\frac{j\omega C_{par}}{R_{par}}}{j\omega C_{par} + \frac{1}{R_{par}}}$$

$$= \frac{R_{par}C_{par}^2\omega^2}{1 + R_{par}^2 C_{par}^2 \omega^2} + j\omega(C_{co-planar} + \frac{C_{par}}{1 + R_{par}^2 C_{par}^2 \omega^2}) \tag{4.1}$$

$$Z_{eff} = \frac{1}{Y_{eff}} \tag{4.2}$$

If $(R_{par}C_{par}\omega)^2 \gg 1$, the effective admittance can be simplified to

$$Y_{eff} = \frac{1}{R_{par}} + j\omega(C_{co-planar} + \frac{1}{R_{par}^2 C_{par} \omega^2}) \tag{4.3}$$

$$Z_{eff} \approx R_{par} + \frac{1}{j\omega C_{co-planar}} \tag{4.4}$$

For Eq. 4.4 to be valid, $(R_{par}C_{par}\omega)^2 \gg 1$ must to be satisfied and ω should be chosen is such a way that $f \gg \frac{1}{2\pi C_{par} R_{par}}$ where f is the excitation frequency. An interesting observation is that both the real as well as the imaginary part of the admittance are dependent on frequency as seen in Eq. 1.2. The dependency of capacitance on the input voltage frequency is eliminated when the $C_{co-planar} \gg \frac{1}{R_{par}^2 C_{par} \omega^2}$. Experimentally, this occurs at frequencies above 200 kHz as shown in Fig. 4.6. Unstable measurements are denoted by the region R1 and stable measurements by the region R2. Observed instabilities have occurred during the following measurement conditions.
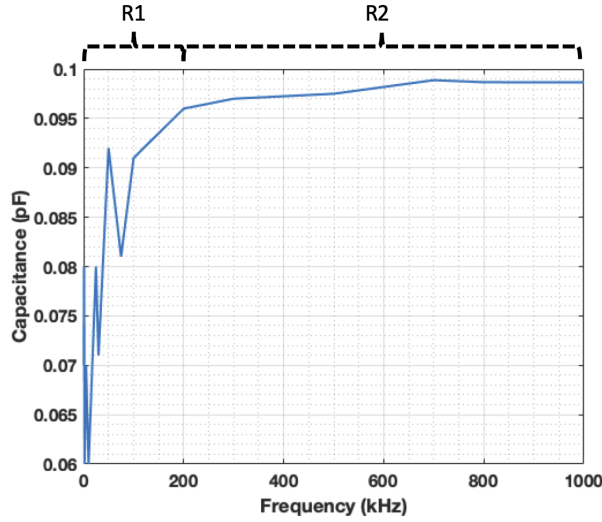
Figure 4.6: Measured capacitance of sensor D vs frequency at an input rms voltage of 5V$_{rms}$.

- When the input frequency is lower than 100 kHz.

- During probing of sensors on the soft substrate with thickness lower than a certain threshold. This threshold was found to be 250 nm. However this can be curbed by increasing the input test signal voltage in order to improve the signal to noise ratio.

- Probing through PDMS after encapsulation. Due to the deformations in the dielectric and the reaction forces generated in the probe tip, capturing a precise capacitance can be challenging. This can be overcome by wire bonding or by utilising a probe with a higher radius to reduce the stress on the needle.

Considering this condition, selecting the C_p-R_p model is a suitable choice for measurements performed in the LCR meter. C_p *is representative of the effective capacitance and R_p is representative of the effective resistance.* This result is in agreement with the measurement model suggested by Keysight for low capacitance measurements and demonstrate the effectiveness of the model [82]. Factors which contribute to satisfying $(R_{par}C_{par}\omega)^2 \gg 1$ are as follows.

- Selection of a high frequency. The highest available frequency in the LCR meter is 1 MHz which is chosen for all measurements. Secondary advantages provided by choosing a high frequency is the reduction of sensor impedance which reduces the effects of any electromagnetic interference and improvement in accuracy of LCR measurements. The dissipation factor of the PDMS is also lower at higher frequencies [82].

- Based on COMSOL simulations, the value of C_{par} can be approximated by Eq. 4.5.

$$2C_{par} = \frac{C_{co-planar}}{2} \tag{4.5}$$

The value of R_{par} is experimentally found out to be between 30-50 $M\Omega$ which confirms the good dielectric nature of PDMS as well as the confinement of current in the substrate to a low area at the surface. Hence the maximum available frequency of 1MHz is chosen for measurements.

It must be kept in mind that increasing the input frequency can contribute to increasing the inductive nature of the spiral capacitors due to a shift towards the resonance frequency of the sensors. Post resonance, the inductance of the sensors becomes more prominent as opposed to their capacitance and utilization of the $R_p - C_p$ model of the LCR meter is no longer valid. The resonance frequency of the sensors (f_0) is given by Eq. 4.6 wherein the inductance and capacitance are represented by L and C, respectively.

$$f_O = \frac{1}{2\pi\sqrt{LC}} \tag{4.6}$$

The inductance can be approximated by $85{\cdot}10^{-14}L_a N^{5/3}$ where L_a is the outer dimension of the sensor and N is the number of turns of the spiral [82]. On substituting the individual values of the parameters, the resonance frequency for all sensors is found to lie in the terahertz spectrum. Hence, baseline measurements can be safely carried out at a frequency of 1 MHz. In order to further improve the accuracy measurements, long integration duration is utilised coupled with an input voltage of $5V_{rms}$ to reduce the effects of noise (the sensor remains viable with a stable output at the maximum available input voltage i.e. 20 V_{rms}). The results of the capacitive measurements are shown in Fig. 4.7a-c for sensors A, B and D. The effects of overexposure, under-etching and cracking of PDMS are more pronounced in sensors with the lowest electrode width as witnessed by their higher dispersion. Sensor C was excluded from the studies due to the discontinuities arising in the plates with the initial fabrication parameters, as previously discussed in Chapter 3.

4.3.2. Experimental Results
A total of 48 devices were utilised for the measurement of the base capacitance of the spiral sensors and the results are shown in Fig. 4.7. It can be seen that the average values are in excellent agreement with the simulated capacitances. Differences arise between the simulated and measured values due to the following factors.

- Meshing differences in the domains surrounding the capacitor.

- Cracking in the PDMS layer which can reduce the effective dielectric constant.

- Vibrations and electromagnetic interference.

- Variations between devices during fabrication.
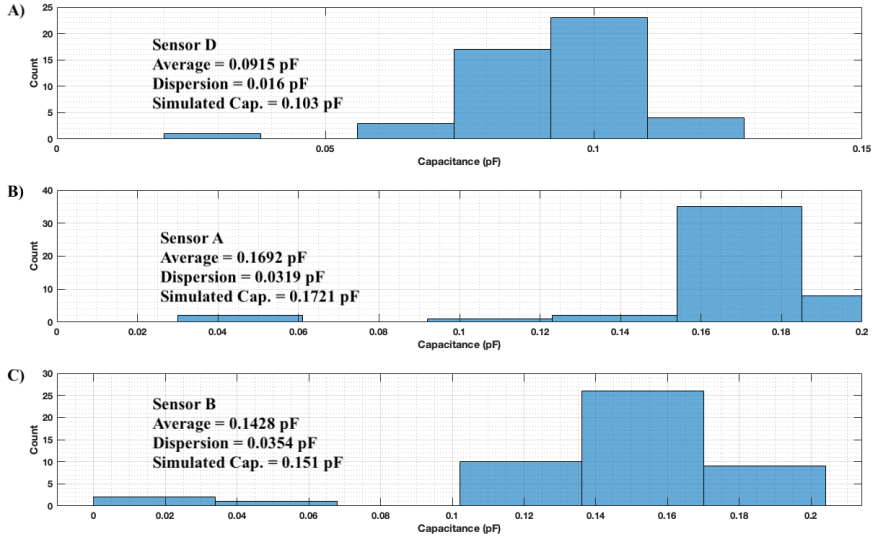
Figure 4.7: Distribution of fabricated sensor capacitance vs simulated capacitance at input frequency equal to 1 MHz and voltage equal to 5V$_{rms}$. A) Sensor D. B) Sensor A. C) Sensor B

Dielectric constant: In order to derive the dielectric constant (ϵ_r) experimentally, the wafers have been coated with 50 μm of PDMS and probed. Owing to the nature of the soft substrate and low thickness of metal, probing of the sandwiched layer becomes challenging which can be curbed by either increasing metal thickness or by reducing the thickness of the second PDMS layer. The latter is preferred since it leads to improvements in stability of all capacitive measurements. The sensor exhibiting the lowest dispersion has been chosen i.e. sensor D. The ratio of the capacitance before and after measurement was found to be 1/1.64. This ratio can be alternatively written by Eq. 4.7 utilising CPW theory where C$_{before}$ and C$_{after}$ denote the capacitance prior to and after the deposition of second layer of PDMS.

$$\frac{C_{before}}{C_{after}} = \frac{1 + (\epsilon_r - 1) \cdot q_1}{1 + (\epsilon_r - 1) \cdot q_1 + (\epsilon_r - 1) \cdot q_2} \tag{4.7}$$

The parameters q$_1$ and q$_2$ are a function of the elliptical integrals of sensor dimensions as well as the thickness of both the PDMS layers and hence remain the same after spin-coating of the second PDMS layer. The dielectric constant is found to be 2.8 at a frequency of 1 MHz and is in excellent agreement with the values provided by Sylgard which lie between 2.68-2.72 [81].

4.3.3. PRELIMINARY MEMS MEASUREMENTS

In order to emulate the response of the capacitors, deformation has been introduced at the edge of sensor D using the DCM series precision positioner with a needle diameter of 10 μm (Formfactor). The drop in capacitance vs time is shown in Fig. 4.8 an average of

the output of 10 sensors. An attoFarad resolution is obtained indicating optimal signal conditions and good shielding of the wafer. Care must be taken while introducing the third probe into the electric field space on account of its very high dielectric constant which causes warping of field lines similar to proximity sensors as shown in Fig. 4.9. The input voltage has been increased to $10V_{rms}$ to further reduce the effects of noise in the system. The change in output of the time-varying capacitor is challenging to quantify on account of this thin PDMS substrate and the low degree of resolution obtained with the precision meter wherein one quarter of revolution is equivalent to a vertical displacement of 60 μm.
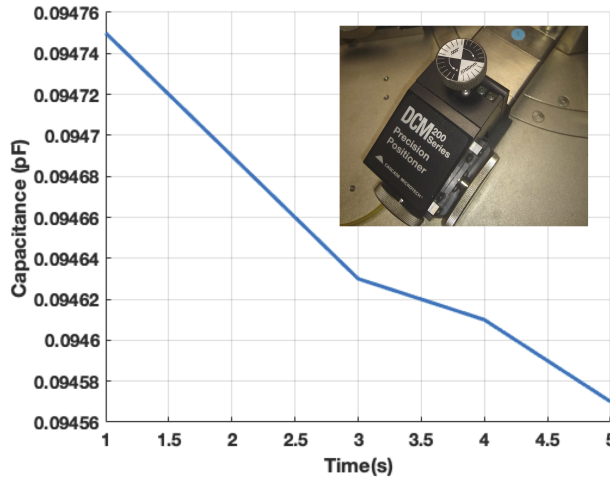
Figure 4.8: Change in capacitance of sensor D due to application of a time varying force at the edge of the sensor [inset: precision posiitoner]
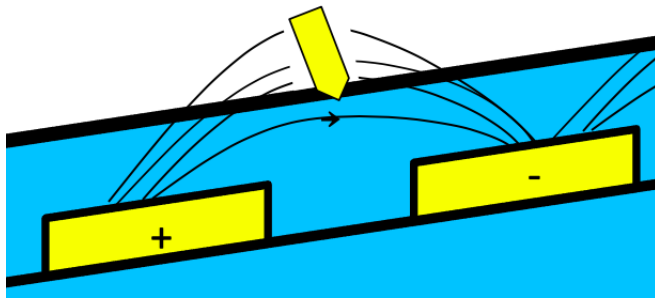
Figure 4.9: Warping of electric field lines on introduction of a third metallic probe into the electric field space.

4.4. TOWARDS A READ-OUT CIRCUIT

A commonly used used approach for measuring differential capacitance is by incorporating the capacitors in a relaxation oscillator circuit [84][85][86]. Relaxation oscillators are a class of oscillator circuits which provide cyclic charging and discharging of a stor-

age element such as capacitor or inductor.

The fabricated spiral capacitive sensors in this thesis have the capability to be integrated with the relaxation circuit shown in Fig. 4.10. The circuit is inspired by the work of Brookuis et al. [87] wherein the least change in capacitance obtained is 0.12 fF. The oscillator is shown in Fig. 4.10 wherein the green block constitutes of C_{rp} and C_{lp} where C_{rp} and C_{lp} are representative of the equivalent lumped model of the capacitors which undergo compression and expansion, respectively. C_{rp} and C_{lp} are excited with square-wave periodic signals of opposite phase. As a result, the current which flows out of the capacitive sensor will only be dependent on the change in capacitance due to pillar tilting. This current then flows into an integrator constituting of an op-amp and feedback capacitor (U4 and C5 in Fig. 4.10). The output voltage of the integrator (U4 in Fig. 4.10) is compared with the reference value, V4. Output of the comparator and its inverted form using U6 are fed back to the two inputs of the capacitive sensors. Charge is exchanged among C5, C6 and sensor capacitors since the potential at the negative input of the op-amp, U4, is constant due to virtual short between the two inputs of the op-amp. Resistor R2 carries a constant current at every half cycle. This is because R2 is connected between the output of the inverter, U6, and reference voltage V4 wherein output of the inverter is either V_{cc} or zero in every half cycle. Therefore, the capacitor (C5) is charged and discharged with a constant current on a periodic basis.

To derive the period of oscillation as a function of change in the sensor capacitance, the equations governing the operation of the circuit model are presented here. The amount of charge (q_{C6}) which is injected into the capacitor C6 is given by Eq. 4.8. where V_{op} is the output voltage of the op-amp. Therefore oscillation period is given by Eq. 4.8.

$$T_{osc} = 4R_2C_6 + 4R_2\Delta C \tag{4.8}$$

ΔC is a function of the base capacitance (C_0) and is written as

$$C_{rp} = \frac{C_0 + \Delta C}{2} \tag{4.9}$$

$$C_{lp} = \frac{C_0 - \Delta C}{2} \tag{4.10}$$
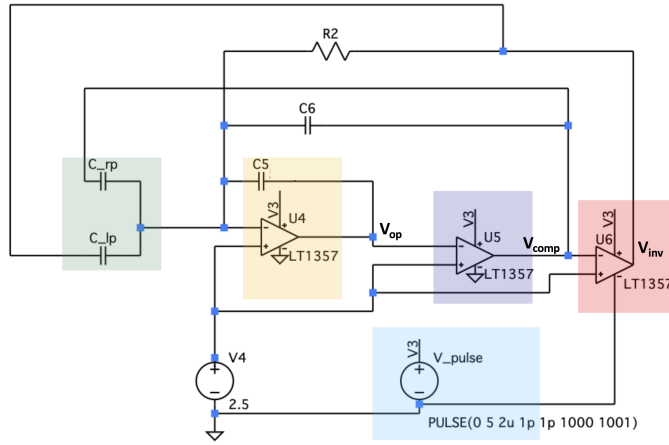
Figure 4.10: Proposed read-out circuitry for differential capacitance measurements in SPICE.

Eq. 4.8 shows the relative change in the period of oscillation, which is directly proportional to the change in the capacitance ΔC.

As a numerical example, consider the following values of the circuit parameters are to 10 pF is applied to this circuit to demonstrate the proof-of-concept as well as the applicability of Eq. 4.8. The change in the oscillation period derived using simulations is in excellent agreement with the values derived in Eq. 4.8 before and after change in capacitance. The pulsed outputs of the final inverter stage (V_{inv}) are shown in Fig. 4.11.
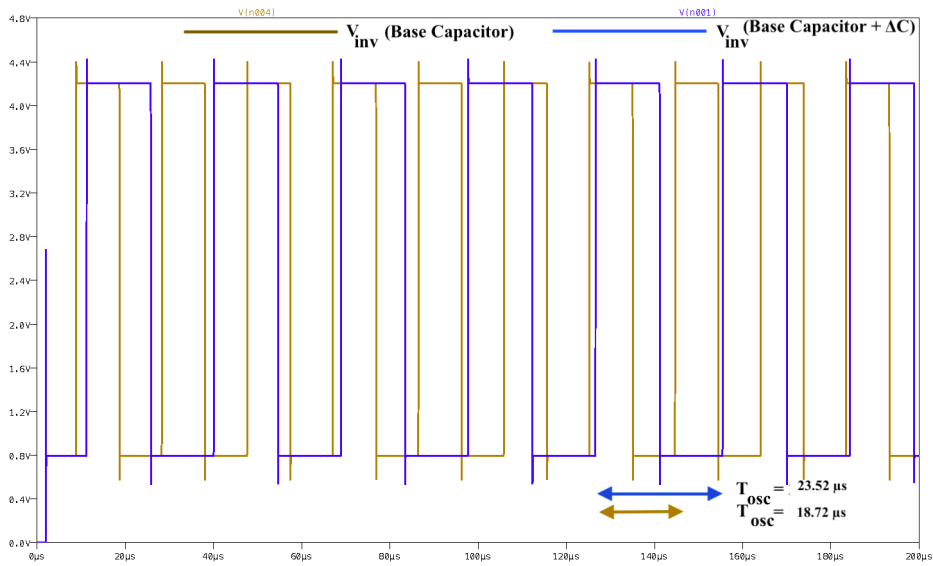
Figure 4.11: Change in oscillation period due to change in capacitance of the sensors in SPICE.

The example mentioned before is a generic example. However, the same oscillator has been used for extracting ΔC of the order of 0.12 fF [87]. The reason for achieving such a high sensitivity with the same circuit is the frequency averaging over a low acquisition rate 3.5 Hz along with the aid of frequency estimation techniques [88].

4.5. CONCLUSION

In this chapter the preliminary results of the electrical characterization of the sensors is provided. Inspired by concepts pertaining to Metal-Insulator-Semiconductor (MIS) devices, a lumped circuit representation of the sensors on PDMS and Si is derived which aids in extracting the operation frequency of the sensors. The measured capacitive values are in excellent agreement with the simulated results and are stable up-to the maximum limits of voltage and frequency available on the LCR meter which are $20V_{rms}$ and 1 MHz respectively. The co-planar capacitive measurements are performed in a floating setup which enable measurements at higher frequencies since the effects of parasitic components are minimized. Via the deposition of a thicker layer of PDMS as well as sensors, the measurement accuracy can be further improved and stabilized. The base capacitance of the sensors increases on encapsulation which is beneficial once they have been integrated with the EHT platform. As the final step of the first level assessment of the sensors, a literature-inspired relaxation oscillator circuit is proposed with simulations carried out in SPICE to present the proof-of-concept of a potential read-out technique.

5

CONCLUSION AND FUTURE OUTLOOK

5.1. CONCLUSION

In this thesis the first level assessment of the first completely integrated sensor for measurement of contractile forces generated by cardiac tissue in miniaturized Engineered Heart Tissue (EHT) platforms was carried out. Prior to fabrication, an in-depth analysis of the mechanical response of the micropillar platform was carried out and coupled with sensing modalities comprising of piezoelectric, piezoresistive and capacitive techniques.

Spiral capacitive sensors were chosen for further analysis on account of their high sensitivity. Inspired by co-planar wave-guides, the sensors exploit variations in co-planar fields emanating and terminating on the capacitor plates due to warping of the substrate to which the micropillars are attached. They are designed in such a manner so as to provide seamless integration with the platform developed at ECTM and fabricated at EKL, TU Delft. Additional multiphysics studies were performed on the integrated sensors and four variations of the spiral sensors with different metallization ratios were designed for the photo-mask.

The designed sensors were fabricated on PDMS without the aid of additional layers, using plasma etching techniques and encapsulated in two layers of PDMS whilst staying intact. Simultaneously, the steps towards the fabrication of micropillars were also carried out. Combined with the process flow of the encapsulated spiral sensors, we are one step closer to developing an on-chip sensor capable of recording forces generated by cardiac tissue to an electrical output. This output can be acquired and utilised for continuous monitoring of engineered heart tissue.

The patterned sensors were electrically characterized by on-wafer probing. A lumped

circuit model is derived and utilised to explore the presence of parasitics within the system. The capacitive measurements were in excellent agreement with the simulated results. The sensors exhibited a stable base-line response up-to 1 MHz input frequency and 20 V_{rms} input voltage, the maximum limits of the measurement instrumentation. A differential read-out circuit was simulated in SPICE, successfully completing the first level assessment of a novel heart-on-chip integrated sensor suitable for point-of-care testing and diagnosis.

5.2. FUTURE OUTLOOK

Future research and development directions based on this thesis are listed as follows.

- Completion of the process flow of the integrated sensors encapsulated in the EHT platform. This is done via combining the fabrication of the sensors encapsulated in PDMS with the steps carried out for the development of the EHT platform as shown previously in Fig. 3.6. The wafer can be diced along with wire-bonding to an external PCB for on-chip measurements.

- System level integration of the sensors with the read-out circuitry can be performed as shown in Fig. 21321. Each chip consists of two pillars of which symmetric outputs are connected in parallel and differential read-out is achieved via the differential oscillator read-out circuit. The signal is then acquired and processed externally via signal processing algorithms. In order to reduce the effects of electromagnetic interference, shielding can be achieved by placing the circuit inside aluminium container as shown in Fig. 5.1.
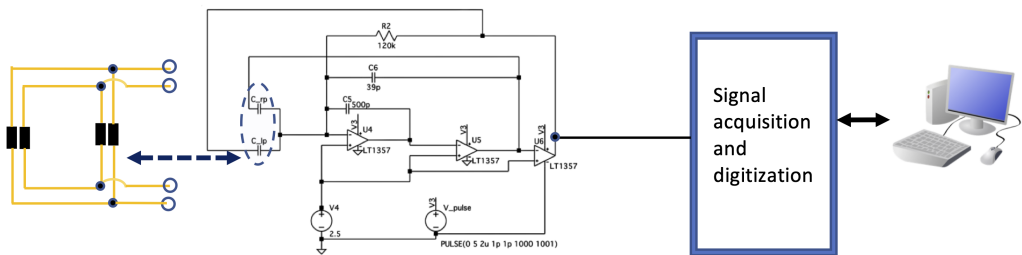
Figure 5.1: Proposed read-out of differential capacitive sensors integrated with cardiac tissue and the EHT platform [sensors are represented by back boxes with PCB connections shown by yellow traces].
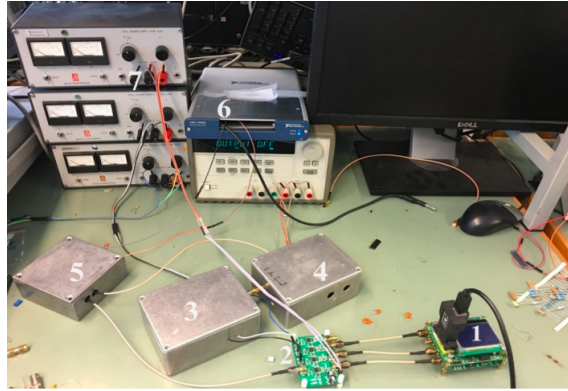
Figure 5.2: Placement of capacitive sensors within Aluminium boxes (3-5) for electromagnetic shielding [89]

- Precise biomechanical characterization of cardiac tissue on the micropillar system after system level integration and comparison with results obtained utilising optical microscopy.

5

REFERENCES

[1] M. Shojaei Baghini, *"Literature Review and Thesis Introductory Report: Microfabricated Systems for Contractile Measurements of Engineered Heart Tissue"*, Feb. 2020.

[2] X. Ren, D. Levin, and F. Lin, "Cell migration research based on organ-on-chip-related approaches," *Micromachines*, vol. 8, no. 11. MDPI AG, 31-Oct-2017.

[3] C. A. Umscheid, D. J. Margolis, and C. E. Grossman, "Key concepts of clinical trials: A narrative review," *Postgraduate Medicine*, vol. 123, no. 5. NIH Public Access, pp. 194–204, Sep-2011.

[4] K. Duval et al., "Modeling physiological events in 2D vs. 3D cell culture," *Physiology*, vol. 32, no. 4. American Physiological Society, pp. 266–277, 14-Jun-2017.

[5] R. Edmondson, J. J. Broglie, A. F. Adcock, and L. Yang, "Three-dimensional cell culture systems and their applications in drug discovery and cell-based biosensors," *Assay and Drug Development Technologies*, vol. 12, no. 4. Mary Ann Liebert Inc., pp. 207–218, 01-May-2014.

[6] C. Y. Chan et al., "Accelerating drug discovery via organs-on-chips," *Lab Chip*, vol. 13, no. 24, pp. 4697–4710, Dec. 2013.

[7] S. N. Bhatia and D. E. Ingber, "Microfluidic organs-on-chips," *Nature Biotechnology*, vol. 32, no. 8. Nature Publishing Group, pp. 760–772, 05-Aug-2014.

[8] D. Huh, G. A. Hamilton, and D. E. Ingber, "From 3D cell culture to organs-on-chips", *Trends in Cell Biology*, vol. 21, no. 12. Elsevier Current Trends, pp. 745–754, 01-Dec-2011.

[9] M. Zhang, C. Xu, L. Jiang, and J. Qin, "A 3D human lung-on-a-chip model for nanotoxicity testing," *Toxicol. Res. (Camb)*., vol. 7, no. 6, pp. 1048–1060, 2018.

[10] L. Si et al., "Human organs-on-chips as tools for repurposing approved drugs as potential influenza and COVID19 therapeutics in viral pandemics," *bioRxiv*, p. 2020.04.13.039917, Apr. 2020.

[11] J. Deng et al., "Engineered liver-on-a-chip platform to mimic liver functions and its biomedical applications: A review," *Micromachines*, vol. 10, no. 10. MDPI AG, 01-Oct-2019.

[12] S. Y. Lee and J. H. Sung, "Gut–liver on a chip toward an in vitro model of hepatic steatosis," *Biotechnol. Bioeng.*, vol. 115, no. 11, pp. 2817–2827, Nov. 2018.

[13] L. Yin et al., "Efficient Drug Screening and Nephrotoxicity Assessment on Co-culture Microfluidic Kidney Chip," *Sci. Rep.*, vol. 10, no. 1, pp. 1–11, Dec. 2020.

[14] M. J. Wilmer, C. P. Ng, H. L. Lanz, P. Vulto, L. Suter-Dick, and R. Masereeuw, "Kidney-on-a-Chip Technology for Drug-Induced Nephrotoxicity Screening," *Trends in Biotechnology*, vol. 34, no. 2. Elsevier Ltd, pp. 156–170, 01-Feb-2016.

5

[15] G. Sriram et al., "Full-thickness human skin-on-chip with enhanced epidermal morphogenesis and barrier function," *Mater. Today*, vol. 21, no. 4, pp. 326–340, May 2018.

[16] B. Lukács et al., "Skin-on-a-chip device for ex vivo monitoring of transdermal delivery of drugs—design, fabrication, and testing," *Pharmaceutics*, vol. 11, no. 9, Sep. 2019.

[17] S. Bang, S. Jeong, N. Choi, and H. N. Kim, "Brain-on-a-chip: A history of development and future perspective," *Biomicrofluidics*, vol. 13, no. 5. American Institute of Physics Inc., p. 051301, 01-Sep-2019.

[18] A. P. Haring and B. N. Johnson, "Brain-on-a-chip systems for modeling disease pathogenesis," in *Organ-on-a-chip*, Elsevier, 2020, pp. 215–232.

[19] A. Agarwal, J. A. Goss, A. Cho, M. L. McCain, and K. K. Parker, "Microfluidic heart on a chip for higher throughput pharmacological studies," *Lab Chip*, vol. 13, no. 18, pp. 3599–3608, Sep. 2013.

[20] Y. Zhao et al., "Towards chamber specific heart-on-a-chip for drug testing applications," *Adv. Drug Deliv. Rev.*, 2020.

[21] E. Gencturk, S. Mutlu, and K. O. Ulgen, "Advances in microfluidic devices made from thermoplastics used in cell biology and analyses," *Biomicrofluidics*, vol. 11, no. 5, Sep. 2017.

[22] W. F. Quirós-Solano et al., "Microfabricated tuneable and transferable porous PDMS membranes for Organs-on-Chips," *Sci. Rep.*, vol. 8, no. 1, Dec. 2018.

[23] A. O. Stucki et al., "Lab on a Chip A lung-on-a-chip array with an integrated bio-inspired respiration mechanism", *Lab Chip*, vol. 15, p. 1302, 2015.

[24] H. Lee, D. S. Kim, S. K. Ha, I. Choi, J. M. Lee, and J. H. Sung, "A pumpless multi-organ-on-a-chip (MOC) combined with a pharmacokinetic–pharmacodynamic (PK–PD) model", *Biotechnol. Bioeng.*, vol. 114, no. 2, pp. 432–443, Feb. 2017.

[25] K.-J. Jang et al., "Human kidney proximal tubule-on-a-chip for drug transport andnephrotoxicity assessment Human kidney proximal tubule-on-a-chip for drug transportand nephrotoxicity assessment", *Integr. Biol*, vol. 5, no. 9, p. 1119, 2013.

[26] F. Qian et al., "Simultaneous electrical recording of cardiac electrophysiology and contrac-tion on chip", *Lab Chip*, vol. 17, no. 10, pp. 1732–1739, 2017.

[27] "Easy and Reliable In Vitro BBB-on-a-Chip|Mimetas." [Online]. Available: https://mimetas.com/article/easy-and-reliable-vitro-bbb-chip. [Accessed: 12-Aug-2020]

[28] E. Ergir, B. Bachmann, H. Redl, G. Forte, and P. Ertl, "Small Force, Big Impact: Next Generation Organ-on-a-Chip Systems Incorporating Biomechanical Cues," *Front. Physiol.*, vol. 9, no. OCT, p. 1417, Oct. 2018.

[29] "Organs on chip review - Elveflow." [Online]. Available: https://www.elveflow.com/microfluidic-reviews/organs-on-chip-3d-cell-culture/organs-chip-review/. [Accessed: 13-Aug-2020].

[30] N. Azizipour, R. Avazpour, D. H. Rosenzweig, M. Sawan, and A. Ajji, "Evolution of biochip technology: A review from lab-on-a-chip to organ-on-a-chip," *Micromachines*, vol. 11, no. 6, pp. 1–15, Jun. 2020.

[31] R. R. Besser, M. Ishahak, V. Mayo, D. Carbonero, I. Claure, and A. Agarwal, "Engineered microenvironments for maturation of stem cell derived cardiac myocytes", *Theranostics*, vol. 8, no. 1, pp. 124–140, Jan. 2018.

[32] V. Talman and R. Kivelä, "Cardiomyocyte—Endothelial Cell Interactions in Cardiac Remodeling and Regeneration," *Frontiers in Cardiovascular Medicine*, vol. 5. Frontiers Media S.A., p. 101, 26-Jul-2018.

[33] W. L. Stoppel, D. L. Kaplan, and L. D. Black, "Electrical and mechanical stimulation of cardiac cells and tissue constructs," *Advanced Drug Delivery Reviews*, vol. 96. Elsevier B.V., pp. 135–155, 15-Jan-2016.

[34] S. Sugiura et al., "Measurement of Force Developed by a Single Cardiac Myocyte Using Novel Carbon Fibers," *Springer*, Boston, MA, 2003, pp. 381–387.

[35] C. Zuppinger, "3D Cardiac Cell Culture: A Critical Review of Current Technologies andApplications",*Frontiers in Cardiovascular Medicine*, vol. 6. Frontiers Media S.A., p. 87,26-Jun-2019.

[36] R. J. Mills et al., "Functional screening in human cardiac organoids reveals a metabolic mechanism for cardiomyocyte cell cycle arrest," *Proc. Natl. Acad. Sci. U. S. A.*, vol. 114, no. 40, pp. E8372–E8381, Oct. 2017.

[37] M. Dostanic et al., "A Miniaturized EHT Platform for Accurate Measurements of Tissue Contractile Properties," *J. Microelectromechanical Syst.*, pp. 1–7, 2020.

[38] R. Veeraraghavan, R. G. Gourdie, and S. Poelzing, "Mechanisms of cardiac conduction: A history of revisions," *American Journal of Physiology - Heart and Circulatory Physiology*, vol. 306, no. 5. American Physiological Society, p. H619, 01-Mar-2014.

[39] J. A. Mulligan, X. Feng, and S. G. Adie, "Quantitative reconstruction of time-varying 3D cell forces with traction force optical coherence microscopy," *Sci. Rep.*, vol. 9, no. 1, Dec. 2019.

[40] K. S. Bielawski, A. Leonard, S. Bhandari, C. E. Murry, and N. J. Sniadecki, "Real-Time Force and Frequency Analysis of Engineered Human Heart Tissue Derived from Induced Pluripotent Stem Cells Using Magnetic Sensing",*Tissue Eng. - Part C Methods*, vol. 22,no. 10, pp. 932–940, Oct. 2016

[41] K. S. Rao et al., "Design and sensitivity analysis of capacitive MEMS pressure sensor for blood pressure measurement," *Microsyst. Technol.*, vol. 26, no. 8, pp. 2371–2379, Aug. 2020.

5

[42] R. Zeiser, T. Fellner, and J. Wilde, "Capacitive strain gauges on flexible polymer substrates for wireless, intelligent systems," *J. Sensors Sens. Syst.*, vol. 3, no. 1, pp. 77–86, Apr. 2014.

[43] "Piezoelectric Force Transducer: 5 Rules for Installation an | HBM." [Online]. Available: https://www.hbm.com/en/3212/piezoelectric-force-transducer-installation-and-mounting/. [Accessed: 14-Aug-2020].

[44] C. Dagdeviren et al., "Recent progress in flexible and stretchable piezoelectric devices for mechanical energy harvesting, sensing and actuation," *Extreme Mechanics Letters*, vol. 9. Elsevier Ltd, pp. 269–281, 01-Dec-2016.

[45] H. Jin et al., "Stretchable Dual-Capacitor Multi-Sensor for Touch-Curvature-Pressure-Strain Sensing," *Sci. Rep.*, vol. 7, no. 1, pp. 1–8, Dec. 2017.

[46] S. Chandra and S. Chandra, "Wearable sensors for physiological parameters measurement: physics, characteristics, design and applications," *Wearable Sensors:Applications, design and implementation*, IOP Publishing, 2017.

[47] A. C. C. Van Spreeuwel et al., "The influence of matrix (an)isotropy on cardiomyocyte contraction in engineered cardiac microtissues," *Integr. Biol. (United Kingdom)*, vol. 6, no. 4, pp. 422–429, Apr. 2014.

[48] A. Kajzar, C. M. Cesa, N. Kirchgeßner, B. Hoffmann, and R. Merkel, "Toward physiological conditions for cell analyses: Forces of heart muscle cells suspended between elastic micropillars," *Biophys. J.*, vol. 94, no. 5, pp. 1854–1866, Mar. 2008.

[49] I. Schoen, W. Hu, E. Klotzsch, and V. Vogel, "Probing cellular traction forces by micropillar arrays: Contribution of substrate warping to pillar deflection," *Nano Lett.*, vol. 10, no. 5, pp. 1823–1830, May 2010.

[50] Comsol, "The Structural Mechanics Module User's Guide," 2018.

[51] K. Takizawa, T. E. Tezduyar, and T. Sasaki, "Isogeometric hyperelastic shell analysis with out-of-plane deformation mapping," *Comput. Mech.*, vol. 63, no. 4, pp. 681–700, Apr. 2019.

[52] K. H. Baumgärtel, D. Zöllner, and K.-L. Krieger, "Classification and Simulation Method for Piezoelectric PVDF Sensors," *Procedia Technol.*, vol. 26, pp. 491–498, Jan. 2016.

[53] "Theory: How to Calculate Piezoelectric Material Properties from a Material Datasheet | OnScale." [Online]. Available:https://bit.ly/2Y2pulc. [Accessed: 14-Aug-2020].

[54] "How to Model Piezoelectric Devices as Both Transmitters and Receivers | COMSOL Blog." [Online]. Available:https://bit.ly/2E2BZ9e. [Accessed: 14-Aug-2020].

[55] A. Jain, K. J. Prashanth, A. K. Sharma, A. Jain, and R. P.n, "Dielectric and piezoelectric properties of PVDF/PZT composites: A review," *Polym. Eng. Sci.*, vol. 55, no. 7, pp. 1589–1616, Jul. 2015.

5

[56] S. Yang and N. Lu, "Gauge factor and stretchability of silicon-on-polymer strain gauges," *Sensors (Switzerland)*, vol. 13, no. 7, pp. 8577–8594, Jul. 2013.

[57] M. C. Ben Romdhane, H. Mrad, F. Erchiqui, and R. Ben Mrad, "Thermomechanical Study and Fracture Properties of Silicon Wafer under Effect of Crystal Orientation," in *IOP Conference Series: Materials Science and Engineering*, 2019, vol. 521, no. 1.

[58] Y. Kim, Y. Kim, C. Lee, and S. Kwon, "Thin polysilicon gauge for strain measurement of structural elements," *IEEE Sens. J.*, vol. 10, no. 8, pp. 1320–1327, 2010

[59] S. M. Won et al., "Piezoresistive strain sensors and multiplexed arrays using assemblies of single-crystalline silicon nanoribbons on plastic substrates," *IEEE Trans. Electron Devices*, vol. 58, no. 11, pp. 4074–4078, Nov. 2011.

[60] M. Maroufi, N. Nikooienejad, M. Mahdavi, and S. O. Reza Moheimani, "SOI-MEMS Bulk Piezoresistive Displacement Sensor: A Comparative Study of Readout Circuits," *J. Microelectromechanical Syst.*, vol. 29, no. 1, pp. 43–53, Feb. 2020.

[61] T. Han et al., "Multifunctional Flexible Sensor Based on Laser-Induced Graphene", *Sensors*, vol. 19, no. 16, p. 3477, Aug. 2019.

[62] A. D'Alessandro, S. Scudero, and G. Vitale, "A Review of the Capacitive MEMS for Seismology," *Sensors*, vol. 19, no. 14, p. 3093, Jul. 2019.

[63] N. Gaio, "Organ-on-Silicon," 2019.

[64] D. P. Da Silva and S. F. Pichorim, "Modeling of open square bifilar planar spiral coils," *J. Microwaves, Optoelectron. Electromagn. Appl.*, vol. 17, no. 3, pp. 319–339, 2018.

[65] Y. Zhao, Y. Cao, W. Hong, M. K. Wadee, and X. Q. Feng, "Towards a quantitative understanding of period-doubling wrinkling patterns occurring in film/substrate bilayer systems," *Proc. R. Soc. A Math. Phys. Eng. Sci.*, vol. 471, no. 2173, Jan. 2015.

[66] W. R. Lee, C. Im, H. Y. Park, J. M. Seo, and J. M. Kim, "Fabrication of convex PDMS-parylene microstructures for conformal contact of planar micro-electrode array," *Polymers (Basel).*, vol. 11, no. 9, 2019.

[67] S. Lee, Y. Y. Kim, and Y. Cho, "A comparative study on the elastic characteristics of an aluminum thin-film using laser optical measurement techniques," *Coatings*, vol. 7, no. 9, Sep. 2017.

[68] Y. Zhou, U. Erb, K. T. Aust, and G. Palumbo, "Young's modulus in nanostructured metals," *Zeitschrift fuer Met. Res. Adv. Tech.*, vol. 94, no. 10, pp. 1157–1161, 2003.

[69] J. R. Sambles, K. C. Elsom, and G. Sharp-Dent, "The effect of sample thickness on the resistivity of aluminium," *J. Phys. F Met. Phys.*, vol. 11, no. 5, pp. 1075–1092, 1981.

[70] C. Exley, "Human exposure to aluminium," *Environmental Sciences: Processes and Impacts*, vol. 15, no. 10. pp. 1807–1816, Oct-2013.

5

[71] D. Wu, H. Xie, and Y. Yin, "Fracture behavior of thin aluminum films on soft substrate."

[72] M. A. Karami and A. Afzali-Kusha, "Exponentially tapering ground wires for elmore delay reduction in on chip interconnects," in *Proceedings of the International Conference on Microelectronics, ICM*, 2006, pp. 99–102.

[73] M. Dabaghi et al., "An ultra-thin, all PDMS-based microfluidic lung assist device with high oxygenation capacity," *Biomicrofluidics*, vol. 13, no. 3, p. 034116, May 2019.

[74] A. D. Mazzeo and D. E. Hardt, "Microfluidic Components With PDMS," *J. Micro Nano-Manufacturing*, vol. 1, no. 2, p. 21001, 2013.

[75] S. Béfahy, S. Yunus, V. Burguet, J.-S. Heine, M. Troosters, and P. Bertrand, "Stretchable Gold Tracks on Flat Polydimethylsiloxane (PDMS) Rubber Substrate," *J. Adhes.*, vol. 84, no. 3, pp. 231–239, Apr. 2008.

[76] W. E. Frank, "Approaches for patterning of aluminum," 1997.

[77] S. Majee, D. Barshilia, S. Kumar, P. Mishra, and J. Akhtar, "Signature of growth deposition technique on the properties of PECVD and thermal SiO2," in *AIP Conference Proceedings*, 2018, vol. 1989.

[78] J. Tang et al., "Highly Stretchable Electrodes on Wrinkled Polydimethylsiloxane Substrates," *Sci. Rep.*, vol. 5, no. 1, p. 16527, Nov. 2015.

[79] S. J. Hwang et al., "Dry etching of polydimethylsiloxane using microwave plasma," *J. Micromechanics Microengineering*, vol. 19, no. 9, 2009.

[80] G. Bhatt, K. Patel, P. Suryavanshi, C. Panchal, "Optimization of Ultrasonic and Thermosonic Wire-Bonding Parameters on Au/Ni Plated PCB Substrate", at *National Laser Symposium (NLS-24) Conference*, Dec. 2015.

[81] T. Dow Chemical Company, "SYLGARDTM 184 Silicone Elastomer FEATURES BENEFITS," 2017.

[82] "Agilent 4284A/4285A Precision LCR Meter Family." [https://bit.ly/2E47pMu] Accessed: 16-Aug-2020]

[83] "Inductor Sizing Equation | Useful Equations And Conversion Factors | Electronics Textbook." [Online]. Available: https://www.allaboutcircuits.com/textbook/reference/chpt-1/inductor-sizing-equation/. [Accessed: 16-Aug-2020].

[84] R. A. Brookhuis, R. J. Wiegerink, T. S. J. Lammerink, and G. J. M. Krijnen, "Three-axial force sensor with capacitive read-out using a differential relaxation oscillator," in *Proceedings of IEEE Sensors*, 2013.

5

[85] J. Lee, A. George, and M. Je, "A 1.4V 10.5MHz swing-boosted differential relaxation oscillator with 162.1dBc/Hz FOM and 9.86psrms period jitter in 0.18μm CMOS," in *Digest of Technical Papers - IEEE International Solid-State Circuits Conference*, 2016, vol. 59, pp. 106–108.

[86] H. Kim, I.-H. Rho, and W.-S. Chung, "High-speed interface circuit for differential capacitance transducers," *IEICE Electron. Express*, vol. 8, no. 2, pp. 96–102.

[87] R. A. Brookhuis, T. S. J. Lammerink, and R. J. Wiegerink, "Differential capacitive sensing circuit for a multi-electrode capacitive force sensor," *Sensors Actuators, A Phys.*, vol. 234, pp. 168–179, Oct. 2015.

[88] J. Song, Q. An, and S. Liu, "A high-resolution time-to-digital converter implemented in field-programmable-gate-arrays," *IEEE Trans. Nucl. Sci.*, vol. 53, no. 1, pp. 236–241, Feb. 2006.

[89] D. Lin, "An atto-Farad resolution closed loop impedance measurement bridge for capacitive sensors," 2018.

PEIZORESISTIVE AND CAPACITIVE SENSOR MATERIALS

Table 3.1: Comparison table of commonly used piezoresistive materials

Material	Gauge Factor	Film Thickness	Resistivity	Deposition technique	Ref.	Biocompatibility (via testing with mesenchymal cells)
Metal						
TiN	6.05 ± 0.053	307-314 nm	110-1230 $\mu\Omega$cm	Magnetron sputtering	[12]	Positive [25]
Ti	3.78	100 nm	132 $\mu\Omega$cm	Electron beam evaporation	[13]	Positive (Ti enhances stem cell proliferation and differentiation) [26]
Au	4.9-6.6 (as temperature varied from 25 to 55 degrees) Sensitivity: 0.0086 Ω/ppm	400 nm	-	Magnetron sputtering	[14]	Positive [27]
Pt	5.933	500 nm	-	Magnetron sputtering	[15]	Positive (Pt and its composites are also widely used in chemotherapeutics) [28]
Ni-Cr alloy	1.75	35 nm	-	Magnetron sputtering	[16]	Unknown, however nichrome is commonly used in implantable electrodes [29]
Organic						
Amorphous Carbon	67-69	500 nm	5e4 $\mu\Omega$cm	Magnetron Sputtering	[17]	Positive [30]
Hydrogenated Amorphous Carbon	40-90	500 nm	1e5 $\mu\Omega$cm	PECVD (Hydrocarbon rich vapour)	[18]	Positive [31]
Graphene	61.5	2500 nm	-	Drop casting of Graphene Oxide followed by laser induced reduction	[19]	Positive [32]
Polymer						
PEDOT:PSS	0.48 ± 0.07	150 nm	Sheet resistance: 1500 ohm/$\square$	Spin coating followed by lithographic patterning	[20]	Positive [33]
PDMS-Carbon nanotube composite	2.7	5e4 nm	-	Spin coating of composite solution followed by stamping	[21]	Positive [34]

Material	Gauge Factor	Film Thickness	Resistivity	Deposition technique	Ref.	Biocompatibility (via testing with mesenchymal cells)
Semiconductor						
p-type monocrystalline Silicon	200	-	-	-	[22]	Positive [35] (Biocompatibility can be further enhanced by surface functionalization)
n-type monocrystalline Silicon	-125	-	-	-	[22]	Positive [35] (Biocompatibility can be further enhanced by surface functionalization)
p-type polycrystalline Silicon	24 to 31 (longitudinal, highly dependent on grain size)	100 nm	$N_d=10^{19}-10^{20}$ cm^{-3} (ρ=5e5-1e4 $\mu\Omega$cm)	LPCVD followed by ion implantation	[23]	Positive [35] (Biocompatibility can be further enhanced by surface functionalization)
n-type polycrystalline Silicon	-15 to -24 (longitudinal, highly dependent on grain size)	100 nm	$N_d=10^{19}-10^{20}$ cm^{-3} (ρ=5e5-6e3 $\mu\Omega$cm)	LPCVD followed by ion implantation	[23]	Positive [35] (Biocompatibility can be further enhanced by surface functionalization)
Nitrogen doped Amorphous SiC	49	550 nm	17e4 $\mu\Omega$cm	PECVD	[24]	Positive [35] (Biocompatibility can be further enhanced by surface functionalization)

Table 3.2: High sensitivity capacitive sensors (Sensitivity is expressed as the change in the capacitance per parameter

Electrode Material	Baseline Capacitance	Sensitivity	Electrode Fabrication	Electrode dimensions	Inter-electrode distance	Reference
Cr + Cu (or Au)	47.7 pF	-0.658 pF/% strain	Photolithography followed by lift off	Width = 300 nm Length = 45 μm Thickness = 30 nm (Cr) + 350 nm (Cu or Au)	15 μm	[25]
Au	55 fF	-	EBL followed by lift off	Width = 200 nm Length = 50 μm Thickness = 50 nm	500 nm	[26]
Liquid-phase Galinstan	9.6 pF	0.02 pF/% strain	Lithography followed by injection of Galinstan in channels	Length = 135 mm Thickness = 100 μm	100 μm	[27]
Conductive fiber (Ag)	17 pF	0.136 pF/%strain	Casting followed by laser cutting	Length = 65 mm Thickness = 0.45 mm	0.35 mm	[28]
Conductive PDMS (with CNT; cPDMS)	16.15 pF	0.02pF/$\mu\epsilon$	Trench deposition of cPDMS followed by peeling. A second layer of PDMS is cured on top.	Width = 50 μm Length = 4 mm Thickness = 65 μm	30 μm	[29]

APPENDIX B

SURFACE VERTICAL DISPLACEMENT OF SOFT SUBSTRATE

Closed form of substrate warping via its vertical displacement on the application of a pillar boundary force equal to 500 μN, represented symbolically by Eq. 2.8.

$$
\begin{aligned}
&\Big(1906734396158577^*(y/956-1/4)^*\big((x/191+1/2)^{\wedge}2+(y/478- \\
&1/2)^{\wedge}2\big)^{\wedge}(1/2)\Big)/295147905179352825856 - \Big(1906734396158577^*(y/956-1/4)^*((x/191- \\
&1/2)^{\wedge}2+(y/478-1/2)^{\wedge}2)^{\wedge}(1/2)/295147905179352825856 + \big(1906734396158577^*(y/956+ \\
&1/4)^*\big((x/191-1/2)^{\wedge}2+(y/478+1/2)^{\wedge}2\big)^{\wedge}(1/2)\big)/295147905179352825856 - \\
&\Big(1906734396158577^*(y/956+1/4)^*\big((x/191+1/2)^{\wedge}2+(y/478+ \\
&1/2)^{\wedge}2\big)^{\wedge}(1/2)\Big)/295147905179352825856 - \Big(1906734396158577^* \log(y/478 + ((x/191- \\
&1/2)^{\wedge}2+(y/478-1/2)^{\wedge}2)^{\wedge}(1/2)-1/2\Big)^*(x/191-1/2)^{\wedge}2\big)/590295810358705651712 + \\
&\Big(1906734396158577^* \log\big(y/478 + ((x/191-1/2)^{\wedge}2+(y/478+1/2)^{\wedge}2)^{\wedge}(1/2)+1/2\Big)^*(x/191- \\
&1/2)^{\wedge}2\big)/590295810358705651712 + \big(1906734396158577^* \log\big(y/478 + ((x/191+1/2)^{\wedge}2+ \\
&(y/478-1/2)^{\wedge}2)^{\wedge}(1/2)-1/2\Big)^*(x/191+1/2)^{\wedge}2\big)/590295810358705651712 \\[6pt]
&\Big(1906734396158577^* \log\big(y/478 + ((x/191+1/2)^{\wedge}2+(y/478+1/2)^{\wedge}2)^{\wedge}(1/2)+1/2\Big)^*(x/191+ \\
&1/2)^{\wedge}2\big)/590295810358705651712 + \big(1906734396158577^* x^* \big(\log\big(x/191 + ((x/191-1/2)^{\wedge}2+ \\
&(y/478-1/2)^{\wedge}2)^{\wedge}(1/2)-1/2\Big)^*(y/478-1/2) - \log\big(x/191 + ((x/191+1/2)^{\wedge}2+(y/478- \\
&1/2)^{\wedge}2)^{\wedge}(1/2)+1/2\Big)^*(y/478-1/2) + \log\big(y/478 + ((x/191-1/2)^{\wedge}2+(y/478-1/2)^{\wedge}2)^{\wedge}(1/2)- \\
&1/2)^*(x/191-1/2) - \log\big(y/478 + ((x/191+1/2)^{\wedge}2+(y/478-1/2)^{\wedge}2)^{\wedge}(1/2)-1/2\Big)^*(x/191+ \\
&1/2)+1)/56373249889256389738496 - (1906734396158577 * x * (\log(x/191 + ((x/191)- \\
&1/2)^{\wedge}2+(y/478+1/2)^{\wedge}2)^{\wedge}(1/2)-1/2\Big)^*(y/478+1/2) - \log\big(x/191 + ((x/191+1/2)^{\wedge}2+(y/478+ \\
&1/2)^{\wedge}2)^{\wedge}(1/2)+1/2\Big)^*(y/478+1/2) + \log\big(y/478 + ((x/191-1/2)^{\wedge}2+(y/478+1/2)^{\wedge}2)^{\wedge}(1/2)+ \\
&1/2)^*(x/191-1/2) - \log\big(y/478 + ((x/191+1/2)^{\wedge}2+(y/478+1/2)^{\wedge}2)^{\wedge}(1/2)+1/2\Big)^*(x/191+ \\
&1/2)+1)//56373249889256389738496
\end{aligned}
$$

$$\tag{1}$$

BASE CAPACITANCE VS GAP AND WIDTH OF SPIRAL SENSOR ELECTRODES

Fig. 3a and 3b illustrate the variation of base capacitance as a function of gap and width for a constant path length of 6310 μm. The values increase along the arrow with the tip representing the maximum. The maximum and minimum values of both the parameters have been set at $5\mu m$ and $50\mu m$, respectively.
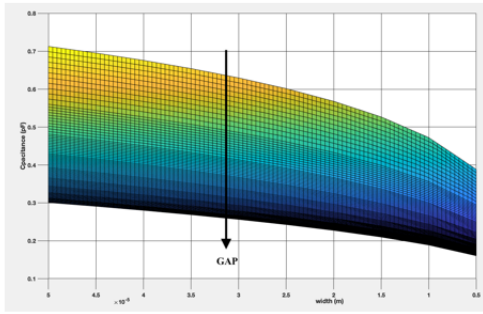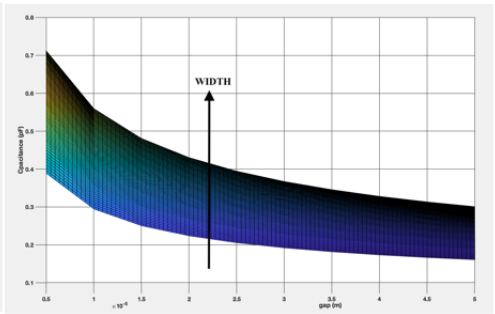

Figure 3: Variation of spiral sensor capacitance with A) Increasing gap B) Increasing width

APPENDIX D

SIMULATED CAPACITANCE VS MESHING CHARACTERISTICS

The simulated base capacitance in COMSOL is highly dependent on the minimum element size of the meshed surrounding air domain. As the minimum element size is reduced, computation time increases. For a refined mesh with minimum element size equal to 4.5 μm the computation time for the electrostatics physics is 4 hours. Once coupled with the moving mesh and Shell interfaces, an out-of-memory error occurs. Hence minimum mesh elements size has been kept at 12 μm for all simulations. To improve accuracy, a computer with a higher RAM can be used (currently used RAM = 8 GB) or simulations can be carried out on the cloud. Table 1 shows the simulated base capacitance with respect to elements size of sensor D placed on the surface of a 2 μm thick PDMS layer.

Table 1: Base capacitance (sensor D) vs minimum mesh element size of surrounding air domain

Minimum mesh element size	Base Capacitance (pF)
54 μm	0.1852
30 μm	0.1443
12 μm	0.1123
4.5 μm	0.107
0.6 μm	0.102

In order to simulate thin film sensors as domains, a triangular mesh must be applied to the boundary surface and swept along the domain. An advantage of modelling thin film sensors as boundaries in the Shell interface is the that the surface mesh is generated considering the points in the tetrahedral surrounding air domain, increasing the efficiency of modelling while not affecting the simulation time. This is shown in Fig. 4a and 4b.

A)

B)
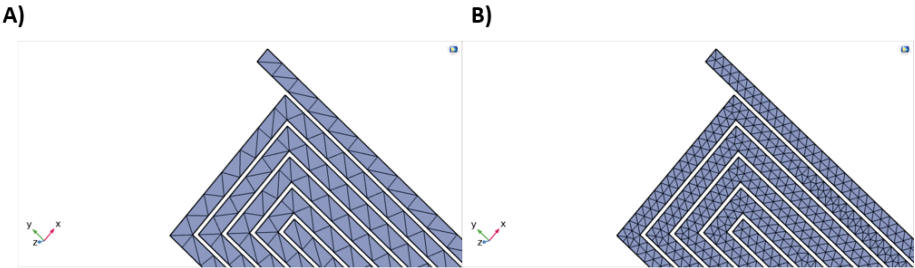
Figure 4: Meshing of capacitor plates A) Surface traingular mesh (Size: "Extremely Fine") B) Tetrahedral domain mesh of air extended to metallic plates (Size: "Extremely Fine")

APPENDIX E

QUARTZ AND ALUMINIUM MASKS UTILISED DURING FABRICATION
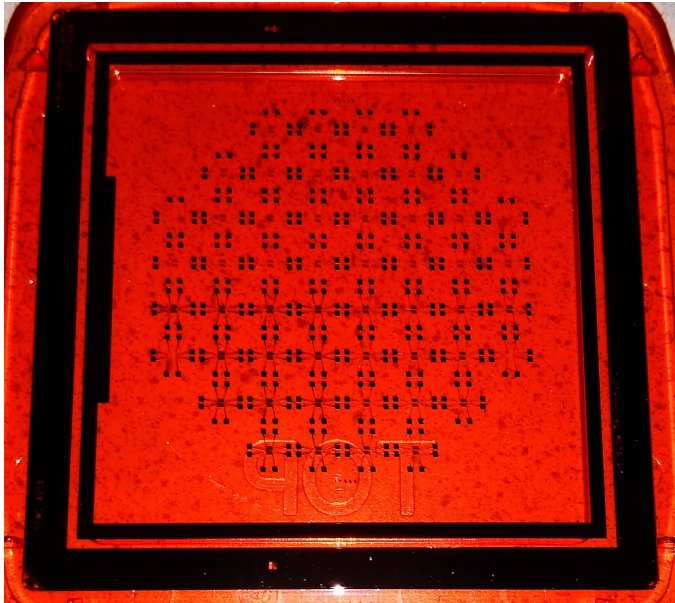
Figure 5: Quartz mask for fabrication of spiral sensors (CP+S+I)

A)

B)

Figure 6: Foil Masks A) Contact Pads (CP) for front-side patterning B) Contact Pads and Wells (CP+W) for back-side patterning

APPENDIX F

FLOWCHART FOR PATTERNING OF SPIRAL SENSORS AND BOSCH ETCHING OF SI

Alignment marks

1. COATING

Use the coater station of the EVG120 system to coat the wafers with photoresist. The process consists of:
- a treatment with HMDS (hexamethyldisilazane) vapor, with nitrogen as a carrier gas
- spin coating of Shipley SPR3012 positive resist, dispensed by a pump
- a soft bake at 95 °C for 90 seconds
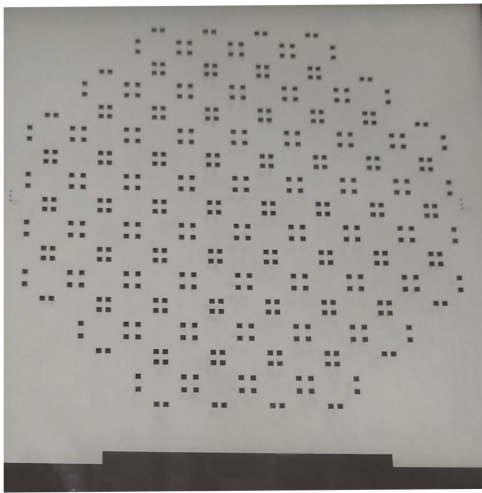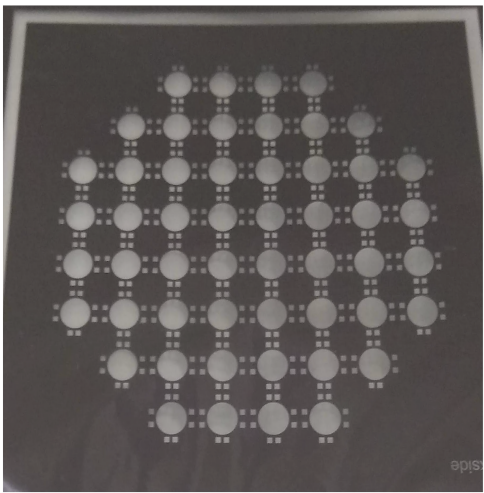- an automatic edge bead removal with a solvent

Always check the relative humidity (48 ± 2 %) in the room before coating, and follow the instructions for this equipment.

Use program **"Co - 3012 – 1.4 – no EBR"**.

2. ALIGNMENT AND EXPOSURE

Processing will be performed on the ASML PAS5500/80 automatic wafer stepper.
Follow the operating instructions from the manual when using this machine.

Expose masks **COMURK**, with job **"ZEFWAM"** and the correct exposure energy 120mJ
This results in alignment markers for the stepper and contact aligner.

3. DEVELOPING

Use the developer station of the EVG120 system to develop the wafers. The process consists of:
- a post-exposure bake at 115 °C for 90 seconds
- developing with Shipley MF322 with a single puddle process
- a hard bake at 100 °C for 90 seconds

Always follow the instructions for this equipment.

Use program **"Dev - SP"**.

4. INSPECTION: Linewidth and overlay

Visually inspect the wafers through a microscope, and check the line width and overlay. No resist residues are allowed

5. PLASMA ETCHING: Alignment markers (URK's) in Silicon

Use the Trikon Ωmega 201 plasma etcher.
Follow the operating instructions from the manual when using this machine.
It is **not** allowed to change the process conditions and times from the etch recipe!

Use sequence **URK_NPD** (with a platen temperature of **20 °C**) to etch 120 nm deep ASM URK's into the Si.

Process conditions from chamber recipe URK_ETCH:						
Step	Gasses & flows	Pressure	Platen RF	ICP RF	Platen temp.	Etch time
1. breakthrough	CF_4/O_2 = 40/20 sccm	5 mTorr	60 W	500 W	20 °C	0'10"
2. bulk etch	Cl_2/HBr = 80/40 sccm	60 mTorr	20 W	500 W	20 °C	0'40"

6. LAYER STRIPPING: Photoresist

Strip resist   Use the Tepla Plasma 300 system to remove the photoresist in an oxygen plasma.
Follow the instructions specified for the Tepla stripper, and use the quartz carrier.
Use **program 1**: 1000 watts power and automatic endpoint detection + 2 min. overetching.

7. CLEANING: HNO_3 99% and 69.5%

Clean   10 minutes in fuming nitric acid at ambient temperature. This will dissolve organic materials.
Use wet bench "HNO_3 99% (Si)" and the carrier with the red dot.
Rinse   Rinse in the Quick Dump Rinser with the standard program until the resistivity is 5 MΩ.
Clean   10 minutes in concentrated nitric acid at 110 °C. This will dissolve metal particles.
Use wet bench "HNO_3 69,5% 110C (Si)" and the carrier with the red dot.
Rinse   Rinse in the Quick Dump Rinser with the standard program until the resistivity is 5 MΩ.
Dry   Use the Semitool "rinser/dryer" with the standard program, and the white carrier with a red dot.

8. COATING (backside)

Use the coater station of the EVG120 system to coat the wafers with photoresist. The process consists of:
- a treatment with HMDS (hexamethyldisilazane) vapor, with nitrogen as a carrier gas
- spin coating of Shipley SPR3012 positive resist, dispensed by a pump
- a soft bake at 95 °C for 90 seconds
- an automatic edge bead removal with a solvent

Always check the relative humidity (48 ± 2 %) in the room before coating, and follow the instructions for this equipment.

Use program **"Co - 3012 – 1.4 – no EBR"**.

9. ALIGNMENT AND EXPOSURE

Processing will be performed on the ASML PAS5500/80 automatic wafer stepper.
Follow the operating instructions from the manual when using this machine.

Expose masks **COMURK**, with job "**ZEFWAM**" and the correct exposure energy 120mJ
This results in alignment markers for the stepper and contact aligner.
Note: Slight misalignment between front and back side masks. Job "**ftbafwam**" can be used if exact alignment is required with caution since it led to patterning of mirrored alignment marks.

10. DEVELOPING

Use the developer station of the EVG120 system to develop the wafers. The process consists of:
  ▪ a post-exposure bake at 115 °C for 90 seconds
  ▪ developing with Shipley MF322 with a single puddle process
  ▪ a hard bake at 100 °C for 90 seconds
Always follow the instructions for this equipment.

Use program "**Dev - SP**".

11. INSPECTION: Linewidth and overlay

Visually inspect the wafers through a microscope, and check the line width and overlay. No resist residues are allowed

12. PLASMA ETCHING: Alignment markers (URK's) in Silicon

Use the Trikon Ωmega 201 plasma etcher.
Follow the operating instructions from the manual when using this machine.
It is **not** allowed to change the process conditions and times from the etch recipe!

Use sequence **URK_NPD** (with a platen temperature of **20 °C**) to etch 120 nm deep ASM URK's into the Si.

Process conditions from chamber recipe URK_ETCH:						
Step	Gasses & flows	Pressure	Platen RF	ICP RF	Platen temp.	Etch time
1. breakthrough	CF_4/O_2 = 40/20 sccm	5 mTorr	60 W	500 W	20 °C	0'10"
2. bulk etch	Cl_2/HBr = 80/40 sccm	60 mTorr	20 W	500 W	20 °C	0'40"

13. LAYER STRIPPING: Photoresist

Strip resist   Use the Tepla Plasma 300 system to remove the photoresist in an oxygen plasma.
Follow the instructions specified for the Tepla stripper, and use the quartz carrier.
Use **program 1**: 1000 watts power and automatic endpoint detection + 2 min. overetching.

Definition of SiO_2 hard mask- pig noses (front)

14. CLEANING: HNO_3 99% and 69.5%

Clean   10 minutes in fuming nitric acid at ambient temperature. This will dissolve organic materials.
Use wet bench "HNO_3 99% (Si)" and the carrier with the red dot.
Rinse   Rinse in the Quick Dump Rinser with the standard program until the resistivity is 5 MΩ.
Clean   10 minutes in concentrated nitric acid at 110 °C. This will dissolve metal particles.
Use wet bench "HNO_3 69,5% 110C (Si)" and the carrier with the red dot.
Rinse   Rinse in the Quick Dump Rinser with the standard program until the resistivity is 5 MΩ.
Dry   Use the Semitool "rinser/dryer" with the standard program, and the white carrier with a red dot.

15. THERMAL OXIDATION (~2.7um)

Furnace no: B1   Program name: WET1000
Total time: 14h 30min   Program no: 3 _ _

PROCESS	TEMPERATURE (in °C)	GAS & FLOWS (in liter/min)	TIME (in minutes)	REMARKS
boat in	800	nitrogen: 6.0	5	
stabilize	800	nitrogen: 6.0	10	
heat up	+10 °C/min	nitrogen: 3.0 oxygen: 0.3	40	
stabilize	1150	nitrogen: 3.0 oxygen: 0.3	2	
oxidation	1150	nitrogen: 2.25 hydrogen: 3.85	14h	
cool down	-7 °C/min	nitrogen: 3.0	>30	
boat out	800	nitrogen: 3.0	5	

16. MEASUREMENT: OXIDE THICKNESS

Use the Leitz MPV-SP measurement system to measure the oxide thickness:
Program: Th. SiO2 on Si, >50nm auto5pts
Oxide thickness: ~2.7um front and back

17. PECVD DEPOSITION: 3300nm oxide on the front side (hard mask for Si DRIE)

Use the Novellus Concept One PECVD reactor.
Follow the operating instructions from the manual when using this machine.
Use group: **undoped oxides** (recipe **xxxsiostd**) to deposit a 6000 nm thick SiO_2 layer.
Change time to get the right thickness.

Process conditions from recipe xxxsiostd:					
Gasses & flows	Pressure	HF power	LF power	Temperature	Time
N_2/SiH_4/N_2O =3150/210/6000 sccm	2.2 Torr	1 kW	0 W	400 °C	47.6 $^{sec}/_{station}$

18. COATING

Use the coater station of the EVG120 system to coat the wafers with photoresist. The process consists of:
- a treatment with HMDS (hexamethyldisilazane) vapor, with nitrogen as a carrier gas
- spin coating of Shipley SPR3012 positive resist, dispensed by a pump
- a soft bake at 95 °C for 90 seconds
- an automatic edge bead removal with a solvent

Always check the relative humidity (48 ± 2 %) in the room before coating, and follow the instructions for this equipment.

Use program "**Co - 3027 – 3.1µm**".

19. ALIGNMENT AND EXPOSURE

Alignment and exposure will be done with the SUSS MicroTec MA/BA8 Mask Aligner. Follow the operating instructions from the manual when using this machine.

Use the mask **"3ul pillars"**, contact time must be **30s** with **hard contact**.

20. DEVELOPING

Use the developer station of the EVG120 system to develop the wafers. The process consists of:
- a post-exposure bake at 115 °C for 90 seconds
- developing with Shipley MF322 with a single puddle process
- a hard bake at 100 °C for 90 seconds

Always follow the instructions for this equipment.

Use program "**Dev - SP**"

21. PLASMA ETCHING: Open 6000 nm SiO2 (PECVD + thermal oxide)

Use the Drytek Triode 384T plasma etcher.
Follow the operating instructions from the manual when using this machine.
It is **not** allowed to change the process conditions from the etch recipe, except for the etch times!
Use recipe **STDOXIDE** to etch the oxide layer with a soft landing on the layer underneath.

Process conditions from recipe OXSFTLND:					
Step	Gasses & flows	Pressure	RF power	He pressure	Etch time
1. bulk etch (RIE)	C_2F_6/CHF_3 = 36/144 sccm	180 mTorr	300 W	12 Torr	10 min

22. RESIDUAL OXIDE REMOVAL

Remove residual oxide in BHF 1:7 Etching line

23. INSPECTION

Visually inspect the wafers through a microscope, and check if the holes are indeed open. No residues are allowed.

24. LAYER STRIPPING: Photoresist

Strip resist   Use the Tepla Plasma 300 system to remove the photoresist in an oxygen plasma.
                 Follow the instructions specified for the Tepla stripper, and use the quartz carrier.
                 Use **program 01**: 1000 watts power with 2 min overetch.

DRIE of pig noses

25. PLASMA ETCHING SILICON (660 um)

Use the Rapier Omega i2L DRIE etcher.
Follow the operating instructions from the manual when using this machine.
* number of cycles depends on the depth and dimensions of the holes
Average number of cycles for a depth of 660 um = 930

26. TEFLON RESIDUE REMOVAL

Strip resist   Use the Tepla Plasma 300 system to remove the Teflon residues in an oxygen plasma.
    Follow the instructions specified for the Tepla stripper, and use the quartz carrier.
    Use **program 02**: 1000 watts power for 5 minutes.

27. MEASURMENTS

Use Keyence for measuring etching profiles

* SiO2 that was used as a mask for etching is not going to be removed since it is beneficial in the next steps

Growing SiO$_2$ as a stopping layer for wet etching (~ 3.7 um)

28. CLEANING: HNO$_3$ 99% and 69.5%

Clean   10 minutes in fuming nitric acid at ambient temperature. This will dissolve organic materials.
    Use wet bench "HNO$_3$ 99% (Si)" and the carrier with the red dot.
Rinse   Rinse in the Quick Dump Rinser with the standard program until the resistivity is 5 MΩ.
Clean   10 minutes in concentrated nitric acid at 110 °C. This will dissolve metal particles.
    Use wet bench "HNO$_3$ 69,5% 110C (Si)" and the carrier with the red dot.
Rinse   Rinse in the Quick Dump Rinser with the standard program until the resistivity is 5 MΩ.
Dry   Use the Semitool "rinser/dryer" with the standard program, and the white carrier with a red dot.

29. THERMAL OXIDATION

Furnace no: B1   Program name: WET100
Total time: 19h 30min   Program no: __3__

PROCESS	TEMPERATURE (in ºC)	GAS & FLOWS (in liter/min)	TIME (in minutes)	REMARKS
boat in	800	nitrogen: 6.0	5	
stabilize	800	nitrogen: 6.0	10	
heat up	+10 ºC/min	nitrogen: 3.0 oxygen: 0.3	40	
stabilize	1150	nitrogen: 3.0 oxygen: 0.3	2	
oxidation	1150	nitrogen: 2.25 hydrogen: 3.85	14h	
cool down	-7 ºC/min	nitrogen: 3.0	>30	
boat out	800	nitrogen: 3.0	5	

30. MEASUREMENT: OXIDE THICKNESS (front and back)

Use the Leitz MPV-SP measurement system to measure the oxide thickness:
Program: Th. SiO2 on Si, >50nm auto5pts
Oxide thickness: ~3.7um in the holes

Definition of SiO$_2$ mask for back-side patterning

31. PECVD DEPOSITION: 5000 nm oxide on the back side

Use the Novellus Concept One PECVD reactor.
Follow the operating instructions from the manual when using this machine.
Use group: **undoped oxides** (recipe **xxxsiostd**) to deposit a 5000 nm thick SiO$_2$ layer.
Change time to get the right thickness. Keep in mind that some oxide was lost from the back-side during step 22.

Process conditions from recipe xxxsiostd:					
Gasses & flows	Pressure	HF power	LF power	Temperature	Time
N$_2$/SiH$_4$/N$_2$O =3150/210/6000 sccm	2.2 Torr	1 kW	0 W	400 °C	71 sec

32. COATING
Use the coater station of the EVG120 system to coat the wafers with photoresist. The process consists of:
- a treatment with HMDS (hexamethyldisilazane) vapor, with nitrogen as a carrier gas
- spin coating of Shipley SPR3012 positive resist, dispensed by a pump
- a soft bake at 95 °C for 90 seconds
- an automatic edge bead removal with a solvent

Always check the relative humidity (48 ± 2 %) in the room before coating, and follow the instructions for this equipment.

Use program "**Co - 3027 – 4μm**".

33. ALIGNMENT AND EXPOSURE BACKSIDE
Alignment and exposure will be done with the SUSS MicroTec MA/BA8 Mask Aligner. Follow the operating instructions from the manual when using this machine.

Use the mask "**Contacts_and_Wells**", contact time must be **40 s** with **hard contact**.

34. DEVELOPING
Use the developer station of the EVG120 system to develop the wafers. The process consists of:
- a post-exposure bake at 115 °C for 90 seconds
- developing with Shipley MF322 with a single puddle process
- a hard bake at 100 °C for 90 seconds

Always follow the instructions for this equipment.

Use program "**Dev - SP**"

35. PLASMA ETCHING: hard mask on the backside
Use the Drytek Triode 384T plasma etcher.
Follow the operating instructions from the manual when using this machine.
It is **not** allowed to change the process conditions from the etch recipe, except for the etch times!

Use recipe **STDOXIDE** to etch the oxide layer with a soft landing on the layer underneath.

Process conditions from recipe OXSFTLND:					
Step	Gasses & flows	Pressure	RF power	He pressure	Etch time
1. bulk etch (RIE)	C_2F_6/CHF_3 = 36/144 sccm	180 mTorr	300 W	12 Torr	14 min

36. INSPECTION
Visually inspect the wafers through a microscope, and check if the holes are indeed open. No residues are allowed.

37. LAYER STRIPPING: Photoresist
Strip resist   Use the Tepla Plasma 300 system to remove the photoresist in an oxygen plasma.
Follow the instructions specified for the Tepla stripper, and use the quartz carrier.
Use program 01: 1000 watts power with 2min overetch watts power and automatic 12 min.

38. CLEANING: HNO_3 99% and 69.5%
Clean   10 minutes in fuming nitric acid at ambient temperature. This will dissolve organic materials.
Use wet bench "HNO_3 99% (Si)" and the carrier with the red dot.
Rinse   Rinse in the Quick Dump Rinser with the standard program until the resistivity is 5 MΩ.
Clean   10 minutes in concentrated nitric acid at 110 °C. This will dissolve metal particles.
Use wet bench "HNO_3 69,5% 110C (Si)" and the carrier with the red dot.
Rinse   Rinse in the Quick Dump Rinser with the standard program until the resistivity is 5 MΩ.
Dry   Use the Semitool "rinser/dryer" with the standard program, and the white carrier with a red dot.

PDMS deposition – first layer

START PDMS IN POLYMER LAB

39. PDMS PREPARATION
In this step the preparation of the PDMS will be done using the elastomer PDMS Sylgard 184 and its curing agent.

Pour **5 g** of the PDMS elastomer in the disposable cup and **0.5 g** of curing agent by using a pipette. Depending on the number of wafers to be processed these amounts could vary but the ratio between the elastomer and curing agent must be keep on 10:1.

Don't forget protecting the weighting machine of any leakage of elastomer or curing agent during the preparation of the material. Use for this a towel to protect the plate of the machine.

5

40. PDMS MIXING
For mixing the PDMS elastomer and curing agent use the Thinky Speedmixer. Make sure that the cup holder is properly located in the machine. Determine the total weight of the cup and the holder and adjust the machine according to this value. Follow the instructions established for this machine.

Select program **01,** check the parameters for each step if necessary and then start the process.

41. PDMS DEPOSITION – filling the holes
Pour thick layer of PDMS on wafer and very slowly spin-coat, to be sure that there is enough PDMS to cover the holes

42. PDMS degassing (first time)
For this step use the vacuum desiccator in the polymer lab. Place carefully wafer inside of the vacuum chamber and turn on the pump. Wait around 20 minutes until all bubbles are gone and then switch off the pump. Slowly open the valve to increase the pressure in the chamber until atmospheric and remove the wafer.
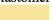
43. Removing and curing PDMS
Use sharp object to uniformly remove PDMS from the wafer and not to damage the wafer surface. After removal of the extra PDMS, bake it for **60** minutes in the Memmert Oven @ **90°C**.

**perform uniformity test to check the thickness of the PDMS layer

44. PDMS DEPOSITION – 50um
For the deposition of PDMS layer use the Polos Manual Spinner 1 Cl100. **Cover** both the bottom and the ring of the spinner with **aluminium foil** to avoid residues of the polymer on the machine.
Pour the PDMS elastomer and curing agent mixture to cover about 2/3 parts of the wafer. (approximately 3g)
Select the recipe _ _ _ _ _ to spin the material.

45. PDMS BAKING
For baking of the PDMS layer use the Memmert Oven with the dedicated carrier (PDMS). Set the temperature level to 90 °C. Establish the temperature level prior to this step since it takes some time because the heat capacity if the oven is high.

Bake the PDMS layer at **90 °C** for **60 min**.

Note: Check again at the end of the processing if any residual is present. Residuals are not allowed neither on the frontside nor the backside of the wafer.

46. MEASUREMENTS
Measure PDMS thickness using Keyence microscope.

47. PDMS ETCH
Dry etching of PDMS with no etch stop layer to reach minimum possible thickness.

48. MEASUREMENTS
Measure PDMS thickness using Keyence microscope.

METAL DEPOSITION – SPIRAL SENSORS
49. PLASMA TREATMENT
Expose wafers to oxygen plasma in ATTO Diener for a duration of 1 minute and a power of 200 W.

50. ALUMINIUM SPUTTERING
Use the TRIKON SIGMA 204 sputter coater for the deposition of 500 nm aluminium metal layer on the wafers at 25 ºC at a power of 1000 W.
The target must consist of pure Aluminium, and deposition must be done at RT with an Ar flow of 100 sccm. Follow the operating instructions from the manual when using this machine.

Note: Before running the recipe, it is **mandatory** for this process first of all to make a Leak-Up rate test of the PDMS layer in order to avoid any damage in the machine.
Whether this test is skip or the results of the test are not satisfactory the processing of the wafers in this machine is not allowed.

51. COATING

Use the coater station of the EVG120 system to coat the wafers with photoresist. The process consists of:
- spin coating of Shipley SPR3012 positive resist, dispensed by a pump

Always check the relative humidity (48 ± 2 %) in the room before coating, and follow the instructions for this equipment.

Use program **"Co - 3012 – 1.4 – no EBR - no HMDS - no HB - no PEB"** and wet carrier.

52. SOFT BAKE

Manually bake at 90 ºC for a duration of 90 seconds.
Handle carefully.

53. ALIGNMENT AND EXPOSURE

Alignment and exposure will be done with the SUSS MicroTec MA/BA8 Mask Aligner. Follow the operating instructions from the manual when using this machine.

Use the mask **"Sensors_Interconnects_Contacts"**, contact time must be 9s with hard contact.

54. POSE EXPOSURE BAKE

Manually bake at 90 ºC for a duration of 90 seconds.
Handle carefully.

55. DEVELOPING

Use the developer station of the EVG120 system to develop the wafers. The process consists of:
- developing with Shipley MF322 with a single puddle process

Always follow the instructions for this equipment.

Use program **"Dev – SP- no PEB – no HB"**

56. POSE DEVELOPMENT BAKE

Manually bake at 90 ºC for a duration of 90 seconds.
Handle carefully.

57. INSPECTION: Linewidth and overlay

Visually inspect the wafers through a microscope, and check the line width and overlay.

58. PLASMA ETCHING OF ALUMINUM

Use the Trikon Ωmega 201 plasma etcher.
Follow the operating instructions from the manual when using this machine.
It is not allowed to change the process conditions and times from the etch recipe! Define new recipe based on parameters given in table below

Etched material	Cl₂ flow (sccm)	HBr flow (sccm)	ICP power (W)	RF Power (W)	Duration (sec)
Aluminium Oxide	30	40	500	50	Endpoint enabled
Bulk Al	30	40	500	40	Endpoint enabled
Over-etch 1	15	30	500	40	10

59. INSPECTION

Visually inspect the wafers through a microscope, and check if the holes are indeed open. No residues are allowed.

60. LAYER STRIPPING: Photoresist

Rinse in acetone for 15 minutes followed by 1 minutes in low power plasma at 200 W.

PDMS deposition – second layer

61. ENCAPSULATION

Encapsulation is done via deposition of second layer of PDMS in the Polos Manual Spinner 1 at a spin speed of 2000 rpm for 30 seconds.
- If wafer was taken out for measurements on probe station with gold chuck, store wafer in gold box prior to deposition of second PDMS layer. Use contaminated tweezer and plastic chuck for spin coating.

Critical steps:

1. Deposition of low thickness Aluminum directly on top of PDMS. It has been shown that Al has a critical thickness of 250 nm after which cracking phenomena *might* be observed. Al thickness can vary between 50-200 nm depending on results. Prior to deposition of Al, surface treatment (plasma or chemical) of PDMS could be helpful.
2. Presence of 8 contact pads (1mm x 1mm) and one hole ($2\phi = 6$mm) per die can lead to stress distributions in Si when back etched. Wire bonding can be replaced by probing for electro-mechanical characterization.

Tests

1. Visual inspection of patterned sensors (Al). Possible analysis of the reflection wavelength (if surface is not smooth) using optical tests to find the effects of surface roughness on capacitance.
2. Check stability of measurements in probe station after deposition of second layer of PDMS.

Contamination protocol (PDMS):

1) Use separate carrier for all wafers coated with PDMS.
2) Due to high spin speed PDMS "ring" is formed on the back-side. This can be prevented in two ways:
   ➔ Protect back-side of wafer with 4 micrometers of SPR3027 photoresist via manual spin coating and baking. HMDS is not required since we do not need to pattern anything. Cure PDMS in oven with resist on the back. After curing, remove resist with acetone. Curing should be complete since uncured PDMS is also affected by acetone. Rinse the wafer with water and dry in spinner.
   ➔ The second method involves removal of PDMS from the back after spin-coating without backside protection. Cotton buds dipped in acetone must be very slowly dragged along the back-side to remove un-cured PDMS. Edge bead and PDMS removal must be performed on the top, bottom and side of the wafer. After curing, the backside of the wafer is further cleaned with acetone and IPA in EVG 101 spray coater.

8

APPENDIX G

Multiphysics Modeling of a Co-planar Capacitive Spiral Sensor for Measurement of Contractile Forces Generated in Miniaturized Engineered Heart Tissue Platforms

Mahdieh Shojaei Baghini

Introduction: Factors which contribute to maturation and efficient proliferation of cardiac tissue in vitro are the presence of mechanical pre-load. In vivo heart cells are exposed to auxotonic loading which involves a positive force-strain relationship during contraction followed by a stress relaxation phase [1]. Hence there always exists a certain degree of resistance to contraction which can be emulated in heart on chip architectures. These heart on chip architectures consist of micropillars around which cardiac issue can grow and beat. Cardiac tissue is often characterized by generated contractile forces and action potentials [2]. The forces provide an indication of tissue volume, maturation, and their variation due to external stimuli and drug exposure. Contraction force microscopy is the most commonly used technique for the derivation of cardiac contraction force [3][4]. To be able to efficiently correlate pillar displacement with contraction force, the stiffness of the pillar must be known. However, as the complexity in geometry of the platform increases, the exact derivation of its Young's Modulus becomes cumbersome and difficult to validate and alternate measurement techniques must be utilized. Additionally, in order to measure the thickness of the tissue the focal plane must be manually varied which can cause errors in recordings. Human errors such as misalignments can cause significant discrepancies in results as well [4]. In order to circumvent these challenges, the development of a novel integrated capacitive sensors is explored in this paper. The developed capacitors have a peak sensitivity of 4.86 pF/N.

Multiphysics modelling: As shown in Fig. 1., the pillars around which cardiac tissue grows are in continuum with the soft substrate to which they are attached. Due to contraction forces generated, the pillars (L = 700 μm, W = 478 μm, B = 191 μm, Young's Modulus = 1.7 MPa, Poisson's ratio = 0.49) tilt leading to displacement within the substrate. The micropillar systems is defined in the Solid Mechanics model with a finer mesh distribution at the interface of the pillar with the substrate as shown in Fig. 2.
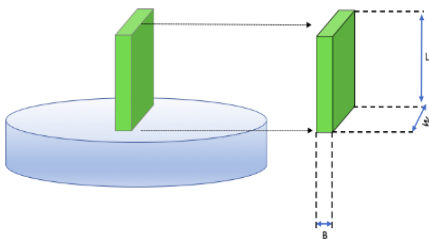

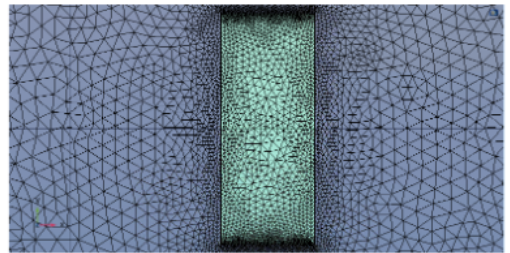Fig. 1. Single micropillar (PDMS) in continuum with substrate (blue).

Fig. 2. Higher distribution of mesh elements at the pillar-substrate interface.

In order to detected this displacement, integrated coplanar spiral capacitive sensors have been designed of which the base capacitance changes with the applied force. Due to their spiral nature, the surface area is maximized which increases sensitivity to substrate deformation. Since the primary quantity of interest is the electric field in the system, the simulation environment has been modified to include a spherical air domain around the sensor (in grey) integrated with the EHT platform as shown in Fig. 3. Additionally, a moving mesh has been assigned to this air domain to account for the changes in the electrical field due to the application of

a boundary load to the pillar. The distortion in the spatial electric field is then coupled to the change in the terminal capacitance of the system. The plates are modelled as pure conductors and charge storage entities. The properties of the sensor are shown in Fig. 4 with $L_a = 1200$ μm and $L_b = 200$ μm.
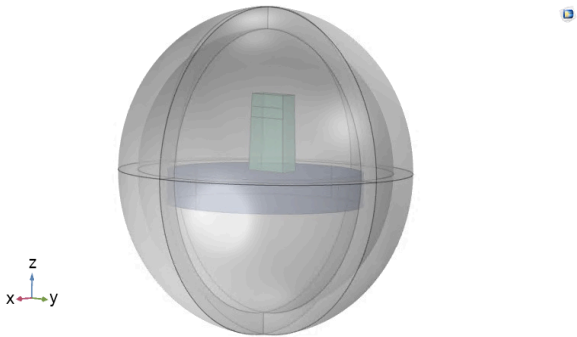

Fig. 3. Spherical air domain around micropillar integrated with sensor.

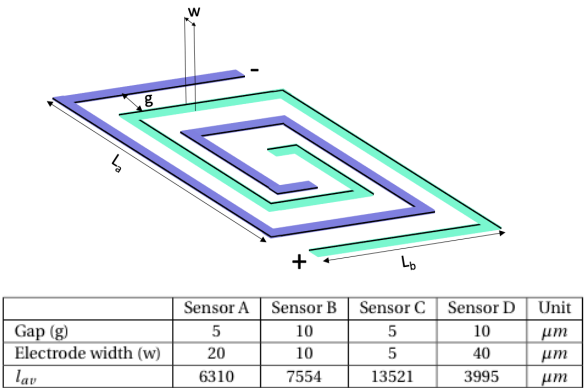|	Sensor A	Sensor B	Sensor C	Sensor D	Unit
Gap (g)	5	10	5	10	μm
Electrode width (w)	20	10	5	40	μm
l_{av}	6310	7554	13521	3995	μm

Fig. 4. Geometrical properties of designed spiral sensors with l_{av} representing the average path length of the plates.

storage entities responsible for the generation of electric field while the outer boundaries of the air domain are assigned zero charge boundary conditions and act as perfect insulators. Aluminum has been chosen as plate material due to its lower stiffness as compared to other metals as well as its biocompatibility. The fully coupled solver has been replaced with a segregated solver to reduce computation time. The plates of the capacitor are modeled using the Shell interface in COMSOL leading to a Solid Mechanics-Shell-Electrostatics coupling.

Results: On the application of a boundary load, the sensors deform exhibiting a linear response with force. The sensitivity of the sensors is shown in Fig. 5 as a function of sensor depth leading to an exponential drop with depth. The top view of the final sensors is shown in Fig. 6 along with their integration with the micropillar system. The antisymmetric nature of the response on either side of the pillar leads to the possibility of IC integration and point-of-care diagnostics.
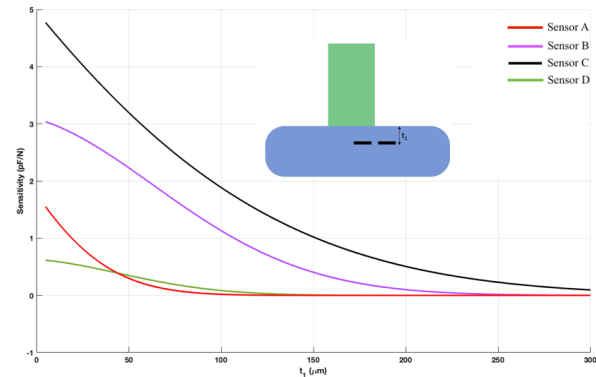

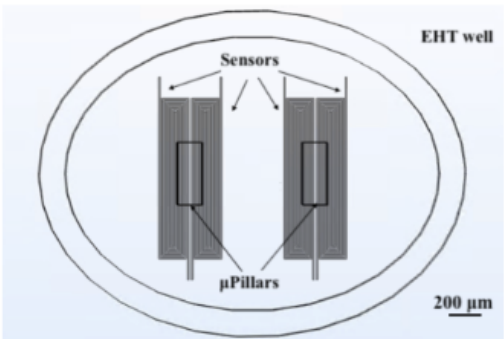Fig. 5. Exponential drop in sensitivity of sensors with substrate depth.

Fig. 6. Integration of spiral sensors with micropillars [top-view].

REFERENCES

[1] N. Dam Madsen et al., "Titanium nitride as a strain gauge material", *J. Microelectromechanical Syst.*, vol. 25, no. 4, pp. 683–690, Aug. 2016.

[2] A. Shokuhfar, P. Heydari, M. R. Aliahmadi, M. Mohtashamifar, S. Ebrahimi-Nejad R., and M. Zahedinejad, "Low-cost polymeric microcantilever sensor with titanium as piezoresistive material", *in Microelectronic Engineering*, 2012, vol. 98, pp. 338–342.

[3] T. Han et al., "Gold/polyimide-based resistive strain sensors", *Electron.*, vol. 8, no. 5, p. 565, May 2019.

[4] D. Gräbner, G. Dumstorff, and W. Lang, "Simultaneous Measurement of Strain and Temperature with two Resistive Strain Gauges made from Different Materials", in *Procedia Manufacturing*, 2018, vol. 24, pp. 258–263.

[5] M. Ahmed, M. M. Chitteboyina, D. P. Butler, and Z. Celik-Butler, "MEMS Force sensor in a flexible substrate using nichrome piezoresistors", *IEEE Sens. J.*, vol. 13, no. 10, pp. 4081–4089, 2013.

[6] E. Peiner, A. Tibrewala, R. Bandorf, S. Biehl, H. Lüthje, and L. Doering, "Micro force sensor with piezoresistive amorphous carbon strain gauge", in *Digest of Technical Papers - International Conference on Solid State Sensors and Actuators and Microsystems, TRANSDUCERS '05*, 2005, vol. 1, pp. 551–554.

[7] A. Tibrewala, E. Peiner, R. Bandorf, S. Biehl, and H. L. Uthje, "Piezoresistive gauge factor of hydrogenated amorphous carbon films", *MICROMECHANICS MICROENGINEERING J. Micromech. Microeng*, vol. 16, pp. 75–81, 2006.

[8] Gamil, M., H. Nageh, I. Bkrey, S. Sayed, A. F. M. R. El-Bab, K. Nakamura, O. Tabata, and A. A. El-Moneim, "Graphene-Based Strain Gauge on a Flexible Substrate", *Sensors and Materials*, vol. 26, issue 9, pp. 699-709, 2014.

[9] U. Lang, P. Rust, B. Schoberle, and J. Dual, "Piezoresistive properties of PEDOT:PSS", *Microelectron. Eng.*, vol. 86, no. 3, pp. 330–334, Mar. 2009.

[10] C. Liu and J. Choi, "An embedded PDMS nanocomposite strain sensor toward biomedical applications", *2009 Annual International Conference of the IEEE Engineering in Medicine and Biology Society*, Minneapolis, MN, 2009, pp. 6391-6394.

[11] "MEMS Mechanical Sensors - Stephen Beeby - Google Books." [Online]. Available: http://tiny.cc/8plpkz [Accessed: 01-Mar-2020].

[12] H. Muro, T. Mitamura, S. Kiyota, "Determination of Electrical Properties of n-Type and p-Type Polycrystalline Silicon Thin Films as Sensor Materials", *Sensors and Materials*, vol. 18, no. 8, pp. 433-444, Jan. 2006

[13] M. A. Fraga, M. Massi, H. Furlan, I. C. Oliveira, L. A. Rasia, and C. F. R. Mateus, "Preliminary evaluation of the influence of the temperature on the performance of a piezoresistive pressure sensor based on a-SiC film", *Microsyst. Technol.*, vol. 17, no. 3, pp. 477–480, Mar. 2011.

[14] H. Lapp et al., "Frequency-dependent drug screening using optogenetic stimulation of human iPSC-derived cardiomyocytes", *Sci. Rep.*, vol. 7, no. 1, pp. 1–12, Dec. 2017.

[15] D. Ingrassia, M. Sladkova, M. Palmer, W. Xia, H. Engqvist, and G. M. de Peppo, "Stem cell-mediated functionalization of titanium implants", *J. Mater. Sci. Mater. Med.*, vol. 28, no. 9, p. 133, Sep. 2017.

[16] L. M. Ricles, S. Y. Nam, K. Sokolov, S. Y. Emelianov, and L. J. Suggs, "Function of mesenchymal stem cells following loading of gold nanotracers", *Int. J. Nanomedicine*, vol. 6, pp. 407–416, 2011.

[17] J. M. L. Roodhart et al., "Mesenchymal stem cells induce resistance to chemotherapy through the release of platinum-induced fatty acids", *Cancer Cell*, vol. 20, no. 3, pp. 370–383, Sep. 2011.

[18] K. M. Szostak, L. Grand, and T. G. Constandinou, "Neural interfaces for intracortical recording: Requirements, fabrication methods, and characteristics", *Frontiers in Neuroscience*, vol. 11, no. DEC. Frontiers Media S.A., p. 665, Dec. 2017.

[19] D. G. Liu et al., "Preparation, biocompatibility, and biotribological properties of TiN-incorporated graphite-like amorphous carbon bio-ceramic composite films", *Ceram. Int.*, vol. 44, no. 6, pp. 6810–6816, Apr. 2018.

[20] S. Martino et al., "Hydrogenated amorphous carbon nanopatterned film designs drive human bone marrow mesenchymal stem cell cytoskeleton architecture", *Tissue Eng. Part A*, vol. 15, no. 10, pp. 3139–49, Oct. 2009.

[21] I. Lasocka et al., "The effects of graphene and mesenchymal stem cells in cutaneous wound healing and their putative action mechanism", *International Journal of Nanomedicine*, vol. 14. Dove Medical Press Ltd., pp. 2281–2299, Aug. 2019.

[22] A. G. Guex et al., "Highly porous scaffolds of PEDOT:PSS for bone tissue engineering", *Acta Biomater.*, vol. 62, pp. 91–101, Oct. 2017.

[23] K. Das et al., "Functionalized carbon nanotubes as suitable scaffold materials for proliferation and differentiation of canine mesenchymal stem cells", *Int. J. Nanomedicine*, vol. 12, pp. 3235–3252, Apr. 2017.

[24] "Physics and Technology of Silicon Carbide Devices - Google Books." [Online]. Available: https://bit.ly/2wVFWZG [Accessed: 01-Mar-2020].

[25] R. Zeiser, T. Fellner, and J. Wilde, "Capacitive strain gauges on flexible polymer substrates for wireless, intelligent systems", *J. Sensors Sens. Syst.*, vol. 3, pp. 77–86, 2014.

[26] D. H. Huynh (2016), *Novel Applications of Static Micro-Scale Interdigitated Electrodes for Energy Harvesting and Biosensing*, University of Melbourne, Australia.

[27] Y. Li et al., "A soft polydimethylsiloxane liquid metal interdigitated capacitor sensor and its integration in a flexible hybrid system for on-body respiratory sensing", *Materials (Basel).*, vol. 12, no. 9, 2019.

[28] O. Atalay, "Textile-based, interdigital, capacitive, soft-strain sensor for wearable applications", *Materials (Basel).*, vol. 11, no. 5, May 2018.

[29] H. Shin, A. Charalambides, I. Penskiy and S. Bergbreiter, "A soft microfabricated capacitive sensor for high dynamic range strain sensing", *2016 IEEE/RSJ International Conference on Intelligent Robots and Systems (IROS)*, Daejeon, 2016, pp. 5572-5578.